Plate-Rod Microstructural Modeling for Accurate and Fast Assessment of Bone Strength

Ji Wang

Submitted in partial fulfillment of the
requirements for the degree of
Doctor of Philosophy
in the Graduate School of Arts and Sciences

COLUMBIA UNIVERSITY

2016

ABSTRACT

Plate-Rod Microstructural Modeling for Accurate and Fast Assessment of Bone Strength

Ji Wang

Progressive bone loss and weakening bone strength associated with aging predispose the elderly population to osteoporosis and millions of costly fragility fractures. Micro finite element (μFE) analysis based on clinical high-resolution skeletal imaging provides an accurate computational solution to assessing the mechanical properties of bone, which can be used as the dominant factors for fracture risk. However, the current μFE analysis technique is impractical for clinical use due to its prohibitive computational costs, which result from the "voxel-to-element" approach of modeling human bone regardless of its microstructural pattern. I developed a novel plate-rod microstructural modeling technique for highly efficient patient-specific μFE analysis and translated it to clinical research for the assessment of bone strength in osteoporosis and fragility fractures.

Trabecular microstructure is composed of interconnected plate-like and rod-like trabeculae. Instead of converting every image voxel directly into an element, the plate-rod modeling approach created mechanical characterization for every individual trabecular plate and rod. The validation studies demonstrated that the PR model was able to reproduce the morphology and mechanical behavior of the original trabecular microstructure, while reducing the size of the μFE model and improving the efficiency of μFE simulations. First, the PR models of trabecular bone were developed based on high-resolution micro computed tomography (μCT), and evaluated in comparison with computational gold standard-voxel μFE models and experimental gold standard-mechanical testing for estimating Young's modulus and yield strength of human trabecular bone.

Results suggested that PR model predictions of the trabecular bone mechanical properties were strongly correlated with voxel models and mechanical testing results. Moreover, the PR models were indistinguishable from the corresponding voxel models constructed from the same images in the prediction of trabecular bone Young's modulus and yield strength. In addition, PR model nonlinear μFE analyses resulted in over 200-fold reduction in computation time compared with voxel model μFE analyses.

In the effort of studying the heterogeneous bone mineralization in trabecular plates and rods, I developed an individual trabecula mineralization (ITM) analysis technique that allows quantification of the tissue mineral density of each individual trabecular plate and rod. By examining the variation of mineral density with trabecular types and orientations, it was found that trabecular plates were higher mineralized than trabecular rods. Furthermore, trabecular plate mineral density varied with trabecular orientation, increasing from the longitudinal direction to the transverse direction. ITM provided measurement of mineral density of each trabecular plate and rod, which was converted to trabecula-specific tissue modulus and used in the PR models to incorporate mineral heterogeneity in μFE simulations. Results suggested that heterogeneous PR models did not differ from the homogeneous PR models or specimen-specific PR models in their predictions of apparent Young's modulus and yield strength of the human trabecular bone specimens from non-diseased donors.

Based on the trabecular bone PR model, a whole bone PR model was developed for assessing whole bone mechanical strength at the distal radius and the distal tibia from high-resolution peripheral quantitative computed tomography (HR-pQCT). The accuracy of the whole bone PR model was evaluated on human cadaver radius and tibia specimens which were imaged using HR-pQCT and μCT, respectively, and tested to failure. The whole bone stiffness and yield

load of the radius and tibia segments predicted by HR-pQCT PR models were strongly correlated with those predicted by corresponding HR-pQCT voxel models, μCT voxel models, and mechanical testing measurements. The PR models μFE results were indistinguishable from the voxel models constructed from the same HR-pQCT images. Moreover, the PR models significantly reduced the computational time for nonlinear μFE assessment of whole bone strength. After evaluating the accuracy and efficiency of the newly developed whole bone PR model, it was employed in a clinical study aimed at characterizing the abnormalities of trabecular plate and rod microstructure, cortical bone, and whole bone mechanical properties in postmenopausal women with vertebral fractures. Women with vertebral fractures had thinner cortical bone, and larger trabecular area compared to their non-fractured peers. ITS analyses suggested vertebral fracture subjects had deteriorated trabecular microstructure, evidenced by fewer trabecular plates, less axially aligned trabeculae and less trabecular connectivity at both radius and tibia. These microstructural deficits translated into reduced whole bone stiffness and yield load at radius and tibia as predicted by PR model nonlinear μFE simulation. More importantly, logistic regression indicated that whole bone yield load was effective in discriminating the vertebral fracture subjects from the non-fractured controls.

Table of Contents

List of Tables

List of Figures

Acknowledgements

I owe my sincere thanks to my dear family, my great mentor, colleagues, friends, and everyone else who offered me support and help in my PhD study. It is the encouragement from all of you that gives me faith in myself to overcome challenges and complete my thesis work.

First of all, I would like to express my greatest gratitude to my thesis advisor, Prof. X.Edward Guo. Thank you for granting me the opportunity to pursue PhD study in the first place. It was an incredible opportunity for me as a colleague graduate in China to travel across the world to the US and study at a prestigious Ivy League university. You guided me every step along the way from learning to conduct research to starting my first project, trouble shooting my program, having my first conference talk, writing my first paper, building up my thesis project, until today completing my PhD training. You always gave me courage to accomplish the impossible and provided me with insights. I feel fortunate to have you direct me towards a productive development of my research and indeed learned tremendously from your sharp insights, meticulous attention to details, and great vision. Moreover, I sincerely appreciate your and Carol's caring for me, my parents, my husband Bo, and our daughter Olivia. The blessing from you and Carol are so warm and sweet that we will always be grateful for.

Secondly, I want to thank the Howard Hughes Medical Institute (HHMI) for granting me the HHMI International Pre-doctoral Student Fellowship. It is my greatest honor to conduct my thesis research with the support of the fellowship. I feel responsible for doing the best I can to accomplish the thesis research that deserves this prestige. I hope to make my contribution to the HHMI and biomedical research in the future.

In addition, I would like to extend my thanks to our collaborators, Dr. Elizabeth Shane, Dr. Emily Stein, Dr. Kyle Nishiyama, and Fernando Rosete at Columbia University Medical Center.

It is my great pleasure to work with Dr. Shane's team, who provided me with the opportunity to get involved in clinical research on osteoporosis and fractures, and gave me invaluable suggestions on project design, writing and presentation from their professional perspectives. I would also like to thank Dr. Galateia Kazakia at University of California, San Francisco for collaborating with me in studying heterogeneous bone mineralization in trabecular plates and rods, and providing valuable SRμCT images in our co-authored paper on JBMR.

Furthermore, I want to give my special thanks to my wonderful colleagues in the Bone Bioengineering Lab, Dr. Bin Zhou, Genevieve Brown, Eric Y. Yu, Andrea Morrell, Sam Robinson, Rachel Sattler, Jenny Hu, Eddie Zhang, and previous lab members Dr. Sherry Liu and Dr. Andrew Baik. I am so proud to be part of this great team. We always support each other with the best we can offer. In particular, I would like to thank Dr. Bin Zhou and Eric Yu for your instrumental help in my thesis research. I would also like to thank Dr. Sherry Liu for developing individual trabecula segmentation technique and making the initial effort in developing the plate-rod modeling technique in her PhD research, which laid valuable foundation for my work in the development of individual trabecula mineralization analysis and plate-rod micro finite element modeling. I am truly grateful for sharing this chapter of my life with you and becoming friends with you. Our friendship and all the joyful moments in our lab and BBL exclusive office will become beautiful memories that I will cherish forever.

Besides, I would like to thank the faculty and staff in the Department of Biomedical Engineering, Prof. Christopher Jacobs, Prof. Van Mow, Prof. Paul Sajda, Prof. Henry Hess for being on my qualifying exam, proposal, and defense committee; Prof Helen Lu and Prof. Sam Sia for your help with my application for the HHMI international student fellowship; Shila Maghji, Kidest

Shenkoru, Paulette Louissaint, Michelle Cintron, Jarmaine Lomax, James Ihn for your kindest help with the administrative issues.

Last but not least, I want to give my deepest thanks to my loving husband Bo, my little princess Olivia, and my parents. I could not have gone so far without your selfless support and unconditional love. You are the best family I could ever hope for.

To my dearest Bo and Olivia

Chapter 1. Overview

1.1. Background

1.1.1. Bone Anatomy and Physiology

The human skeleton is the internal framework of the body. It provides structural support for the body shape, permits movement and locomotion, and protect the fragile organs inside the body. Furthermore, bone tissue serves as a reservoir of minerals to help maintain mineral balance and provides environment for hematopoiesis within the marrow spaces. Bone constantly undergoes remodeling throughout life to remove old, microdamaged bone and replace it with new, fresh bone to help it adapt to changing biomechanical environment. The four general categories of bones are long bones, short bones, flat bones, and irregular bones. The long bones, such as femurs, radii, and tibiae, are composed of a long hollow shaft, or diaphysis, in the middle; two cone-shaped metaphases below the growth plate; and two rounded epiphyses on both ends above the growth plate. The diaphysis is composed primarily of dense cortical bone, also known as compact bone; whereas the metaphases and epiphyses are composed of porous trabecular bone surrounded by a relatively thin shell of cortical bone.

The adult human skeleton has 80% cortical bone and 20% trabecular bone overall. Different skeletal sites have different proportions of cortical bone and trabecular bone. Trabecular bone accounts for 75% of the bone mass in the vertebra, 50% in the femoral head, and 5% in the radial diaphysis. Cortical bone is composed of osteons, which are cylindrical in shape with concentric lamellae surrounding the Haversian canals. Normal cortical bone has low porosity. In aging adults, increased cortical remodeling often results in thinning of the cortex and increased cortical porosity, which compromise the mechanical strength of cortical bone. Trabecular bone has a honeycomb-like microscopic structure, composed of interconnected

trabeculae around 100~150 μm in thickness. The two types of trabeculae are trabecular plates and rods, classified according to the shape of the trabeculae. Bone remodeling occurs on the trabecular surface. Increased trabecular bone remodeling may cause perforation in trabecular plates and breakage in trabecular rods. Aging adults normally experience a change from more of a plate-like trabecular network to a more rod-like structure.

Bone strength is not only determined by bone mass, but also by bone geometry on the organ level, cortical and trabecular microstructure on the microscopic level, and the intrinsic material properties of bone on the tissue level. Bone tissue consists of 65% mineral, 35% organic matrix, cells, and water. The organic matrix is dominated by Type-I collagen and the mineral is in the form of hydroxyapatite located within and between collagen fibers. Bone mineral provides mechanical rigidity and load-bearing strength to bone, whereas the organic matrix provides flexibility and elasticity. When new bone is formed, the bone forming cells, called osteoblasts, secrete and deposit the collagen matrix first, which then gradually mineralizes. The mineralization process starts with a rapid increase in the mineral content during the first few days up to 70% of the final level, a phase typically referred to as the primary mineralization, and followed by a slow and gradual maturation of the mineral content, referred to as secondary mineralization. The mineral content of bone matrix is not uniform because bone packets are deposited at different moments in a remodeling cycle, and the mineral content depends on the time since its deposition. Therefore, the average mineral density and the heterogeneity of mineralization are both important factors in determining fundamental mechanical properties of bone tissue, which also affect bone strength on the whole bone level.

1.1.2. Microstructure of Trabecular Bone

Trabecular bone network consists of interconnected plate-like and rod-like trabeculae, typically 100~150 μm in thickness. The microstructure of trabecular bone directly determines the mechanical properties of trabecular bone. Age-related alteration occurs in the trabecular microstructure, which is typically evidenced by trabeculae loss, trabeculae thinning, or disorientation of the trabecular network (Chen, Zhou et al. 2013). Such structural changes compromise the mechanical strength of trabecular bone and lead to increased susceptibility to fractures.

Morphological parameters charactering the trabecular microstructure have been utilized in order to quantitatively assess bone quality. These parameters can be divided into three categories: scale, orientation, and topology (Wehrli 2007). The scale parameters include bone volume fraction, trabecular thickness, and trabecular number. The bone volume fraction has been considered as the predominant microstructural parameter that strongly correlated with the elastic modulus of trabecular bone. Trabecular thickness and number provides additional measurement of the trabeculae, which allows understanding of the structural changes on the trabecula level beyond bone volume fraction. Trabecular network exhibits a pronounced alignment with the principle direction of mechanical loads applied to the anatomic location. Adaptation of trabecular microstructure to the mechanical environment is referred to as Wolff's law (Wolff 1986). The orientation of trabecular network therefore plays an important role to convey load-bearing function along the principle direction. Structural anisotropy is used to characterize trabecular orientation. Topology refers to the geometric properties of objects, which are not affected by deformation. Topological characteristics of trabecular bone include types of trabeculae and connectivity between trabeculae. Plate-like trabecular network differs from rod-like structure in

topological configuration, as well as the mechanical competence of the structure. In case of trabecula breakage, initially interconnected trabeculae become isolated from each other, and the structural connectivity will be changed. Conversely, the trabecular network remains unaltered topologically if the trabeculae are simply thickened. Early study has demonstrated that loss of trabeculae, which alters trabecular topology, has more pronounced mechanical consequence than trabeculae thinning (Guo and Kim 2002).

These three categories of trabecular microstructural parameters determine trabecular bone quality. The methods of measuring these parameters will be introduced in Chapter 1.2.

1.1.3. Mechanical Properties of Bone

Fractures occur when external mechanical stresses exceed bone's capacity to withstand them. The mechanical properties of bone characterizes bone's behavior under mechanical loads, and are important quantitative factors for assessing the risk of fractures. There are two levels of mechanical properties: apparent level, which refers to the mechanical behavior at the continuum level of the whole bone specimen; and tissue level, which refers to those at the individual trabeculae or osteon level.

The apparent properties can be determined experimentally from compressive, tensile and torsional tests. In general, trabecular bone exists in areas where compressive loads dominate. In this thesis, I mainly focus on the compressive properties of trabecular bone and whole bone segments with the cortex enclosing the trabecular compartment. Trabecular bone plays an important role in load transmission and energy absorption in major joints such as the knee, hip, ankle and the spine, which are also most common anatomic locations of osteoporotic fractures. In the vertebral body, trabecular bone carries more than 75% mechanical load (Eswaran, Gupta et al. 2006). The mechanical properties of trabecular bone varies significantly with respect to

age, sex and anatomic locations, depending on the apparent density and the trabecular microstructure. It has been demonstrated that elastic modulus and strength of trabecular bone is strongly correlated with bone volume fraction by a power-law relationship (Zhou, Liu et al. 2014). In addition, topological and orientation-related microstructural parameters have significant impact on the mechanical properties of trabecular bone (Liu, Sajda et al. 2006).

Uniaxial compression tests are usually carried out to measure the elastic and yield properties. Trabecular bone specimens are machined into cylinder shape and compressed between two endcaps. Whole bone segments with two parallel end surfaces are cut out from long bone specimens and compressed between two platens. It is critical to accurately align the specimen with the loading direction in such mechanical testing experiment. Also, the longitudinal axis of the trabecular bone specimen needs to be aligned with the principle orientation of trabeculae. A typical stress-strain curve from the experiment starts with a linear elastic part and followed by a nonlinear yielding part where bone begins to fail. Young's modulus is calculated as the slope of the fitting line of the linear part. Yield strength represents the stress at which the strain-stress curve starts to deviate from the linear elastic regime. The yield strength and strain are determined from the intersection between the resulting strain-stress curve and a line parallel to the line fitting in the elastic range, with an offset of 0.2% strain (Keaveny, Guo et al. 1994). Similarly, stiffness and yield force of whole bone segments are determined from the load-displacement curve resulting from mechanical testing experiments. Bone strength is more closely related to fracture risk than the elastic modulus, as it indicate how much load may result in permanent damage to bone and initiate mechanical failure.

Other than experiments, micro finite element (FE) analysis can estimate the elastic and yield properties computationally by simulating a mechanical test on the specimen-specific FE

model. Recent advances in high-resolution image technologies allows reconstruction of the three-dimensional trabecular microstructure with 10~80 μm voxels, which is fine enough to be used as input for the FE analysis. The assessment of bone strength using FE analysis will be discussed in Chapter 1.3.

Tissue modulus of trabecular bone can be measured using several experimental methods, including buckling experiments of dissected single trabecula, uniaxial tensile tests, bending tests, ultrasonic technique, back-calculation from FE analysis, microindentation and nanoindentation. Different methods have yielded various measurements of the elastic modulus of trabecular bone and cortical bone. The studies reported that, in general, trabecular bone tissue modulus is similar about 20~30% lower than cortical bone modulus.

1.1.4. Clinical Motivations

Osteoporosis is a common disease of aging, characterized by low bone mass and microstructural deterioration of trabecular and cortical bone that lead to increased bone fragility and susceptibility to fractures (NIH 2001). Approximately 9 million fragility fractures occur because of osteoporosis annually worldwide (Johnell and Kanis 2006). Measurement of aBMD by DXA is currently the accepted method for the diagnosis of osteoporosis and the assessment of fracture risk in postmenopausal women and men over 50 years old (Kanis 2002). However, measurement of aBMD has significant limitations in the prediction of prevalence or incidence of fractures, and in assessing the efficacy of pharmaceutical interventions that aim to reduce fracture risk (Delmas 2000, Siris, Miller et al. 2001, Stone, Seeley et al. 2003, Schuit, van der Klift et al. 2004). Studies in postmenopausal women show that half of all fractures occur in women with aBMD values above the WHO threshold for osteoporosis (*T*-score<-2.5) (Siris, Miller et al. 2001, Schuit, van der Klift et al. 2004). These findings suggest that aspects of bone

quality other than aBMD relate to fracture risk. The resolution of DXA is too low to distinguish trabecular and cortical compartments, or image bone microstructure, so there is great interest in developing high resolution imaging and analytical methods to investigate the microstructural and biomechanical basis of bone fragility and refine the prediction of fracture risk.

Mechanical strength of bone is directly related to risk of fractures, and is determined by bone mass, structure, and material properties. Mechanical testing of *ex vivo* bone specimens is considered the gold standard method to assess bone strength (Keaveny, Guo et al. 1994, Keaveny, Morgan et al. 2001). However, the experimental tests cannot be applied *in vivo*. μFE analysis based on high-resolution images of bone microstructure represents an alternative computational approach to assess bone stiffness (the ability to resist deformation) and bone strength (the breaking capacity) noninvasively (Niebur, Yuen et al. 1999, Niebur, Feldstein et al. 2000). Microstructure of the trabecular and cortical compartments can be imaged *in vivo* at fine resolution by recently developed clinical high-resolution peripheral quantitative computed tomography (HR-pQCT) (Boutroy, Bouxsein et al. 2005, Melton, Riggs et al. 2007). Based on the HR-pQCT images, patient-specific μFE models are created to provide accurate and direct estimate of bone's mechanical competence, such as stiffness and strength (Liu, Zhang et al. 2010, Christen, Melton et al. 2013). The accuracy of HR-pQCT and μFE analysis has been demonstrated in several validation studies and they have also been utilized in clinical studies to characterize differences in bone microstructure and mechanical competence between subjects with and without osteoporosis, and with and without a history of fractures (Boutroy, Van Rietbergen et al. 2008, Vilayphiou, Boutroy et al. 2010) . In postmenopausal women with fractures, HR-pQCT detected cortical thinning and reduced trabecular bone volume, with fewer and more widely spread trabeculae (Stein, Liu et al. 2010, Stein, Kepley et al. 2014). In addition,

μFE analysis has been shown to distinguish between postmenopausal women with and without previous fragility fractures (Nishiyama, Macdonald et al. 2013), suggesting the promise of HR-pQCT-based μFE analysis to become a powerful tool for the clinical assessment of bone strength and fracture risk.

Currently, the most common μFE modeling strategy is to convert each voxel from an image into a single finite element, in which way fine details of the bone microstructure is incorporated in the μFE model, but meanwhile resulting in a large-scale model with millions of elements which requires high computational capacity to perform the μFE analysis. The cumbersome voxel μFE models make the assessment of bone strength impractical for clinical use. In the current HR-pQCT, only estimates of bone stiffness is available derived from the linear μFE analysis, simulating bone deformation within the elastic range due to loading from daily activities. In order to simulate the failure behaviors of bone when overloaded beyond the elastic limit of the bone tissue, nonlinear μFE analysis is needed to derive bone's nonlinear properties such as yield strength or failure load, which are more directly reflective of bone's resistance to fractures than bone stiffness. The computational cost of the nonlinear μFE analysis of a HR-pQCT scan of distal radius or distal tibia is prohibitively high, requiring parallel computing for over 100 CPU hours (Christen, Melton et al. 2013, Christen, Zwahlen et al. 2014). Consequently, the assessment of bone stiffness is used as a surrogate, which compromises the prediction power for fracture risk. There is strong need for new modeling strategy that can provide estimate of bone strength from clinical available HR-pQCT scans in a highly efficient manner, accomplishable using regular computational capacity and applicable in clinical research.

1.2 Characterization of Trabecular Plate and Rod Microstructure

1.2.1 Imaging Technologies for Assessing Trabecular Bone Microstructure

Micro computed tomography (μCT) has become the gold standard for evaluation of bone morphology and microstructure. μCT uses x-ray attenuation data acquired at various viewing angles to reconstruct a three-dimensional representation of the specimen that characterizes spatial distribution of material density. Currently available μCT scanners have achieved an isotropic voxel size as low as a few micrometers, which captures the fine microstructure of individual trabeculae that are around 100~150 μm thick in human. μCT allows direct 3D measurement of trabecular morphology. Bone volume fraction (BV/TV) is calculated as the bone tissue volume divided by the specimen volume. Trabecular thickness (Tb.Th) is calculated based on distance transformation and maximal sphere fitting in the trabeculae. Similarly, trabecular spacing (Tb.Sp) is calculated based on maximal sphere fitting in the marrow space between trabeculae. Trabecular number (Tb.N) is defined as the inverse of the mean distance between the mid-axes of the trabeculae. Bone surface-volume ratio is defined as the bone surface divided by total bone volume within the region of interest. Structural model index (SMI) is developed to characterize the likeness of a 3D structure towards a plate (SMI=0) or rod (SMI=3). Degree of anisotropy (DA) indicates how the trabecular network is oriented. Connectivity density (Conn.D) describes the connectivity level of the structure normalized by size of the specimen. Other than bone morphology, μCT images can be used to estimate bone tissue mineralization by calibrating the x-ray attenuation with density of hydroxyapatite phantoms. The volumetric density measurement, together with high-resolution morphology of the bone determined from μCT scans, can be used to create μFE models to investigate mechanical behavior of bone.

Nevertheless, due to the high radiation dosage, μCT is prohibited from clinical application and only used for *ex vivo* human bone studies.

More recently, high-resolution quantitative peripheral computed tomography (HR-pQCT) has been developed that enables *in vivo* imaging of the trabecular and cortical microstructure at distal radius and distal tibia (Figure 1.1). It produces images with an isotropic voxel size of 82 μm, and reduced the radiation dosage to safety range for clinical application. Since HR-pQCT was introduced to the field a decade ago, there has been a dramatic increase in the number of studies demonstrating the clinical utility of HR-pQCT in investigating age-, sex- and race-related variations of bone quality, relationship between bone microstructure and fracture risk, osteoporosis and other bone diseases, and monitoring the effects of treatments on bone microstructure. The currently available scanner (XtremeCT; Scanco Medical, Brüttisellen, Switzerland) acquires an axial 9.02 mm section below the growth plate at distal radius and distal tibia, respectively. The cortical and trabecular compartments are separated automatically. Volumetric bone mineral density (vBMD) is determined for the whole bone, trabecular bone and cortical bone, based on pre-calibration using hydroxyapatite phantoms. Morphological analysis can be used to assess the microstructure of trabecular and cortical bone. However, because HR-pQCT resolution is close to the size of individual trabeculae, trabecular measurements are generally derived rather than directly measured from the images. BV/TV is determined from trabecular vBMD assuming the density of fully mineralized bone is 1200 mg HA/cm^3. Tb.N is measured directly using ridge extraction methods. Tb.Th and Tb.Sp are calculated from Tb.N and BV/TV (Tb.Th = (BV/TV)/Tb.N and Tb.Sp = (1-BV/TV)/Tb.N). Cortical thickness (Ct.Th) can be measured from the images based on distance transformation. The HR-pQCT measurements above are highly correlated with μCT measurements performed on cadaver

specimens. In addition to bone structure, bone stiffness can be estimated using FE analysis based on the HR-pQCT images, which has been validated with μCT-based FE models and mechanical testing experiments.

1.2.2 Individual Trabecula Segmentation (ITS)

A major hallmark of osteoporosis is the change from plate-like to rod-like trabecular bone network. It is believed that these two topologically different types of trabeculae have different contribution to the apparent mechanical properties of trabecular bone. However, standard μCT or HR-pQCT morphological analyses cannot determine trabecular type on the individual trabecula level. Although SMI indicates whether the trabecular structure is more plate- or rod-like, it cannot quantify the amount of trabecular plates and rods explicitly. Liu et al. developed individual trabecula segmentation (ITS) technique that decompose the trabecular network into individual trabecular plates and rods (Liu, Sajda et al. 2008). ITS was accomplished through digital topological analysis of the binary trabecular bone image based on the skeletonization and classification algorithms developed by Saha et al (Saha and Chaudhuri 1996, Saha, Chaudhuri et al. 1997). Skeletonization is an iterative erosion process where bone voxels are peeled off layer by layer until no more bone voxels can be removed without changing the shape or topology of the trabecular microstructure. Skeletonization transforms a trabecular bone image into a minimal representation of the microstructure composed of one-voxel thick surface and curves (Figure 1.2). The iteration number, representing the depth of the layer, was recorded for each voxel at the time of its removal (Saha and Chaudhuri, 1994; Saha et al., 1994). After skeletonization, digital topological classification is applied where each skeletal voxel is identified as a plate, rod, or junction type. The method of topological classification was based on the number of objects, tunnels, and cavities in the 3×3×3 neighborhood of a bone voxel after

hypothetically transforming the bone voxel to a marrow voxel (Saha and Chaudhuri, 1996). These topological parameters eventually lead to definitive determination of topological classes at every skeletal voxel (Figure 1.2B). In order to segment the plates, the surface-skeleton is further segmented into a network of curves, which are referred to as arcs to distinguish from previously mentioned rod curves (Figure 1.2C). By applying digital topological classification on the arc-skeleton, plate-plate junctions are identified. The plate-rod, rod-rod, and plate-plate junctions were removed to split the skeleton into individual branches, each of which represents a trabecular plate or rod as classified earlier. The final step of ITS is volumetric reconstruction of trabeculae, which is accomplished by a layer-by-layer reverse filling process of the non-skeletal voxels starting from the skeletal voxels (Liu, Sajda et al. 2006). During each iteration, the topological type of a candidate voxel is determined as the mean of the topological values of all previously reconstructed voxels in the 3×3×3 neighborhood. At the end of the reconstruction process, each bone voxel possesses a topological value, which represents the likelihood to be a plate- or rod-like structure, and it is labeled as belonging to an individual trabecular plate or rod (Figure 1.2D).

1.2.3 ITS-based Morphological Analysis of Plate and Rod Microstructure

Morphological parameters are evaluated directly from the measurements of individual trabeculae to characterize the morphological properties of trabecular plates and rods, respectively. The bone volume fraction (BV/TV), plate bone volume fraction (pBV/TV), and rod bone volume fraction (rBV/TV) are calculated as the volume of all trabecular bone, trabecular plates, and trabecular rods divided by the specimen volume, respectively. Mean trabecular plate thickness (pTb.Th) and mean trabecular rod thickness (rTb.Th) are directly measured from individual trabeculae.

The normal to a trabecular plate was determined as the surface normal to a plane representing surface skeleton using least square fitting. At each voxel of the surface skeleton, a local thickness is calculated along the normal, and the thickness of a trabecular plate is determined by averaging local thickness of all the voxels on the surface skeleton. The orientation of a rod is obtained from 3D principal component analysis on its curve skeleton. Local diameters are determined for all the voxels of the curve skeleton, and their average is defined as the diameter of the rod. Trabecular plate and rod number (pTb.N and rTb.N) are defined as the cubic root of the total number of plates or rods divided by the specimen volume. Average trabecular plate surface area (pTb.S) and average trabecular rod length (rTb.L) are derived from the volume of trabecular plates and rods, along with their thickness and diameter, respectively. The plate-plate, plate-rod, and rod-rod junction densities (P-P, P-R, R-R Junc.D.) are calculated as the total number of those junctions normalized by the specimen volume. In addition, axial bone volume fraction (aBV/TV) is evaluated to characterize the bone volume aligning with the axial direction of the specimen.

The ITS morphological analysis was validated and applied on both micro computed tomography (μCT) and clinical HR-pQCT images (Liu, Sajda et al. 2008, Liu, Zhang et al. 2010, Liu, Shane et al. 2011). Studies using this ITS demonstrated that trabecular microstructure change from plate-like to rod-like in osteoporosis and other metabolic bone diseases, and suggest that a conversion from plate-like to rod-like trabecular bone is an important etiologic factor for age- and osteoporosis-related bone fragility (Liu, Cohen et al. 2010, Wang, Zhou et al. 2013). Liu et al. reported that Chinese American women have more plate-like trabecular structure than Caucasian American women, which could account for the greater mechanical competence and lower fracture risk in Chinese-American women (Liu, Walker et al. 2011). ITS morphological parameters also reveal differences in trabecular plate and rod microstructure between Chinese,

Hispanic and Caucasian women (Zhou, Wang et al. 2014). In addition, the ITS technique has demonstrated the importance of trabecular plates and axial trabeculae in supporting mechanical loads imposed on human vertebrae (Liu, Bevill et al. 2009). ITS morphological parameters have the ability to discriminate postmenopausal women with fragility fractures from those without any fractures, whereas aBMD measurements by DXA cannot distinguish the two groups (Liu, Stein et al. 2012). Stein EM et al suggested trabecular plate loss is the most pronounced trabecular bone abnormality in fractured postmenopausal women with osteopenia, who have an aBMD T-score between -2.5 and -1 (Stein, Kepley et al. 2014). The osteopenic subgroup account for 80% of the total fragility fractures, but their risk of fracture cannot be properly identified by DXA. Other technologies, such as the standard or ITS morphological analysis based on HR-pQCT, are needed to better assess the bone quality and fracture risks.

1.3 Finite Element Modeling of Human Bone

1.3.1 High-Resolution Image Based Finite Element Models

Based on high-resolution 3D images of bone, specimen-specific μFE models are constructed by a direct conversion of each bone voxel to an 8-node brick element. This μFE modeling approach has become a prevailing method for estimating the mechanical properties of trabecular bone. Initially, μFE analysis of bone was applied to solve the linear case and evaluate elastic properties (Hollister, Brennan et al. 1994). Then, efforts were made to incorporate bilinear material property and develop nonlinear μFE analysis algorithm to predict yield strength of trabecular bone (Niebur, Yuen et al. 2001). Nonlinear μFE analysis provides a powerful tool to study the failure behavior of bone under various loading conditions, which helps better understand the biomechanical mechanisms of fractures (Bevill, Eswaran et al. 2006). Nawathe et al. used nonlinear μFE analysis to investigate the initiation and propagation of failure within

human proximal femur during a sideways fall impact and quantified the relative contributions of trabecular and cortical bone to the load-carrying capacity in femoral neck (Nawathe, Akhlaghpour et al. 2014, Nawathe, Nguyen et al. 2015). In clinical studies, nonlinear μFE analysis has also been used to examine the effects of osteoporosis treatments on femoral and vertebral strength (Keaveny, McClung et al. 2014). Since the introduction of HR-pQCT, μFE analysis has been widely used based on HR-pQCT images to evaluate the mechanical properties of distal radii and tibiae. Validation studies demonstrated that mechanical stiffness predicted by HR-pQCT-based μFE models is highly consistent with those measured by mechanical testing, and those predicted by corresponding μCT-based μFE models (Macneil and Boyd 2008, Liu, Zhang et al. 2010, Zhou, Wang et al. 2016). Furthermore, the stiffness of radii and tibiae estimated by HR-pQCT are proved to be an important factor that indicates the risk of osteoporotic fractures in postmenopausal women (Boutroy, Van Rietbergen et al. 2008, Vilayphiou, Boutroy et al. 2010).

Although HR-pQCT provides evaluation of the elastic bone stiffness, it is impractical to predict bone's nonlinear mechanical properties, such as yield strength, using the μFE modeling approach. Due to the simple voxel to element modeling strategy, a μFE model of the distal radius has approximately 2 million elements, which requires about 1 hour of CPU time for a linear μFE analysis and 45 hours of CPU times for a nonlinear μFE analysis on a 3.0 GHz computer. Such heavy computational tasks need to be accomplished by parallel computers, which are not widely accessible and certainly not practical for clinical application. In order to assess bone strength which is more relevant to fracture risk than stiffness, two approaches have been explored in consideration of avoiding large-scale nonlinear μFE computation. The first approach aims to estimate the failure load from linear μFE simulation assuming fracture occurs when 2% of the

total bone volume is strained over a critical level of 7000 microstrain. Pistoia et al. reported moderate agreement between the estimated failure load and that measured by mechanical testing ($R^2 = 0.75$) and overestimation of the failure load by 29% using this approach as compared to experimental measurements (Pistoia, van Rietbergen et al. 2002). The second approach aims to develop a simplified microstructural model for the trabecular bone, which will reduce the size of the FE models and therefore reduce the computational cost of μFE analyses. This approach allows direct prediction of bone strength using nonlinear μFE analysis rather than estimating from the linear case. The more efficient FE model will enable its application in a wider range of research contexts and even in clinical use for assessing bone strength. More details of this approach is discussed in Chapter 1.3.2.

1.3.2 Simplified Plate and Rod Finite Element Models

From a biomechanical perspective, the microstructure of trabecular bone consists of a collection of trabecular plates and rods. As discussed in Chapter 1.2.3, the segmentation of trabecular plates and rods demonstrated close relationship between the microstructure and mechanical properties of trabecular bone, our laboratory hypothesized that the simplified representation of trabecular plates and rods would be sufficient to model the trabecular microstructure and to be subjected to μFE analysis for predicting the mechanical properties of trabecular bone. On the basis of segmented plate and rod skeletons, shell and beam elements are created to model trabecular plates and rods, respectively. The PR modeling strategy can maintain essentially all the plate and rod microstructure, which includes the number, shape, volume, orientation of trabecular plates and rods, as well as the connections between plates and plates, plates and rods, and rods and rods. Compared to traditionally used voxel μFE models, the PR models have substantial advantage in computational efficiency, because the model size would be

significantly reduced by meshing plates and rods using shell and beam elements, instead of converting each of the voxels into an element. The highly efficient PR models will facilitate μFE analysis in the prediction of not only linear but also nonlinear mechanical properties for large bone specimens of interest, such as vertebral bodies, proximal femur, distal tibiae, or distal radius, which otherwise requires large-scale parallel computing using the voxel μFE models. Furthermore, the accuracy of PR models would increase our understanding of the biomechanical roles of trabecular plates and rods and clarify the basic science question about whether trabecular plates and rods can fully determine the apparent mechanical properties of trabecular bone.

The plate-rod modeling strategy was first tested in idealized plate and rod microstructure, which allowed fundamental verification of the feasibility of the plate-rod modeling independent of biological variations and image noise (Wang, Liu et al. 2013). Idealized plate-rod and rod-rod microstructure over a wide range of thicknesses (80 μm, 160 μm, 240 μm, and 320 μm) were constructed at typical resolutions of μCT (20 μm, 40 μm) and HR-pQCT (80 μm) images. A PR model with shell and beam elements representing plates and rods, respectively was created for each image, and compared with μFE analysis results from the voxel model. Results showed that the stress-strain curves of the PR models under uniaxial compression up to 1.5% strain was highly consistent with those of voxel models for the plate-rod structure with elements of varying thickness and rod-rod structure with thin elements. However, deviation was pronounced in rod-rod structure with trabecular thickness of 240 μm and 320 μm, suggesting PR models to be less stiff for thick rod structure. The Young's modulus and yield strength predicted by simplified PR models strongly correlated with those of voxel models from 20 μm to 80 μm resolutions. The conversion from voxel models to PR models resulted in an approximately 762-fold reduction in the largest model size and significantly accelerated the nonlinear FE analysis. The excellent

predictive power of the PR μFE models that was demonstrated in an idealized trabecular microstructure provided a prevailing basis for its further development in real trabecular bone images to assess the mechanical properties of trabecular bone.

1.4 Assessment of Heterogeneous Bone Tissue Mineralization

1.4.1 Tissue Mineral Density Distribution

Tissue mineral density (TMD) and its heterogeneous distributions are key determinants of the intrinsic mechanical properties of trabecular bone tissue (Roy, Rho et al. 1999, Jaasma, Bayraktar et al. 2002). The nonuniform TMD in trabecular bone tissue results from frequent bone remodeling and dynamic mineralization kinetics in newly formed bone packets. Microradiography was the first technique to visualize and quantify the local variation in mineral content within cortical and trabecular bone. More advanced techniques, such as quantitative backscattered electron imaging (qBEI) and synchrotron radiation micro computed tomography (SRμCT) have been developed since then. These imaging techniques show that newly formed bone packets on the bone surface exhibit a lower mineral content as compared to older bone in the center of trabeculae. For a quantitative analysis of mineralization variations throughout the bone tissue, the bone mineral density distribution is defined as a histogram of mineral content in voxels within the region of interest. The bone mineral density distribution is usually characterized by the average, peak, width of distribution, amount of lowly mineralized bone, amount of highly mineralized bone. Normal healthy adults have a characteristic TMD distribution regardless of gender, age and race. Many bone metabolic diseases, e.g., osteoporosis and osteomalacia, are associated with distinct deviations from the reference TMD distribution of healthy individuals (Roschger, Gupta et al. 2003, Roschger, Paschalis et al. 2008). Additionally, patients with fragility fractures at hip and spine have more heterogeneous bone mineralization than the nonfracture control subjects (Ciarelli,

Fyhrie et al. 2003, Loveridge, Power et al. 2004, Seitz, Koehne et al. 2013). These findings suggest significant basic science and diagnostic value for evaluating the distribution of TMD, but knowledge is lacking regarding factors that contribute to the heterogeneity of TMD. Bone mineralization has not yet been investigated on the individual trabecular level. It is unclear whether individual trabecular TMD varies with trabecular types and orientations.

1.4.2 Heterogeneous Finite Element Models of Trabecular Bone

In μFE modeling, bone tissue is normally assumed as isotropic material with homogeneous tissue modulus, which does not account for the local variation in bone mineral content. However, in certain patients, such as those with chronic kidney diseases or on long-term bisphosphonate therapy, alterations in the degree of bone mineralization may have a profound influence on bone tissue mechanical properties, and therefore, on the apparent mechanical properties calculated by μFE analysis. Studies have been performed in order to investigate the effects of heterogeneous mineralization on the apparent mechanical properties of trabecular bone. The heterogeneous TMD distribution is either hypothesized or acquired from μCT and SRμCT attenuation data by converting the grayscale value to mineral density. The relationship between TMD and tissue modulus is usually determined by microindentation, nanoindentation and empirical models. These studies showed that the heterogeneous mineralization affects the apparent elastic properties of trabecular bone. It is suggested that the incorporation of mineral heterogeneity in μFE models results in a reduction in apparent stiffness. Nevertheless, the extent of this reduction is not consistent and varied from 2% to 20% depending on the mineralization distribution model used in those studies (Bourne and van der Meulen 2004, Chevalier, Pahr et al. 2007, Harrison, McDonnell et al. 2008, Gross, Pahr et al. 2012). Another recent HR-pQCT longitudinal study of premenopausal women with idiopathic osteoporosis (IOP) treated with the

anabolic agent, teriparatide suggested that heterogeneous μFE models that account for tissue heterogeneity were more sensitive in detecting improvements in both stiffness and failure load (Nishiyama, Cohen et al. 2014). Therefore, it is important to incorporate trabecula-specific tissue elastic modulus in the PR μFE models, such that not only the microstructure but also the heterogeneous material properties of trabecular bone are well preserved to further refine the prediction of apparent mechanical competence by PR model-based μFE analysis.

ITS technique provides a well validated method to segment the trabecular network and determine the orientation of plates and rods. By combining high-resolution three-dimensional μCT imaging and ITS analysis, it is possible to directly measure the TMD of individual trabecular plates and rods, and to elucidate the heterogeneous distribution of minerals in relation to trabecular structural type and orientation. Elastic modulus of individual trabecular plates and rods can be determined by its linear relation with TMD and assigned to the corresponding shell and beam elements in PR μFE models. The impact of a heterogeneous distribution of bone tissue properties on image-based μFE analysis will be assessed.

1.5 Specific Aims and Organization

1.5.1 Specific Aims

Specific aim 1: Develop plate-rod (PR) modeling technique for the assessment of human trabecular bone strength and evaluate μCT-based PR μFE models for predicting the Young's modulus and yield strength of human trabecular bone in comparison with voxel μFE models and mechanical testing experiments

Hypothesis 1: The PR μFE models are able to predict the Young's modulus and yield strength of human trabecular bone, which are indistinguishable from those estimated by voxel μFE models or measured from mechanical testing.

Specific aim 2a: Develop individual trabecula mineralization (ITM) technique to determine tissue mineral density (TMD) of individual trabeculae and investigate variations in TMD with respect to trabecular types and orientations.

Specific aim 2b: Evaluate the effects of TMD heterogeneity on the apparent mechanical properties of trabecular bone in the PR μFE models.

Hypothesis 2. Mineral heterogeneity is related to the types and orientations of individual trabeculae, and has a significant impact on the apparent mechanical properties of trabecular bone.

Specific aim 3a: Adapt the PR modeling technique for application on the HR-pQCT images of trabecular bone, and develop whole bone PR modeling of distal radii and distal tibiae that incorporates both the trabecular and cortical bone.

Specific aim 3b: Evaluate the HR-pQCT-based PR μFE models for predicting the stiffness and yield force of the trabecular bone and whole bone, respectively, in comparison with the estimations from voxel μFE models and direct measurements from mechanical testing.

Hypothesis 3: The PR μFE models based on the HR-pQCT images of distal radii and tibiae are able to predict the stiffness and strength of the whole bone and trabecular bone compartments, which are indistinguishable from those predicted by the voxel μFE models or measured from mechanical testing.

Specific aim 4: Apply the PR μFE models developed in Aims 3 to *in vivo* HR-pQCT images and determine the effectiveness of the bone strength assessment in distinguishing between postmenopausal women with vertebral fractures and their non-fractured peers.

Hypothesis 4: The assessment of bone strength by the HR-pQCT-based PR μFE models is able to discriminate the fracture status in postmenopausal women.

1.5.2 Organization

This thesis is organized based on a framework consisting of the research conducted for addressing each of the specific aims above. The development and validation of the μCT-based PR μFE models of trabecular bone is discussed in Chapter 2. The development of ITM analysis and heterogeneous PR μFE models is discussed in Chapter 3. The development and validation of the HR-pQCT-based PR μFE models of whole bone segment is discussed in Chapter 4. The application of PR μFE models on *in vivo* HR-pQCT images in postmenopausal women with andwithout fractures is discussed in Chapter 5.

In Chapter 2, the PR modeling algorithm is introduced and first applied on μCT images of human trabecular bone. Specimens from proximal tibia, femoral neck, and greater trochanter were obtained from human cadavers. For each specimen, a 3D image of the trabecular microstructure is reconstructed by μCT at 30 μm voxel size. Then, a PR μFE model is constructed from the μCT image by meshing individual trabecular plates and rods into shell and beam elements, and a voxel μFE model is constructed from direct conversion of each voxel of the image to an element. The trabecular bone specimens are then subjected to mechanical testing. The Young's modulus and yield strength predicted by the PR models are compared with those predicted by the voxel models and mechanical testing. The accuracy and efficiency of the PR μFE models are evaluated in comparison with computational and experimental references.

In Chapter 3, the TMD of individual trabeculae is quantified by the ITM analysis. The distribution of TMD in trabecular plates is compared with that in trabecular rods. Also, the TMD of trabeculae oriented along different directions is analyzed. The variations in TMD associated with trabecular types and orientations are examined in SRμCT and μCT evaluations of bone mineralization, respectively. Furthermore, PR μFE models that incorporate mineral heterogeneity are compared with homogeneous PR models in estimating the apparent mechanical properties of trabecular bone.

In Chapter 4, the PR modeling technique is refined to accommodate the lower resolution of HR-pQCT as compared to μCT, and whole bone PR models are developed by connecting the PR models of the trabecular compartments inside the distal radii and tibiae with the coarsened models of the cortical bone. 30 human radii and 30 tibiae specimens were machined into 9.02 mm segment, scanned using μCT and HR-pQCT, and then loaded to failure in compressive tests. The accuracy of whole bone and trabecular bone PR models based on HR-pQCT in predicting bone stiffness and strength is evaluated by comparison with the estimations from voxel μFE models based on HR-pQCT and μCT, along with the direct measurements from mechanical testing.

In Chapter 5, the whole bone PR models are applied to *in vivo* HR-pQCT images to test the effectiveness of the estimated bone strength in discriminating postmenopausal women with vertebral fracture from non-fractured controls. 45 fracture subjects and 45 controls were included in this study. HR-pQCT images were acquired at 82 μm voxel size. aBMD of each subject was measured by DXA. Trabecular and cortical microstructure were analyzed using ITS and a custom cortical bone evaluation script. Stiffness and yield force of the whole bone section and the trabecular bone compartment were estimated by the PR μFE models. The predictive power of

aBMD, ITS morphological parameters, cortical structure, and mechanical strength were evaluated respectively in distinguishing between the fractured and non-fractured subjects. Finally, Chapter 6 summarizes the key findings from the thesis research and suggestions for future studies.

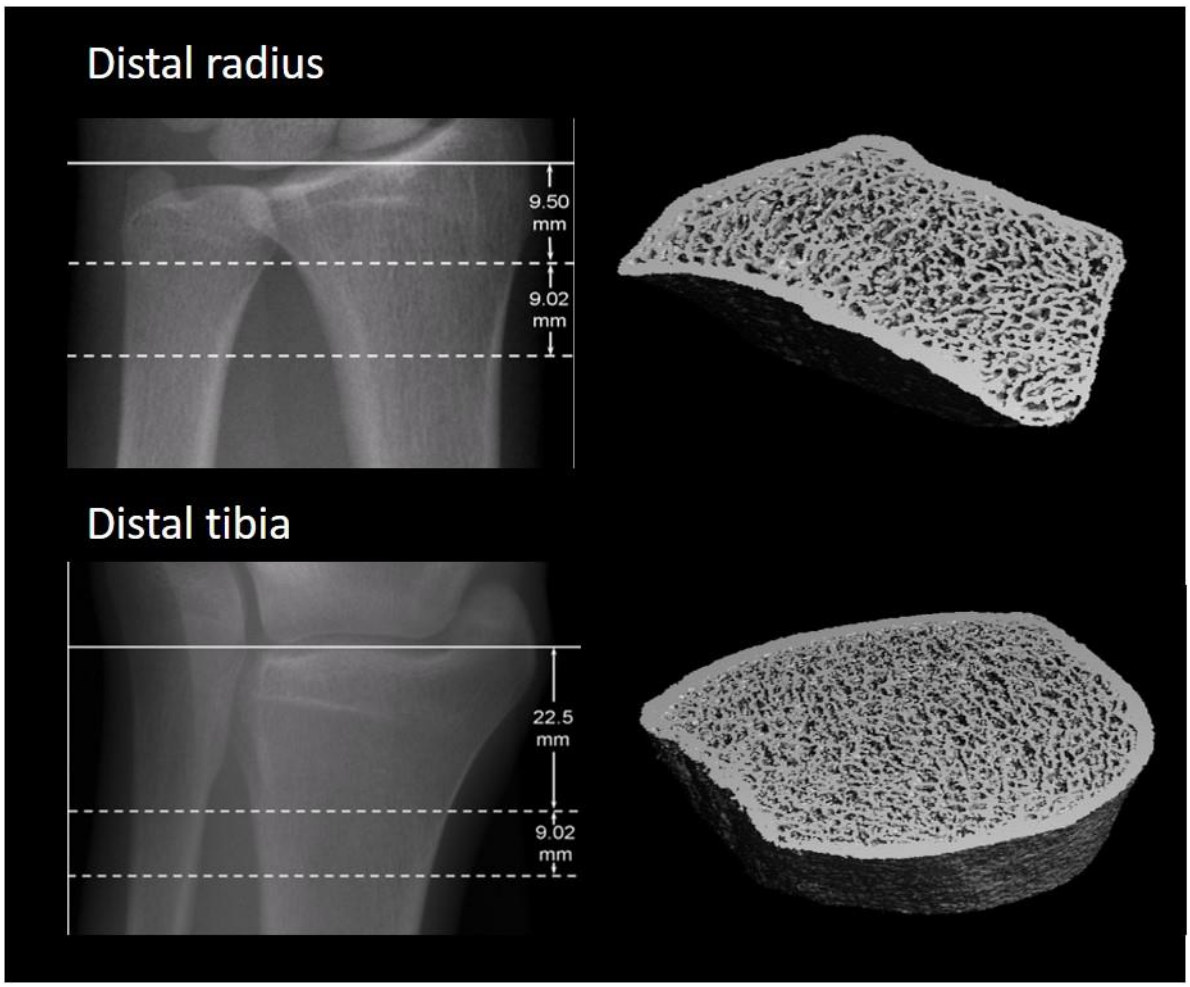

Figure 1.1. HR-pQCT region of interest at distal radius and tibia (left) and reconstructed 3D bone structure images (right)

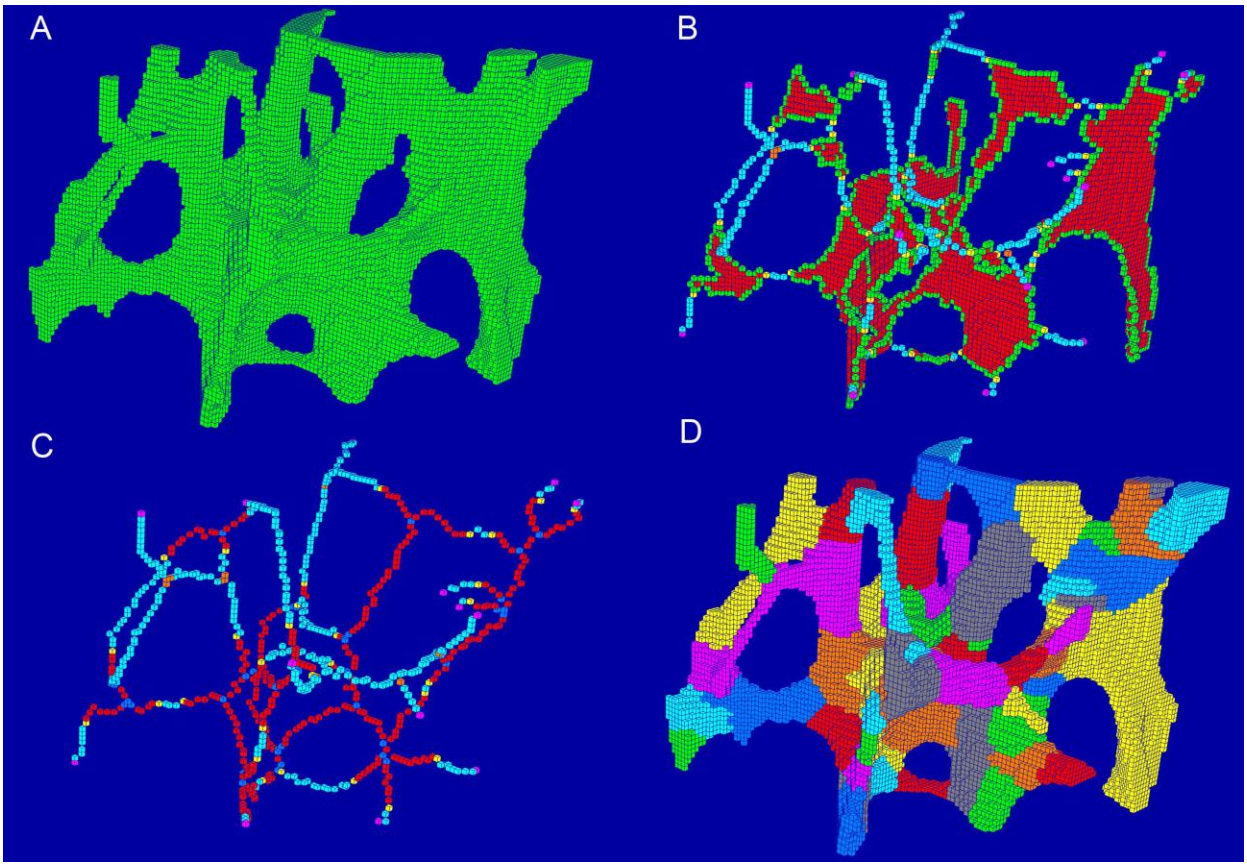

Figure 1.2. Illustration of the process of individual trabecula segmentation (A) digital μCT image; (B) skeleton of the trabecular plate (inner plate in red, and plate edge in green) and rod (light blue) structure; (C) arc skeletons of trabecular plates (red) and rod curve skeletons (light blue); (D) fully segmented individual trabeculae with the original volume.

Chapter 2. Plate-rod microstructure modeling for human trabecular bone

2.1. Introduction

Osteoporosis is a common disease that occurs with age, in which reduced bone mass and strength leads to increased risk of fracture. Millions of fragility fractures occur directly because of osteoporosis, often at trabecular-dominant bone sites. Indeed, the trabecular bone plays an important role in load transmission and energy absorption in major joints such as the knee, hip, and spine (Harada, Wevers et al. 1988, Hvid 1988, Keaveny, Wachtel et al. 1994). For example, the trabecular bone carries more than 75% of the load in a vertebral body (Eswaran, Gupta et al. 2006). It is believed that, in addition to the bone volume fraction (the ratio of the volume of bone tissue to the overall bulk volume), the detailed microstructure, including trabecular orientation and connectivity, is important in governing the mechanical properties of trabecular bone (Liu, Sajda et al. 2006, Liu, Zhang et al. 2009, Shi, Liu et al. 2010, Fields, Lee et al. 2011). Moreover, two major types of trabeculae – namely the trabecular plate and rod – play critical and distinct roles in determining the apparent strength and failure behavior of trabecular bone. Recently, an individual trabecula segmentation (ITS) analysis technique has been developed to decompose the entire trabecular bone network into a collection of individual plates and rods. The ITS technique was further used to assess trabecular plate and rod morphology of both micro computed tomography (μCT) and high resolution peripheral quantitative computed tomography (HR-pQCT) images of human trabecular bone (Liu, Sajda et al. 2008). Studies using this ITS technology demonstrated that trabecular microstructure changed from plate-like to rod-like in osteoporosis and other metabolic bone diseases, and suggested that a conversion from plate-like to rod-like trabecular bone was an important etiologic factor in age- and osteoporosis-related

bone fragility (Liu, Bevill et al. 2009, Liu, Cohen et al. 2010, Liu, Shane et al. 2011, Liu, Stein et al. 2012). The ITS technique has also demonstrated the importance of trabecular plates and axial trabeculae in supporting mechanical loads imposed on human vertebrae (Fields, Lee et al. 2011). Furthermore, ITS-based morphological analysis can detect microstructural abnormalities in postmenopausal women with fragility fractures independent of areal bone mineral density (aBMD) (Liu, Stein et al. 2012) and reveal dramatic differences in trabecular microstructure between different ethnicities (Liu, Walker et al. 2011, Zhou B and Zhang CA 2014).

It has been demonstrated that the ITS-based morphological parameters such as plate bone volume fraction (pBV/TV) and axial bone volume fraction (aBV/TV) are highly correlated with experimentally and computationally determined elastic modulus and yield strength of human trabecular bone (Liu, Sajda et al. 2008, Zhou, Liu et al. 2014). To further examine the biomechanical roles of trabecular plates and rods, ITS-based, specimen specific, plate-rod (PR) micro finite element (μFE) modeling strategy was developed. These PR μFE models are constructed exclusively by ITS plate and rod segmentations, maintaining essentially all the plate and rod microstructure: number, shape, volume of trabecular plates and rods, and orientation and connectivity between trabecular plates-plates, plates-rods, and rods-rods. Alternatively, specimen specific, voxel-based μFE models do not make any assumption regarding trabecular types but fully represent the original 3D trabecular microstructure. Recently, the accuracy and efficiency of the PR modeling strategy were examined in an idealized, synthetic trabecular bone structure model, and demonstrated that the Young's modulus that was predicted by the ITS-based PR model correlated strongly with those by the voxel-based model at various voxel sizes (Wang, Sherry Liu et al. 2013). Additionally, conversion from the voxel model to the PR model resulted in a 47-fold reduction in the number of elements (Liu, Wang et al. 2013). Independently, Vanderoost *et al.*

developed specimen-specific skeleton based beam-shell μFE models for simulating trabecular bone elastic modulus (Vanderoost, Jaecques et al. 2011). However, from a biomechanical perspective, it is not clear whether the simplified trabecular plate and rod morphology alone sufficiently represents the 3D microstructure of human trabecular bone. To determine whether the simplified PR model can accurately predict the mechanical properties of the complex human trabecular bone structure, a thorough validation of the PR model against the "gold standard" mechanical testing is required.

The purpose of this study was to compare the predictions in elastic modulus and yield strength of the μCT PR model, which was based completely and explicitly on ITS plate and rod segmentations and reconstructions, with those determined by mechanical testing as well as by μCT-image-based voxel model, the computational "gold standard" measurements. In addition, I aimed to demonstrate that the ITS-based PR FE model provides a highly efficient and alternative method to predict both linear and nonlinear mechanical properties of human trabecular bone. I hypothesized that the plate and rod morphology are the most critical determinants of the mechanical properties of human trabecular bone; thus, the simplified PR FE model that consists of only plate and rod elements can accurately predict the Young's modulus and yield strength of human trabecular bone.

2.2. Materials and Methods

2.2.1. Specimen preparation and μCT scanning

Fifteen sets of freshly frozen human cadaveric tibiae (11 male/4 female, age: 71 ± 9 years, ranged from 55 to 84 years old) and fifteen sets of proximal femurs (8 male/7 female, age 73 ± 14 years, ranged from 40 to 91 years old) were obtained from the International Institute for the

Advancement of Medicine (Scranton, PA) with no history of bone related metabolic diseases. Contact X-ray radiography was performed to verify that there was no fracture in the specimens. Cylindrical trabecular bone cores with a diameter of ~8.5 mm were prepared from proximal tibiae and femurs along the main trabecular orientation (Morgan and Keaveny 2001). In total, 22 proximal tibia (PT), 20 femoral neck (FN) and 20 greater trochanter (GT) trabecular bone cores were prepared. Specimens were kept in sealed plastic bags at -20°C and wrapped with wet gauze between preparations. These specimens were also described in our previous work (Zhou B and Zhang CA 2014). The specimens were scanned along the cylindrical axis using a μCT scanner (*VivaCT* 40, Scanco Medical AG, Basserdorf, Switzerland) at 15 μm voxel size with 55 kVp energy and 200 ms integration time. The middle 13 mm trabecular bone of the cylinder was scanned to assure that the 8 mm strain gage region in mechanical testing was included in the μCT image. The grayscale images corresponding to the 8 mm strain measurement region were then down sampled to 30 μm voxel size and thresholded for further processing.

2.2.2. Mechanical testing

After μCT scanning, the bone marrow near the two ends of the bone cores was cleaned out with a water jet. The specimens were then glued into customized brass cylindrical end caps with the inner diameter the same as the diameter of trabecular bone cores. The specimens were pushed to the bottom of the end cap to eliminate movement during mechanical testing and to reduce end-artifacts (Keaveny, Guo et al. 1994). A uniaxial compression test was performed on each core to measure the mechanical properties (MTS 810, Eden Prairie, MN) at room temperature, while keeping the specimen hydrated. An 8 mm strain gage (MTS, 632.26F-20) was attached to the middle of the specimen to measure strain. To ensure uniform deformations between the end caps and no yielding at the endcap-bone interface, a 25 mm extensometer (MTS 634.11F-24) was

attached to the end caps. The specimen was preconditioned by 3 cycles with a 0.05% strain per second loading speed and a final ramp beyond the yield point. The elastic modulus was calculated by the linear curve fit within a 0-0.2% strain range. The yield strength and the yield strain were calculated using a 0.2% offset technique (Keaveny, Guo et al. 1994).

2.2.3. Voxel-based μFE models

The down sampled and thresholded μCT images of trabecular bone were converted to μFE models by converting each voxel to 8-node brick element. It should be noted that voxel μFE models were based on the original μCT images of trabecular bone. A uniaxial compression test was simulated through μFE analysis (μFEA), and fixed boundary conditions were assigned to the nodes at the two ends of the model. The bone tissue constitutive law was prescribed based on the elasto-plastic material model that incorporates geometric large deformations and material non-linearity (Papadopoulos and Lu 1998, Papadopoulos and Lu 2001). Poisson's ratio was defined as 0.3, and a 15 GPa tissue modulus was applied. The tissue-level yield strains were assumed to be 0.81% of strain in tension and compression (Bayraktar, Morgan et al. 2004). The post-yield tissue modulus was 5% of its initial value. An implicit parallel finite element framework, Olympus (Adams 2004), was used to solve the nonlinear μFE models on a Sun Constellation Linux Cluster at the Texas Advanced Computing Center. For each model, the apparent modulus was calculated from the slope of the linear curve fit of the stress-strain curve. The yield strength and yield strain were determined using the 0.2% offset technique (Keaveny, Guo et al. 1994).

2.2.4. PR μFE models

PR μFE models were constructed from the ITS segmented and reconstructed μCT image of each trabecular bone specimen (Figure. 2.1). Through the PR modeling procedure, individual trabecular plates and rods were meshed into shell and beam elements, respectively. First, the μCT

image of trabecular microstructure (Figure. 2.1A) underwent an iterative thinning process and generated the skeleton image, consisting of the central axes of trabecular rods and the medial surfaces of trabecular plates (Figure. 2.1B) (Saha and Chaudhuri 1994, Saha, Chaudhuri et al. 1994). Then, the entire skeleton was decomposed into individual plate and rod skeletons with every voxel uniquely classified as inner plate, plate edge, inner rod, rod end and junction points based on digital topological analysis (DTA) and ITS (Figure. 2.1B) (Saha and Chaudhuri 1996, Saha, Chaudhuri et al. 1997). Using ITS segmentation, both curve and surface skeletons were segmented into individual pieces (Figure. 2.1C) and recovered to their full bone volume with individual trabecular plates and rods (Figure. 2.1D). The skeleton and reconstructed ITS images of trabecular bone were further processed for generation of PR μFE model based exclusively on the plate and rod assumption (Figure. 2.1E, F). Plate-plate junction, rod-rod junction, plate-rod junction, rod end and plate edge junction points were used as connection nodes in the PR model. In addition, the key turning points on plate edges and rod curves were identified as shape-refining nodes in the PR model. Each trabecular rod was meshed into a beam element with two nodes connecting this rod to its neighboring trabeculae. A curvy rod was further divided into segments by the key turning points on the rod curve, so the curvature of trabecular rods could be preserved in the PR model (Figure. 2.2). Each trabecular plate was meshed into multiple triangular shell elements through Delaunay Triangulation using the node set of plate-plate junction, plate-rod junction, plate edge junction and turning points on the plate edges (Figure. 2.3). Delaunay triangulation algorithm follows the "empty circle" principle that the circumcircle of each triangle does not contain any of the other nodes, therefore avoids thin triangles (Delaunay 1934). By incorporating both connection nodes and shape-refining nodes, the connectivity and shape of each individual trabecular plates and rods were fully preserved in the PR model. The segmented trabecular plate and rod skeleton

was recovered layer by layer to the original volume of trabecular bone microstructure. Each voxel was determined as part of a trabecular plate or rod. Thickness of a trabecular plate was calculated from its volume divided by the sum of area of the triangular shell elements associated with this plate. Thickness of a trabecular rod, namely diameter of its corresponding cylindrical beam elements, was calculated from the rod volume and the sum of length of the beam elements. Therefore, the shell and beam elements in the PR model maintained the original volume of each trabecular plates and rods. It should be noted that the thickness of shell and beam elements was not shown in the model.

ABAQUS 6.10 (Dassault Sytemes USA, Waltham, MA) software was used to perform finite element analysis on the PR model. Shell and beam elements were defined as STRI3 and B31 elements in the ABAQUS library, respectively. Trabecular bone tissue was assumed to have elastic modulus of 15 GPa and Poisson's ratio equal to 0.3, the same as the voxel model. In the PR model, trabecular bone tissue was assumed to yield at 0.81% strain with a post-yield modulus equal to 5% of the elastic modulus. A compression test along the longitudinal axis of trabecular bone core was simulated up to 1% apparent strain. Elastic modulus of the PR model was determined as the slope of the linear curve fit for the stress-strain curve in elastic range. The yield strength and yield strain were determined using the 0.2% offset method (Keaveny, Guo et al. 1994). PR models were compared with those by voxel models for the trabecular bone specimens from PT, FN and GT, as shown in Figure. 2.4.

2.2.5. Predictions of anisotropic mechanical properties by PR μFE model

In order to test the ability of the PR μFE model in characterizing and quantifying 3D anisotropic trabecular bone microstructure, a $5.1\times5.1\times5.1mm^3$ cubical sub-volume was extracted from each μCT image of a randomly select subgroup of specimens, including 10 FN specimens,

10 PT specimens, and 10 GT specimens. The z axis was aligned with the longitudinal axis of the bone core, and x, y axes were orthogonal in the transverse plane. Voxel models and PR models were generated for the cubical sub-volumes, as described before. Three uniaxial compression tests were performed along x, y and z axes, respectively. Elastic modulus (E_x, E_y, E_z) and yield strength (σ_x, σ_y, σ_z) along x, y and z axes were predicted by both PR μFE model and voxel model.

2.2.6. PR model of distal tibia and distal radius

The accuracy of PR models was further tested on a separate and independent set of μCT images of trabecular bone from the distal tibia (n=15) and distal radius (n=15), which corresponded to the scan region under clinical HR-pQCT protocol. Cylindrical sub-volume (8.5 mm diameter, 8 mm length) was extracted from the μCT images at 37 μm voxel size. PR model and voxel model were generated and subjected to nonlinear FE analysis. The elastic moduli and yield strengths predicted by PR models were compared with those by corresponding voxel models.

2.2.7. Statistical analyses

Statistical analyses were performed using NCSS software (NCSS 2007, NCSS Statistical Software, Kaysville, Utah). Descriptive data were presented in the form of mean ± standard deviation (SD). Elastic modulus and yield strength predicted by PR models were correlated with those derived from voxel models and measured directly from mechanical testing experiments. Paired T-test was applied to examine the difference among PR model predictions, voxel model predictions and experimental measurements. Two-sided p values <0.05 were considered to indicate statistical significance. Bland-Altman plots were shown to present the agreement of the

PR model relative to mechanical testing experiment and voxel model. The relative difference between two methods (difference/average) was plotted versus their average.

2.3. Results

Both PR and voxel μFE models predicted the stress-strain behavior of human trabecular bone as measured experimentally. The elastic modulus and yield strength predicted by the PR μFE model were not different from those experimentally measured by mechanical testing ($p>0.15$) across different anatomic sites (Table 2.1). Strong correlations were found between the PR model predictions and those measured experimentally (Young's modulus: $R^2 = 0.97$; Yield strength: $R^2 = 0.96$, Figure. 2.5A and C). With reference to experimental measurements, the PR model had an average error of 0.00 (-0.24~0.24, 95% agreement limit) in predicting elastic modulus and error of 0.02 (-0.32~0.37) in predicting yield strength (Figure. 2.6A and C). In addition, PR model predictions in elastic modulus and yield strength strongly correlated with those of voxel models, which were based on original μCT trabecular bone microstructure ($R^2 = 0.99$ and 0.98, respectively), as shown in Figure. 2.5B and D. Excellent agreement was found between PR model and voxel model in predicting elastic modulus with a relative error of 0.02 (-0.14~0.20), whereas PR model underestimated yield strength that was determined by voxel model by around 21% (error: -0.44~0.01, $p<0.001$, Figure. 2.6B and D). It was also noted that voxel model overestimated yield strength relative to mechanical testing measurements by around 23% (error: -0.04~0.50, $p<0.001$). Table 2.2 showed comparison between the original trabecular microstructure as assessed by ITS analysis and the simplified PR μFE model. Plate and rod bone volume fraction (pBV/TV and rBV/TV) were maintained in the PR μFE models. The number of trabeculae in ITS and the number of elements in the PR model suggested that each trabecular plate was modeled by 6 shell elements, on average, and each trabecular rod was modeled by 1.06 beam elements. It should also be noted

that one of the benefits of the PR μFE models is a drastic reduction in model size and computation time. Overall, conversion from voxel model to PR model resulted in 83-fold reduction in model size and 324-fold reduction in nonlinear FEA computation time (Table 2.3). If taking account the model generation time, PR model-based FEA led to 215-fold reduction in total computation time compared with voxel model.

BV/TV is also highly correlated with the experimental measurements of elastic modulus and yield strength in these on-axis specimens. However, whereas BV/TV predicted anisotropic mechanical properties of human trabecular bone poorly, the PR μFE models accurately predicted the anisotropic mechanical properties of trabecular bone. As shown in Figure. 2.7 and 2.8, BV/TV was highly correlated with the on-axis E_z and σ_z (R^2=0.98, 0.98), but only moderately correlated with off-axis E_x, E_y, σ_x and σ_y (R^2=0.65~0.77). Yet, the PR μFE models were able to predict both elastic modulus and yield strength along all directions, x, y and z-axes, respectively, in comparisons to voxel models (R^2=0.96~0.99).

It was observed that similar accuracy of PR model predictions for a separate and independent set of distal tibia and distal radius trabecular bone specimens (Figure. 2.9). PR model predictions of elastic modulus and yield strength highly correlated with voxel model predictions (R^2=0.98, 0.97), with a relative error of 0.08 (-0.07~0.20) and -0.22 (-0.40~0.01), respectively.

2.4. Discussion

Human trabecular bone consists mainly of a collection of trabecular plates and rods connected to form an anisotropic network. It has been demonstrated that there is an apparent transition from plate-like to rod-like microstructure in osteoporotic trabecular bone by either the Structure Model Index (SMI) or more advanced ITS based measures (Ding and Hvid 2000, Cohen,

Liu et al. 2009, Liu, Cohen et al. 2010). From both computational and experimental studies, it has been shown that trabecular plates play a more dominant role in mechanical integrity of human trabecular bone (Wang, Zhou et al. 2013, Stein, Kepley et al. 2014, Zhou, Liu et al. 2014). It is not clear how adequate is the plate-rod assumption of trabecular bone microstructure in quantifying mechanical properties of human trabecular bone. In this study, μFE models were constructed based explicitly on the ITS plate and rod segmentations and tested their ability in predicting elastic modulus and yield strength measured experimentally and computed by voxel based μFE models.

The reconstructed PR μFE models based on ITS preserve the 3D trabecular bone microstructure, including trabecular types and their bone tissue volume, trabecular orientation, and trabecular connectivity. The results indicate that these reconstructed PR μFE models predict accurately the elastic modulus and yield strength determined by the gold standard mechanical testing and voxel based μFE models. Furthermore, these PR μFE models also adequately describe the anisotropic elastic and yield properties of human trabecular bone. Therefore, our results suggest that trabecular plates and rods adequately determine elastic modulus and yield strength of human trabecular bone. In addition, these PR μFE models provided 83-fold reduction in model size and 324-fold reduction in nonlinear FEA computational time to determine yield strength of trabecular bone. In Vanderoost et al., they achieved a 7-fold reduction in the number of elements, and a 33-fold reduction in the central processing unit (CPU) time in linear analyses for estimating elastic modulus (Vanderoost, Jaecques et al. 2011). One of their pilot nonlinear analyses indicated a 45-fold reduction in CPU time. However, both models of Vanderoost and our early work significantly underestimated apparent elastic modulus and strength in comparison to those by voxel models or experiments. The refined PR modeling strategy proposed in this study

demonstrated accurate prediction of both elastic modulus and yield strength by nonlinear FE analysis, and achieved more significant reduction in model size and computational time.

There are several limitations of this study. Uniform and isotropic material properties were used for trabecular bone tissue, which are certainly inhomogeneous and anisotropic. Although, it is interesting that PR μFE models using this single constant material property of trabecular bone tissue predicted well the on-axis mechanical properties of human trabecular bone from several anatomic sites, it remains to be seen how inhomogeneous and anisotropic trabecular bone tissue properties affect apparent, anisotropic properties of human trabecular bone. Second, it was assumed symmetric tissue-level strengths under compression and tension in predicting the yield strength of trabecular bone. Using the same material property, PR μFE models predicted yield strengths that did not differ from experimental measurements, whereas voxel μFE models overestimated yield strengths as measured in experiments. It was shown that voxel μFE models with tissue strength asymmetry taken into account could accurately predict yield strengths measured experimentally (Bevill, Eswaran et al. 2006). It remains to be tested whether tissue strength asymmetry would influence yield strength prediction by the PR μFE models. Furthermore, both the voxel and the PR μFE models used the elasto-plastic material law, which has a significant limitation in post-yield behaviors of bone such as unloading. Although, this limitation will not affect the conclusions of the current study regarding elastic modulus and yield strength of human trabecular bone, a better constitutive law for bone tissue, in general, for both voxel and PR μFE models is needed for post-yield behaviors such as unloading or ultimate strength.

The feasibility of our PR μFE modeling approach has been quantified in idealized plate and rod microstructural models, which were made of either a combination of two plates and four rods or purely eight interconnected rods in a unit cell (Wang, Liu et al. 2013). Excellent agreement

was found between the mechanical properties calculated from PR models and the corresponding voxel models, such as elastic modulus and yield strength. This idealized study provided fundamental assessment of PR μFE models in predicting mechanical properties of trabecular bone, independent of biological variations among human bone specimens and image noises existing in the imaging process. PR μFE models have also been applied on clinical HRpQCT images and demonstrated the ability of HRpQCT-based μFE PR models to predict bone strength and discriminate postmenopausal women with and without vertebral fractures (Liu, Wang et al. 2013). Elastic modulus and yield strength predicted by HRpQCT-based PR models were strongly correlated with those by voxel models. Furthermore, HRpQCT-based PR model revealed marked mechanical deficiency in postmenopausal women with vertebral fracture compared with nonfracture controls. Therefore, the ITS based PR μFE models also provide a highly efficient and alternative approach for clinical prediction of mechanical integrity in patients.

In summary, I used ITS based trabecular plate and rod segmentation to create PR μFE models, which maintain only plate-rod microstructure of human trabecular bone. By comparing the prediction in elastic modulus and yield strength to those determined by experiments and voxel based computations, I concluded that trabecular plate and rod microstructure sufficiently determine mechanical properties of human trabecular bone. The study also provides the validation of the PR μFE approach in quantifying mechanical properties of trabecular bone in both basic science and clinical studies.

Table 2.1. Elastic modulus and yield strength measured by mechanical testing experiment and predicted by FE analysis using voxel model and PR model. Data is shown as Mean ± SD.

	Elastic modulus (MPa)			Yield strength (MPa)		
	PR model	Experiment	Voxel model	PR model	Experiment	Voxel model
PT	757 ± 383	785 ± 407[c]	739 ± 387[c]	3.98 ± 2.11[b]	4.09 ± 2.32[c]	5.12 ± 2.72[b,c]
FN	3,239 ± 1,518	3,132 ± 1,466	3,155 ± 1,447	18.68 ± 8.83[b]	18.72 ± 8.88[c]	23.50 ± 11.61[b,c]
GT	491 ± 329	498 ± 349	489 ± 339	2.66 ± 1.82[b]	2.44 ± 1.65[c]	3.29 ± 2.33[b,c]
Pooled	1,452 ± 1,515	1,430 ± 1,457	1,419 ± 1,466	8.25 ± 8.91[b]	8.16 ± 8.92[c]	10.08 ± 11.14[b,c]

[a] PR model predictions different from experimental measurements; [b] PR model predictions different from voxel model predictions; [c] voxel model predictions different from experimental measurements, $p<0.05$.

Table 2.2. ITS evaluation of the original trabecular microstructure and assessment of the recreated microstructure in the PR model. Data is shown as Mean ± SD.

	PT (n=22)	FN (n=20)	GT (n=20)	Pooled (n=62)
ITS parameters				
BV/TV	0.106 ± 0.031	0.293 ± 0.104	0.111 ± 0.070	0.162 ± 0.110
pBV/TV	0.094 ± 0.031	0.281 ± 0.101	0.083 ± 0.036	0.149 ± 0.110
rBV/TV	0.014 ± 0.004	0.012 ± 0.004	0.013± 0.004	0.013 ± 0.004
Number of plates	4,163 ± 1,060	8,033 ± 2,524	4,028 ± 1,744	5,237 ± 2,548
Number of rods	1,751 ± 439	2,056 ± 808	1,719 ± 670	1,828 ± 655
PR model parameters				
BV/TV	0.106 ± 0.031	0.293 ± 0.104	0.111 ± 0.070	0.162 ± 0.110
pBV/TV	0.094 ± 0.031	0.281 ± 0.101	0.083 ± 0.036	0.149 ± 0.110
rBV/TV	0.014 ± 0.004	0.012 ± 0.004	0.013± 0.004	0.013 ± 0.004
Number of shell elements	23,973 ± 6,553	48,951 ± 16,117	22,836 ± 10,460	30,803 ± 16,220
Number of beam elements	1,868 ± 461	2,163 ± 842	1,820 ± 714	1,936 ± 688

Table 2.3. Comparison of model size, FEA computation time and model generation time between PR model and voxel model. Data is shown as Mean ± SD.

	PT		FN		GT		Pooled	
	Voxel model	PR model	Voxel model	PR model	Voxel model	PR model	Voxel model	PR model
# Element	1,822,600 ± 509,703	26,219 ± 6,704	3,257,231 ± 1,777,522	51,114 ± 16,888	3,182,186 ± 2,440,628	22,975 ± 8,647	2,728,837 ± 1,847,899	32,999 ± 16,788
CPU Time for nonlinear FEA (Minutes)	2,546.99 ± 622.60	11.39 ± 10.10	4,990.58 ± 4,290.19	16.11 ± 18.57	3,825.85 ± 2,374.51	7.46 ± 4.64	3,744.94 ± 2,923.14	11.57 ± 12.59
Model Generation Time (Minutes)	0.5 ± 0.2	5.29 ± 1.11	1.0 ± 0.6	6.35 ± 1.29	0.4 ± 0.15	6.00 ± 1.29	0.6 ± 0.3	5.87 ± 1.29

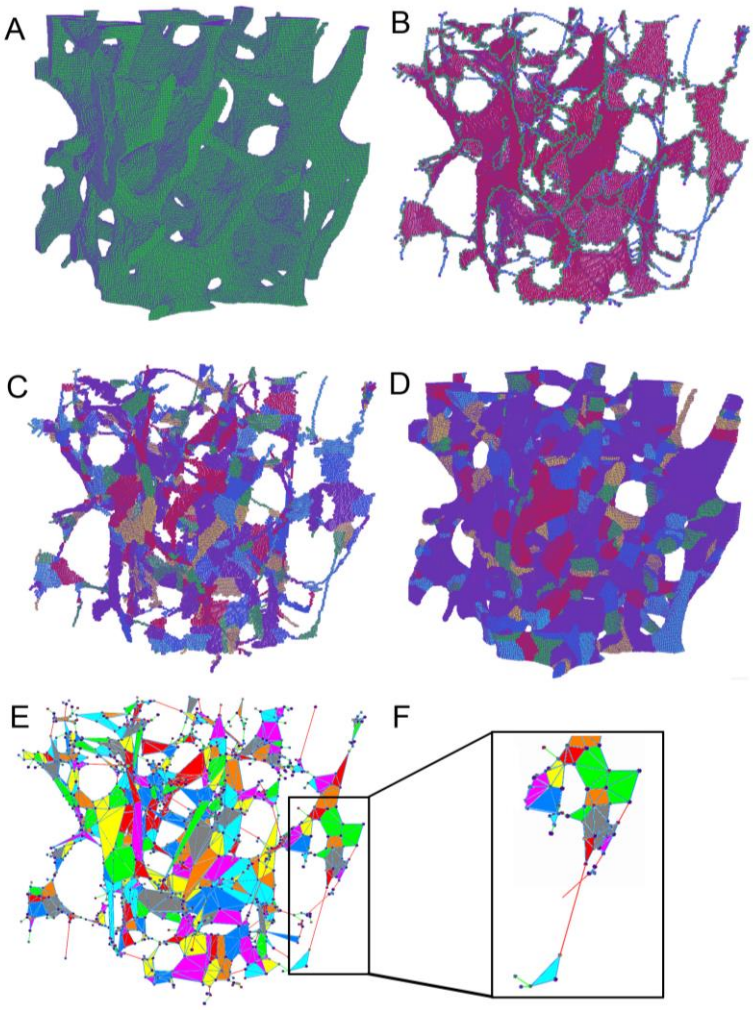

Figure 2.1. Illustration of ITS-based PR modeling on a cubical trabecular bone specimen. (A) Original 3D volume of the trabecular bone. (B) Microstructural skeleton with the trabecular type labeled for each voxel. Plate skeleton voxels are shown in red, surface edge voxels in green, rod skeleton voxels in blue. (C) Segmented microstructural skeleton with individual trabeculae labeled by color for each skeleton voxel. (D) Recovered trabecular bone with individual trabeculae labeled by color for each voxel. (E) PR model with shell and beam elements and color indicating different trabeculae. (F) Details of the beam-shell connection, note that the thickness of shell and beam elements was not depicted.

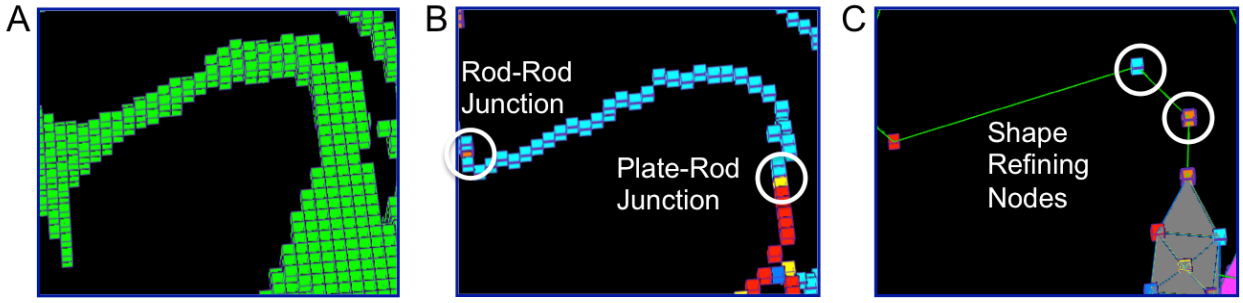

Figure 2.2. Meshing trabecular rods into beam elements. (A) Original microstructure of a trabecular rod; (B) Rod-rod junction or plate-rod junction at both ends of the trabecular rod skeleton; (C) Shape refining nodes divide the rod into three beam elements.

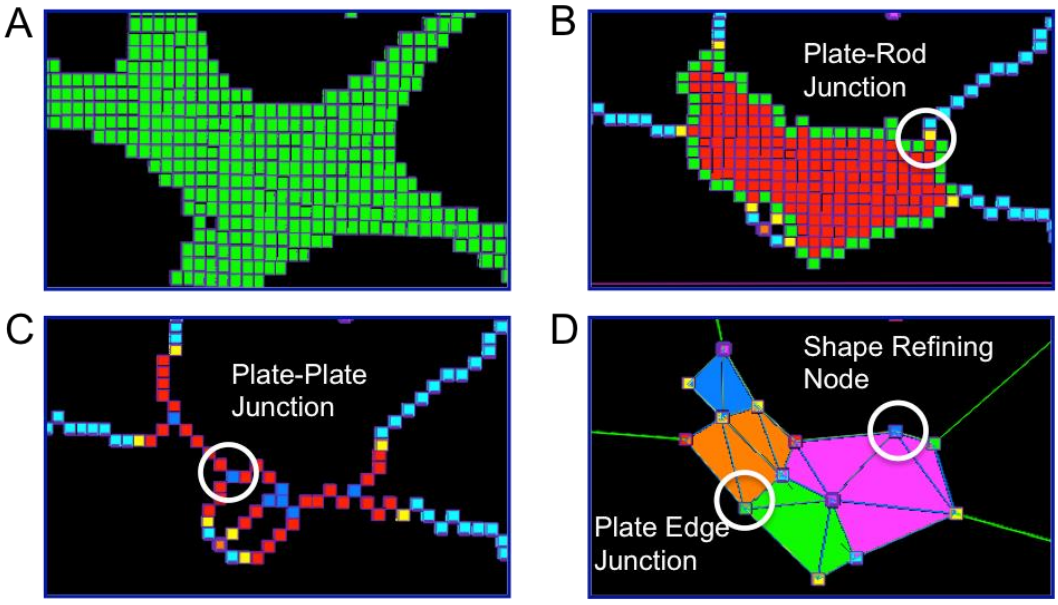

Figure 2.3. Meshing trabecular plates into shell elements. (A) Original microstructure of the trabecular plate; (B) Plate-rod junctions connecting plate and rod skeletons; (C) Plate-plate junctions connecting plate-arc skeletons; (D) Plate edge junctions and shape refining nodes are added to construct triangular shell elements.

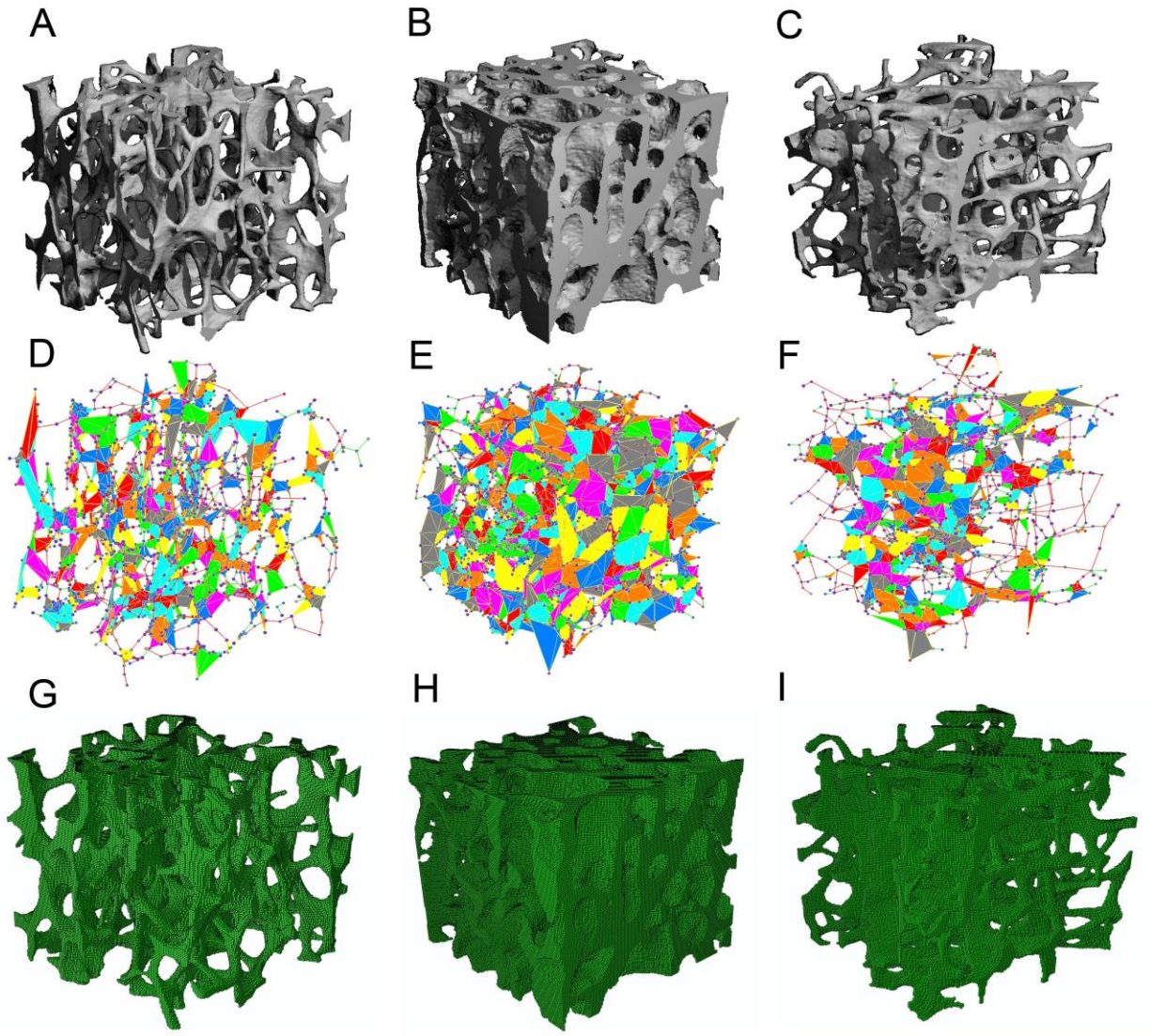

Figure 2.4. µCT image of human trabecular bone from (A) PT, (B) FN, and (C) GT; PR models for (D) PT, (E) FN, and (F) GT; corresponding voxel models for (G) PT, (H) FN, and (I) GT.

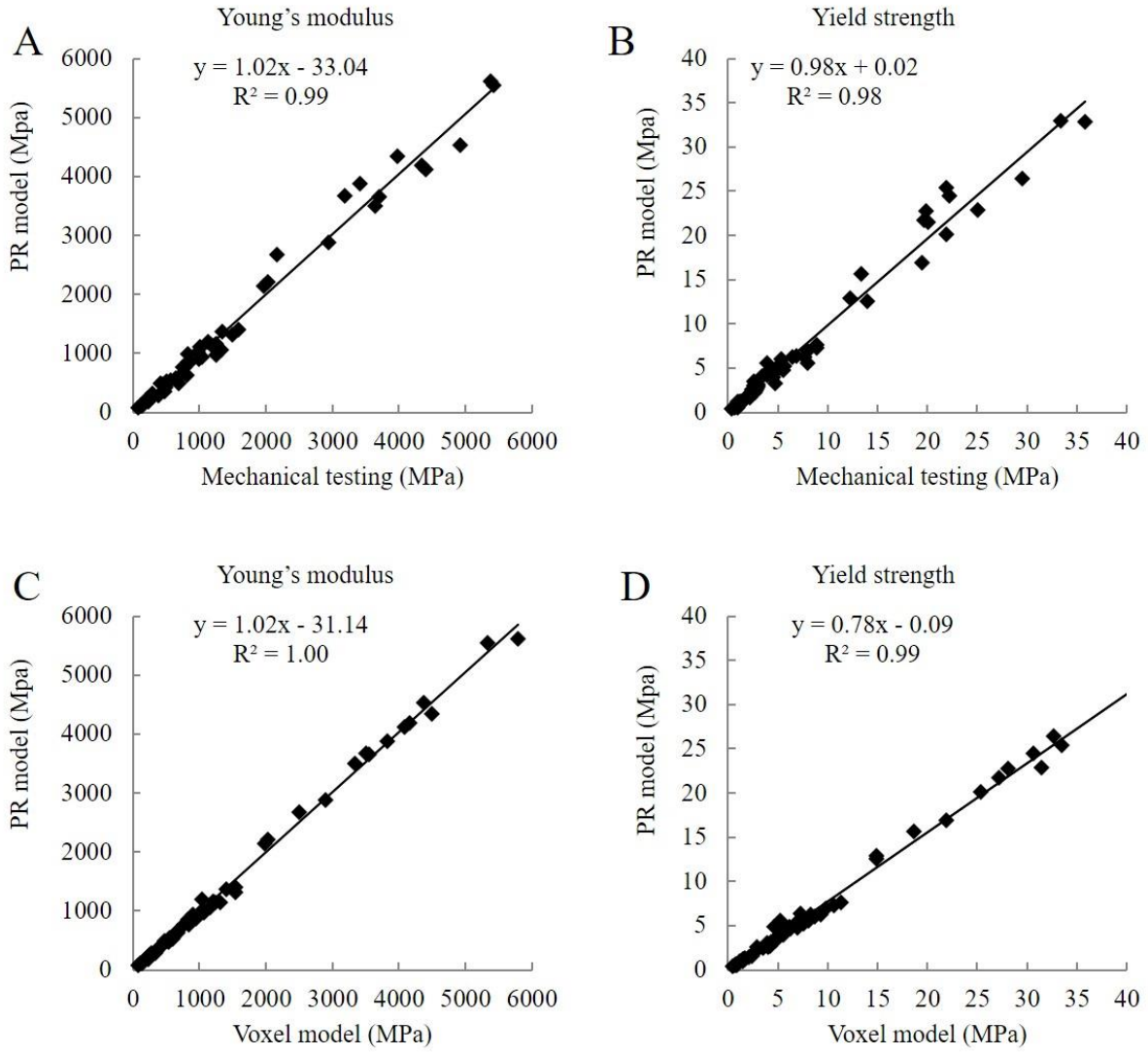

Figure 2.5. Linear regressions of the elastic modulus (A, C) and yield strength (B, D) between PR model prediction and voxel model prediction and experimental measurements (data pooled from three sites).

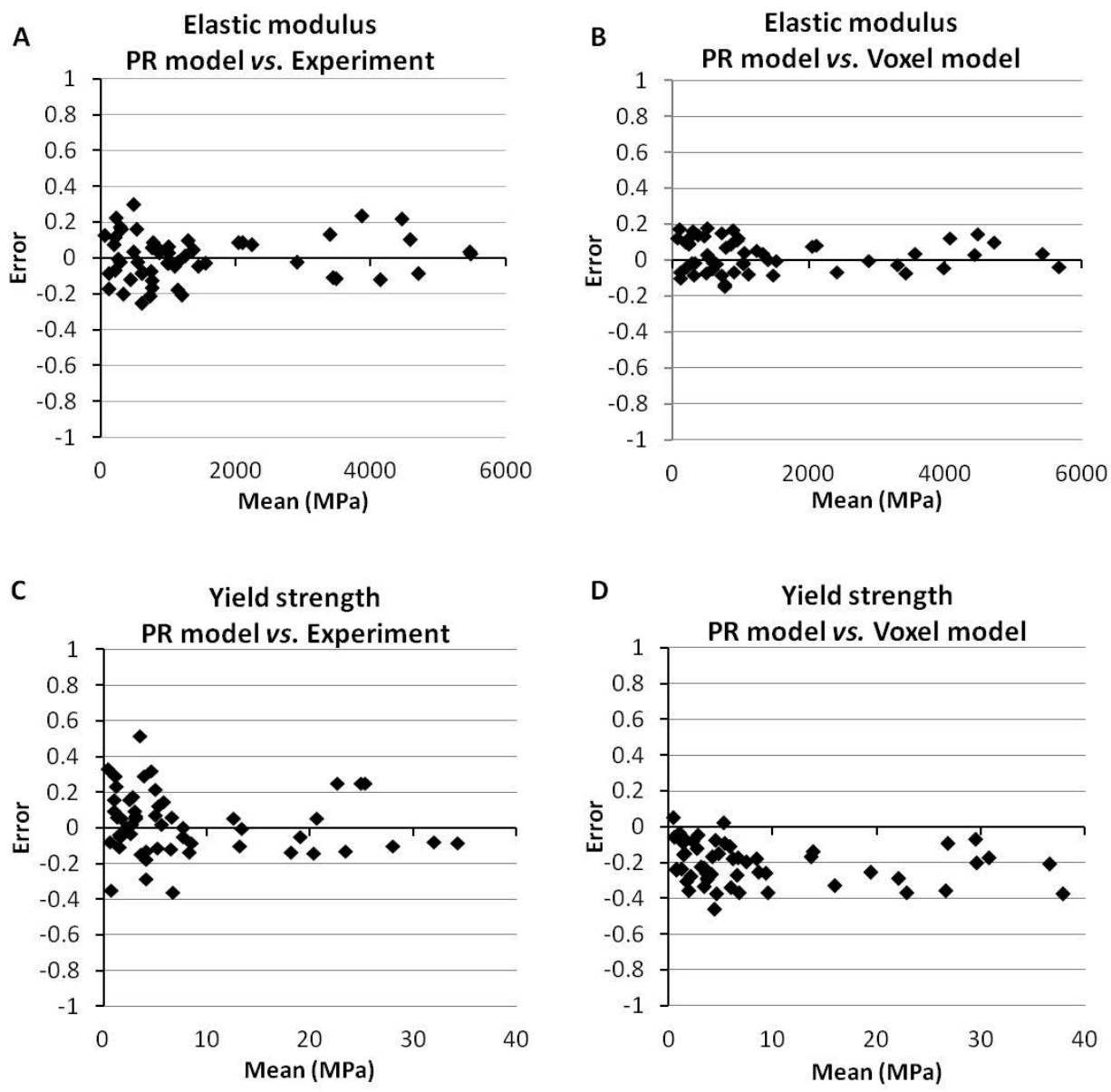

Figure 2.6. Bland-Altman plots of the prediction error of PR model compared to voxel model and mechanical testing experiment. Error = (PR model - voxel model or experiment) / mean.

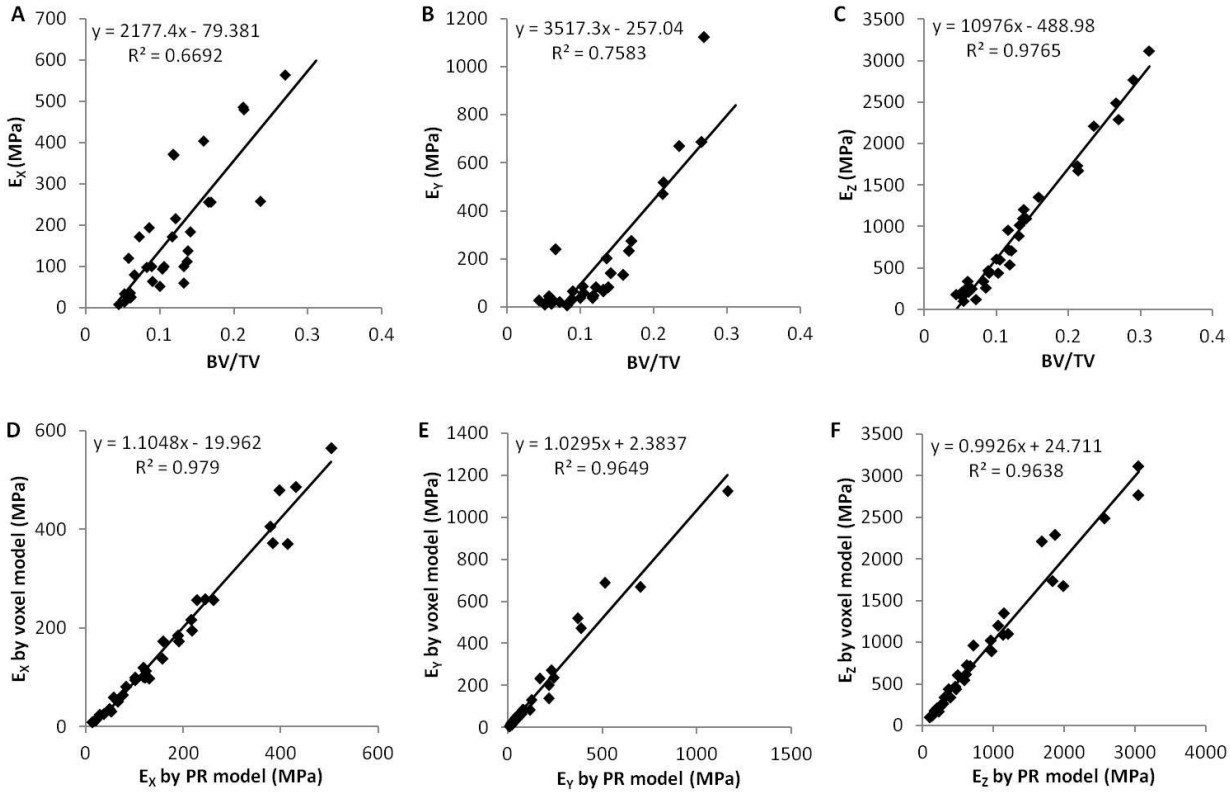

Figure 2.7. (A~C) Linear regressions between bone volume fraction and the elastic modulus along x, y and z axes determined by voxel models; (D~F) linear regressions between the elastic modulus along x, y and z axes predicted by PR models and voxel models.

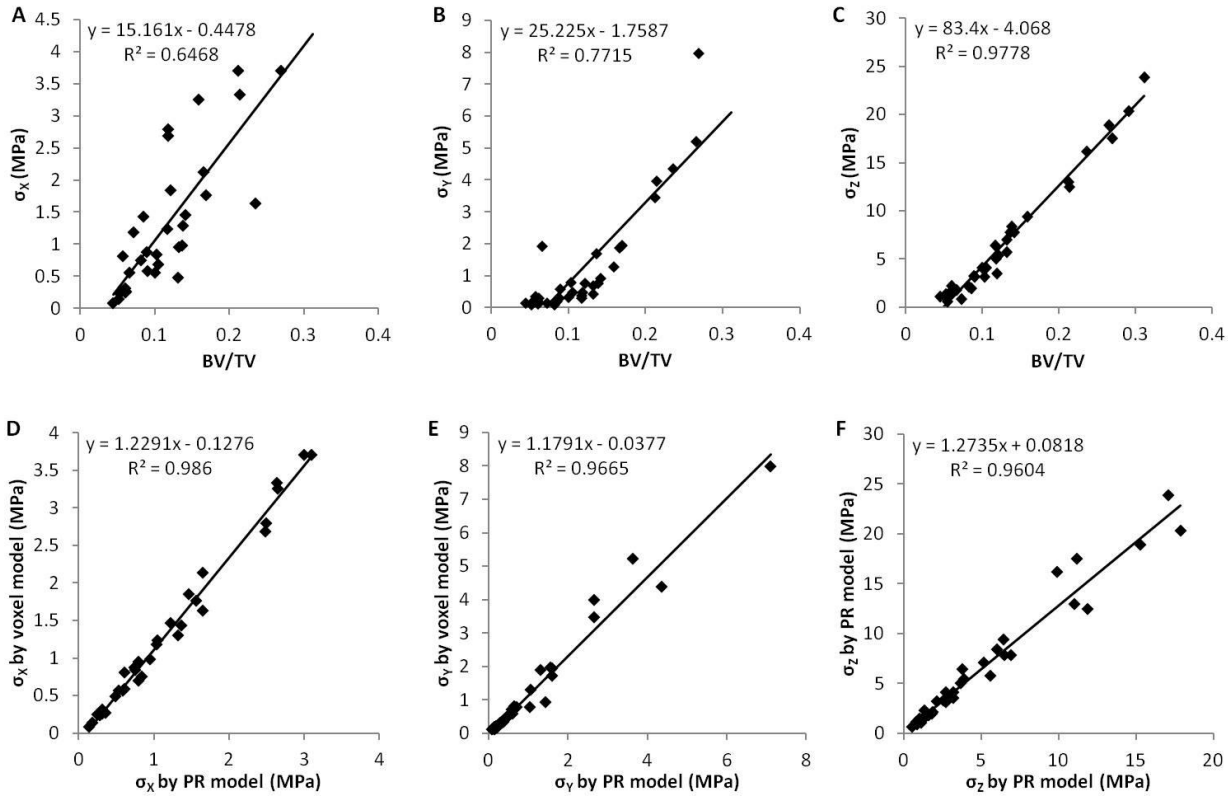

Figure 2.8. (A~C) Linear regressions between bone volume fraction and the yield strength along x, y and z axes determined by voxel models; (D~F) linear regressions between the yield strength along x, y and z axes predicted by PR models and voxel models

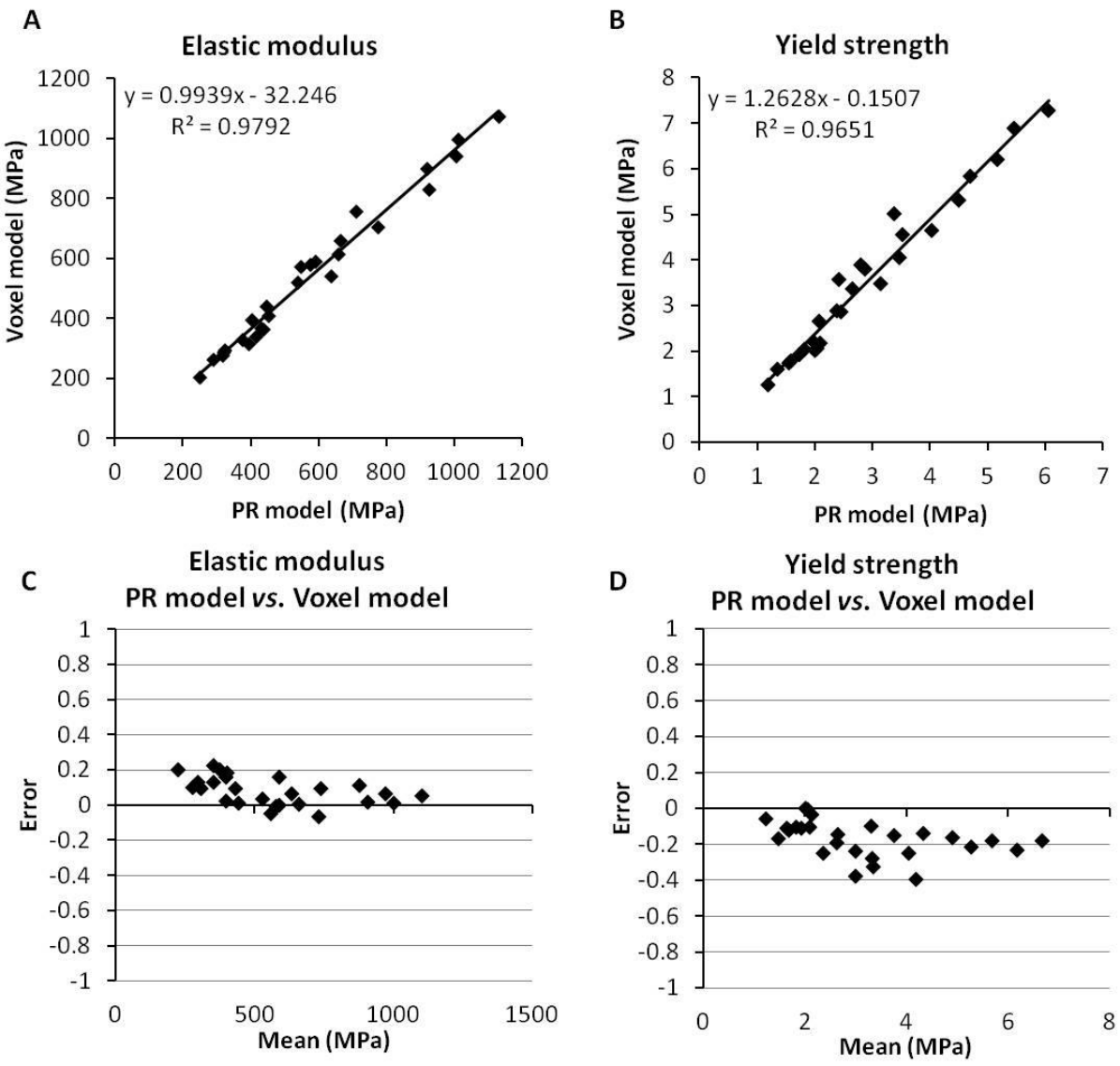

Figure 2.9. Comparison between PR model and voxel model for the test set of trabecular bone specimens at distal tibia and distal radius.

Chapter 3. Distinct tissue mineral density in plate and rod-like trabeculae

3.1. Introduction

Tissue mineral density (TMD) and its heterogeneous distribution are key determinants of the intrinsic mechanical properties of trabecular bone tissue (Rho, Zioupos et al. 1999, Jaasma, Bayraktar et al. 2002). The nonuniform TMD in trabecular bone tissue results from frequent bone remodeling and dynamic mineralization kinetics in newly formed bone packets. Normal healthy adults have a characteristic TMD distribution regardless of gender, age and race. Many bone metabolic diseases, e.g., osteoporosis and osteomalacia, are associated with distinct deviations from the reference TMD distribution of healthy individuals (Roschger, Gupta et al. 2003, Roschger, Paschalis et al. 2008). Additionally, patients with fragility fractures at the hip and spine have more heterogeneous bone mineralization than the nonfracture control subjects (Ciarelli, Fyhrie et al. 2003, Loveridge, Power et al. 2004, Seitz, Koehne et al. 2013). These findings suggest basic science and diagnostic value for evaluating the distribution of TMD; however, knowledge is lacking regarding factors that contribute to the heterogeneity of TMD. For instance, bone mineralization has not yet been investigated on the individual trabecular level. In addition, it is unclear how individual trabecular TMD varies with trabecular types and orientations.

Trabecular bone microstructure is an important determinant for bone strength and fragility that is independent of areal bone mineral density measurement by dual-energy X-ray absorptiometry (DXA) (Sornay-Rendu, Boutroy et al. 2007, Liu, Stein et al. 2012). Individual trabecula segmentation (ITS)-based morphological analysis, which segments trabecular microstructure into individual trabecular plates and rods, has demonstrated that trabecular plates

and rods of different orientations have varying impact on the mechanical properties and failure mechanisms of trabecular bone (Liu, Sajda et al. 2006, Liu, Sajda et al. 2008, Liu, Walker et al. 2011, Liu, Wang et al. 2013, Wang, Zhou et al. 2015). Based on microstructural differences between trabecular plates and rods, it was hypothesized that plate-like and rod-like trabeculae also differ in TMD, and trabeculae of different orientations have different TMD.

The material property of bone tissue is usually assumed to be homogeneous in FE simulations. For instance, in the PR model introduced in Chapter 2, bone tissue was assumed to have a homogeneous tissue modulus of 15 GPa. It is unclear whether incorporating mineral heterogeneity into the PR models will have an impact on the prediction of apparent mechanical properties of trabecular bone. The grayscale value of a μCT voxel represent the mineral density of the corresponding volume of bone tissue, and trabecular microstructure can be further segmented into individual trabecular plates and rods by ITS. By combining high-resolution three-dimensional (3D) micro computed tomography (μCT) imaging and ITS analysis, I developed a new volumetric mineralization analysis technique, individual trabecula mineralization (ITM), which provides detailed and direct measurements of TMD of individual trabecular plates and rods. The TMD of each trabecular plate and rod were further converted to tissue modulus according to a linear relationship between them established by microindentation experiment. Considering the beam hardening effect introduced by polychromatic x-ray source in the μCT system, the ITM technique using μCT was first compared to that based on synchrotron radiation μCT (SRμCT), the gold standard for 3D TMD evaluation without any beam hardening. Then, I used the newly developed ITM technique to (1) quantify the TMD of individual trabeculae in human trabecular bone; (2) compare the TMD distributions of plate- and rod-like trabeculae; (3) establish the relationship

between TMD and trabecular orientation; (4) evaluate the influence of TMD variation on apparent mechanical properties of trabecular bone.

3.2. Materials and Methods

3.2.1. Validation Set

In order to verify the ITM measurements, trabecular bone samples were prepared at the University of California at San Francisco and imaged by both SRμCT and μCT as described in Kazakia et al.. Trabecular bone cores (8 mm diameter, 4 mm length) were obtained from the femoral head (n=5), vertebral body (n=5), and proximal tibia (n=4). SRμCT imaging was performed on a beamline X2B of the National Synchrotron Light Source (Brookhaven National Laboratory, Upton, NY). 3D SRμCT images of trabecular bone samples were reconstructed at an isotropic voxel size of 7.50 μm. μCT imaging was performed on a μCT 40 (Scanco Medical AG, Switzerland) combined with two beam hardening correction (BHC) factors derived from the polynomial attenuation profiles of two wedge phantoms composed of a hydroxyapatite (HA)-resin mixture of 200 mg HA/cm^3 and 1200 mg HA/cm^3, respectively. μCT images were reconstructed at an isotropic voxel size of 8 μm. A Gaussian filter along with site- and modality-specific threshold values were applied. A HA rod density calibration phantom was scanned under the same conditions as the trabecular bone samples to convert attenuation levels to HA concentrations for the SRμCT data, μCT data with 200 mg HA/cm^3 BHC, and μCT data with 1200 mg HA/cm^3 BHC. Kazakia et al.(Kazakia, Burghardt et al. 2008) has reported this data set and compared TMD measurements of the SRμCT and μCT images.

3.2.2. Experimental Set

Sixty-three cylindrical (8mm diameter, 20 mm length) human trabecular bone samples were obtained from the proximal tibia (PT, n=22), greater trochanter (GT, n=21), and femoral neck

(FN, n=20) at Columbia University (Table 3.1). The subjects (n=26, 19 male and 7 female, 69±12 years) were screened to exclude history of metabolic bone diseases or bone cancers. X-ray radiographs were taken to ensure no evidence of damage, fracture, or other bone pathologies. Trabecular bone cores were drilled along the principle loading direction following a previously reported protocol (Morgan and Keaveny 2001). To ensure that the longitudinal axis of the bone core was aligned along the primary trabecular orientation, X-ray radiographs were taken on two orthogonal planes parallel with the longitudinal axis. Any sample with an angle between the trabecular orientation and the longitudinal axis larger than 10° was excluded from this study. Samples were wrapped with wet gauze in airtight plastic bags and stored at -20°C when not being processed. Images of the central gauge length of 8 mm were obtained by μCT (VivaCT 40, Scanco Medical AG, Switzerland) at an isotropic voxel size of 15 μm with a source potential of 55 kV and tube current of 109μA. To minimize the beam hardening effect, a standard aluminum filter was installed in the μCT scanner, and a voltage- and scanner- specific BHC algorithm derived from a wedge phantom of 200 mg HA/cm^3 density was implemented (Burghardt, Kazakia et al. 2008). Gaussian filter and anatomic site-specific threshold values were applied to segment grayscale images into binary images composed of bone and marrow. The bone morphology and mechanics data of these specimens have been reported (Zhou, Liu et al. 2014, Wang, Zhou et al. 2015). Furthermore, the original grayscale value of each voxel, representing the attenuation coefficient, was converted to HA concentration using a linear regression derived by imaging a calibration phantom containing rods of HA-resin mixtures (0, 100, 200, 400, and 800 mg HA/cm^3). Given that the peripheral regions of the trabecular bone cores were likely to be affected by cupping artifact, the central 5×5×5 mm^3 cubic sub-volume of each image was extracted for subsequent ITM analysis.

3.2.3. Individual Trabecula Mineralization (ITM) Analysis

Grayscale images containing volumetric bone mineral densities (in mg HA/cm^3) and binary images representing trabecular microstructure were both imported into ITM analysis (Figure. 3.1). By ITS, trabecular bone microstructure was decomposed into individual trabecular plates and rods (Saha and Chaudhuri 1996, Saha, Chaudhuri et al. 1997, Liu, Sajda et al. 2008). Briefly, through an iterative thinning process, a surface and curve skeleton of the trabecular bone microstructure was extracted with its topology and morphology fully preserved (Saha, Chaudhuri et al. 1997). Then, the entire skeleton was decomposed into individual trabecular skeletons with each voxel uniquely classified as either a plate or a rod type based on digital topological classification (Saha and Chaudhuri 1996). The segmented skeleton was then returned to the original volume as a collection of individual trabecular plates and rods labeled with unique identification numbers. To quantify TMD of each individual trabecula, the segmented trabecular plate and rod microstructure was mapped to the original grayscale image. On the single voxel level, the volumetric mineral density was determined from the grayscale value by the linear regression derived from the HA calibration phantom scan, and the microstructural type was classified as either trabecular plate or rod. Individual trabecula TMD was defined as the average TMD of all the voxels that belonged to this trabecula. Additionally, the orientation of individual trabecular plates or rods was determined with reference to the principal trabecular direction of the bone sample. For a trabecular plate, angle Φ was defined as the angle between the normal vector of the plate and the longitudinal axis. For a trabecular rod, angle Φ was defined as the angle between the direction of the rod and the longitudinal axis. Trabecular orientations were categorized into longitudinal (angle Φ 60°~90° for plates and 0°~ 30° for rods), oblique (angle Φ 30°~60° for plates and rods), and transverse (angle Φ 0°~ 30° for plates and 60°~90° for rods).

3.2.4. TMD Distributions in Trabecular Plates and Rods

A histogram of TMD distribution in individual trabecular plates and rods was plotted. The following parameters were defined to characterize a TMD distribution: the average TMD of plate- and rod-like trabeculae ($pTMD_{MEAN}$, $rTMD_{MEAN}$), the most frequent TMD of trabecular plates and rods ($pTMD_{PEAK}$, $rTMD_{PEAK}$), the width of distributions in trabecular plates and rods at half maximum frequency ($pTMD_{WIDTH}$, $rTMD_{WIDTH}$), the percentage of trabecular plates and rods whose TMD was lower than the 5^{th} percentile of the overall distribution ($pTMD_{LOW}$, $rTMD_{LOW}$), and the percentage of trabecular plates and rods which were mineralized above the 95^{th} percentile of the overall distribution ($pTMD_{HIGH}$, $rTMD_{HIGH}$). The low and high mineralization cutoff values were determined based on the pooled TMD distribution at each of the anatomic sites in the validation set and experimental set.

3.2.5. Heterogeneous PR μFE model

Three PR μFE models were generated for each specimen using different bone tissue properties: (1) a homogeneous model with a constant tissue modulus determined by the average TMD of the specimens; (2) a specimen-specific model with tissue modulus determined by the average TMD of each specimen; (3) a heterogeneous model in which each shell and beam element were assigned the tissue modulus determined by the TMD of the corresponding trabecular plate or rod. Trabecular bone tissue was modeled as an isotropic, linear elastic material with a Poisson's ratio of 0.3(Bayraktar, Morgan et al. 2004). μFE analysis simulating a uniaxial compression test along the longitudinal direction of the trabecular bone specimen was performed, and apparent Young's modulus was derived. To determine the influence of TMD variation, I compared the apparent Young's modulus and yield strength predicted by the homogeneous model, specimen-

specific model, and heterogeneous model with reference to the measurements from mechanical testing as described in Chapter 2.2.2.

3.2.6. Statistical Analysis

Statistical analyses were conducted with NCSS (NCSS Statistical Software, Kaysville, Utah). Paired Student's *t* test was applied to compare the TMD distribution parameters of plate- and rod-like trabeculae. Two-sided p value <0.05 was considered to indicate statistically significant. Differences between trabecular plate and rod TMD distributions were further assessed by a Kolmogorov-Smirnov test. Bland-Altman plots were used to show the disparity between the heterogeneous model and the homogeneous, plate-heterogeneous, or rod-heterogeneous model. The relative difference between two methods (difference/average) was plotted versus their average.

3.3. Results

3.3.1. TMD Distributions in the Validation Set

Compared to trabecular plates, trabecular rod TMD had a wider distribution and a bigger tail in the low TMD range (Figure 3.2 A~C). Differences between TMD distributions in trabecular plates and rods were more pronounced in the SRμCT data, while a similar pattern was observed in the μCT data with 200 BHC and 1200 mg HA/cm^3 BHC. Statistically, the two-sample Kolmogorov-Smirnov test suggested that TMD distributions in trabecular plates and rods were distinct from each other, based on comparing the cumulative distribution functions of two data sets. TMD values measured by SRμCT were significantly higher than μCT-based TMD values, as shown in Figure 3.2 D~F. The relatively larger underestimation of TMD by the 200 mg HA/cm^3 beam hardening correction led to further discrepancy between μCT and SRμCT data. Kazakia et al. (Kazakia, Burghardt et al. 2008) reported the regressions between μCT and SRμCT TMD measurements of this exact validation data set. Strong correlations (R^2=0.78~0.99) were found

between TMD values calculated by SRμCT and μCT using two beam hardening correction algorithms. Regressions of individual trabecula TMD measurements in our current study resulted in similar correlations (R^2=0.71~0.95) between SRμCT and μCT data (Figure 3.2 G~I). TMD distribution parameters were derived for each specimen and summarized in Table 3.2. In the SRμCT data, $rTMD_{MEAN}$ and $rTMD_{PEAK}$ were significantly lower than $pTMD_{MEAN}$ and $pTMD_{PEAK}$ by 3% and 2%, respectively. $rTMD_{WIDTH}$ was 30% higher than $pTMD_{WIDTH}$. $rTMD_{LOW}$ was 150% higher than $pTMD_{LOW}$, which was the most striking difference between two TMD distributions. Furthermore, lower $rTMD_{MEAN}$ and higher $rTMD_{LOW}$ were consistent in the three data sets of SRμCT, μCT with 200 and 1200 mg HA/cm^3 BHC.

3.3.2. TMD Distributions in the Experimental Set

As the validation set demonstrated substantial differences between the TMD distributions in trabecular plates and rods, the experimental set from FN, PT and GT was used to establish the characteristic TMD distributions in individual trabecular plates and rods of different orientations (Figure 3.3). Trabecular plate and rod TMD distributions in the experimental set agreed with what was observed in the validation set. More specifically, trabecular rod TMD distribution shifted towards lower TMD relative to trabecular plate TMD distribution with a wider band and a heavier tail in the low TMD range. Distribution indexes showed that $rTMD_{MEAN}$ and $rTMD_{PEAK}$ were lower than $pTMD_{MEAN}$ and $pTMD_{PEAK}$ by 2.3% and 1.4%, respectively. $rTMD_{WIDTH}$ was 8.8% higher than $pTMD_{WIDTH}$, and $rTMD_{LOW}$ was 140.8% higher than $pTMD_{LOW}$. Lower $rTMD_{MEAN}$ and higher $rTMD_{LOW}$ relative to $pTMD_{MEAN}$ and $pTMD_{LOW}$ were found consistently at FN, GT, and PT (Table 3.3). It was observed that trabecular bone at FN had higher TMD and higher BV/TV than PT and GT. No difference in TMD was observed between male and female subjects. Finally,

trabecular plate and rod TMD did not increase with age of the subjects ($p=0.17$); however, this observation could be limited by the number of specimens in this study.

3.3.3. TMD of Individual Trabeculae along Different Orientations

In the experimental set, it was observed that TMD of individual trabecular plates increased from the longitudinal to the transverse direction, namely longitudinal trabecular plates had lower TMD than oblique and transverse plates (Figure 3.4). Such orientation-wise TMD variation in trabecular plates was consistent across all tested anatomic sites. Conversely, trabecular rod TMD was relatively uniform along different trabecular orientations. Trabecular bone at FN had a higher proportion of transverse trabeculae (14%) and a lower proportion of axially aligned trabeculae (65%) compared with GT and PT ($p<0.05$), which had 11% and 8% transverse trabeculae, and 72% and 80% axial trabeculae ($p<0.05$), respectively.

3.3.4. Effect of TMD Variation on Apparent Young's Modulus Prediction

Apparent Young's modulus and yield strength of trabecular bone predicted by the heterogeneous PR models were strongly correlated with those from homogeneous models and specimen-specific PR models with R^2 equal to 0.99 and 1.00 (Figure 3.5). Moreover, linear regressions between the three PR models and the mechanical testing results were shown in Figure 3.6. Heterogeneous models had similar relationship with mechanical testing measurements as the homogeneous and specimen-specific models without significant change in the correlation coefficient (R^2 =0.98~0.99). The estimated value of Young’s modulus and yield strength differed between heterogeneous and homogeneous models, as well as the specimen-specific models, as shown in Table 3.4.

3.4. Discussion

In this study, I developed an ITM technique, which integrated bone mineralization assessment and trabecular microstructure segmentation, to investigate heterogeneity of TMD associated with trabecular microstructural types and orientations. ITM analysis demonstrated that plate-like trabeculae, on average, had higher TMD than rod-like trabeculae across the anatomic sites of FN, GT and PT. Furthermore, trabecular plate TMD varied among different orientations, showing a significant increase of TMD from the longitudinal plates to the transverse ones. In contrast, trabecular rod TMD had lower average TMD with a wider distribution, and showed little variation along different trabecular orientations.

ITM assessment was first tested on SRμCT images, in the absence of beam hardening effect, and then compared to the results from μCT images of the same trabecular bone samples after BHC. Higher average TMD in trabecular plates than rods was observed in both SRμCT and μCT data. In fact, the difference between trabecular plate and rod TMD distributions was more pronounced in the SRμCT data. These observations verified distinct trabecular plate and rod TMD distributions in the absence of beam hardening effect, and provided important reference to estimate the deviation of μCT-based ITM assessment compared to SRμCT-based results.

ITM analysis revealed that trabecular plates had a significantly higher average TMD than trabecular rods, suggesting a lower bone turnover in trabecular plates which might result from lower surface to volume ratio in trabecular plates. The proportion of trabecular rods with low TMD, below the 5^{th} percentile of the overall TMD distribution, was twice to five times as that of trabecular plates. Also, trabecular rod TMD tended to be more heterogeneous, suggested by a wider distribution. Similarly, using qBEI, Busse et al. observed elevated mineral density distribution in plate-like trabeculae compared to rod-like trabeculae in osteoporotic vertebral bone

(Busse, Hahn et al. 2009). Furthermore, in this study, it was observed that TMD in the longitudinal trabecular plates was lower than the transverse ones, however trabecular rod TMD did not vary with trabecular orientation. It is worth noting that specimens in the experimental set were scanned with the transverse plates parallel to the x-ray beam path, so transverse plates were likely more influenced by beam hardening effect and underestimated in TMD assessment. In spite of this, transverse plates were found to be higher mineralized than longitudinal plates across different anatomic sites. Therefore, our finding was unlikely caused by beam hardening artifact. Additionally, I observed such heterogeneity in plate TMD with orientation in the SRμCT validation set of vertebral specimens, which were harvested with the long axis of the bone core aligned with the superior-inferior direction (the other specimens not controlled in orientation). Lower TMD in the longitudinal trabecular plates, which account for the majority of trabecular plate volume and the predominant load-bearing elements in trabecular network (Liu, Sajda et al. 2008, Liu, Cohen et al. 2010, Liu, Walker et al. 2011, Liu, Stein et al. 2012), might suggest relatively more proactive bone remodeling in those load-bearing trabeculae in response to physiological mechanical loading. The relatively lower TMD in trabecular rods, in general, might suggest active and constant remodeling process in trabecular rods, making them more vulnerable for osteoporotic loss. These new observations in trabecular plate and rod ITM distributions suggest interesting interactions that may inform future directions in bone remodeling studies.

Comparison of heterogeneous and homogeneous models demonstrated difference in apparent Young's modulus and yield strength of trabecular bone resulted from incorporating heterogeneous TMD into the PR model μFE analysis. As shown in Table 3.4, the homogeneous models, either using a universal or specimen-specific tissue modulus, tended to overestimate the apparent mechanical properties as compared to the heterogeneous models. Gross et al.(Gross, Pahr

et al. 2012) and other studies in the effort of developing FE models that account for mineral heterogeneity also reported overestimation of trabecular bone elastic properties by homogeneous SRμCT-based FE models as compared with heterogeneous models. Despite the differences in absolute values, the correlations between FE results of the heterogeneous model and the homogeneous and specimen-specific models were so strong that R^2 was 0.99 to 1.00. Moreover, the linear regressions between the heterogeneous model and mechanical testing measurements were almost identical to the linear regressions between the homogeneous and specimen-specific models and mechanical testing. It suggested that incorporating heterogeneous TMD had minor contribution to providing FE predictions more close to direct experimental measurements. It is worth pointing out that the bone specimens in this study were collected from donors without metabolic bone diseases. It will be interesting to study trabecular plate and rod TMD distributions in metabolic bone diseases known to affect TMD, such as chronic kidney disease or diabetes (Nickolas, Leonard et al. 2008, Dede, Tournis et al. 2014), and changes to bone quality in response to anabolic treatments, such as parathyroid hormone or antibody against sclerostin (Nishiyama, Cohen et al. 2014, Ross, Edwards et al. 2014). The heterogeneous PR models can be applied to study the impact of abnormal bone mineralization on the apparent mechanical properties of these diseased bone.

There are certain limitations associated with the present study. First, ITM assessment based on μCT images is inevitably subjected to partial volume effect caused by voxels on the bone surface containing half bone and half marrow. In the case of high-resolution μCT images, e.g., 15 μm voxel size used in this study, the influence introduced by partial volume effect should be minor. Furthermore, I compared ITM results with and without the bone surface voxels removed (data not shown). Except for elevated TMD of all trabeculae, I observed no change in major observations.

As μCT is inherently affiliated with partial volume and beam hardening effects, ITM analysis based on μCT requires a necessary beam hardening correction, high image resolution, special caution with the sample geometry and porosity, as well as large enough sample collection to draw sound conclusions. Our repeated measurements using μCT at 15 μm indicated the high precision of the ITM technique and the influence of voxel size (15 μm compared to 30 μm) seemed to be minor. This study focused on assessment of TMD heterogeneity associated with trabecular type and orientation. Future work combining ITM analysis and bone histomorphometry may provide additional insights into individual trabecula TMD changes in relation to bone remodeling events and help explain the development of trabecular bone anisotropy.

In conclusion, this study provided direct evidence for distinct TMD distributions in plate- and rod-like trabeculae of human trabecular bone. The ITM analysis enabled evaluating the TMD of individual trabeculae for particular research interests and investigating the interaction between tissue mineralization and trabecular microstructure. By categorizing trabeculae by trabecular type and orientation, this study demonstrated higher TMD in trabecular plates relative to rods, and higher TMD in trabecular plates along the transverse direction relative to the longitudinal direction. Since both trabecular microstructure and tissue property are important indicators for bone quality, the ITM approach will be a valuable tool to improve our understanding of bone fragility from an integrated perspective.

Table 3.1. Donor and sample information in the experimental set

Anatomic site	*No. Specimens*	*No. Donors (male/female)*	*Age (year)*	*BV/TV*
Proximal tibia	22	12 (11/1)	65±7	0.094±0.03
Femoral neck	20	13 (7/6)	72±15	0.28±0.10
Greater Trochanter	21	12 (8/4)	73±13	0.086±0.031

Table 3.2. TMD distribution parameters of trabecular plates and rods in the validation set (n=5, femoral head; n=5, vertebral body; n=4 proximal tibia)

TMD distribution parameters	*Plate (Mean±SD)*	*Rod (Mean±SD)*	*p*
*SR*µCT			
TMD_{MEAN} (mg HA/cm^3)	1006.90 ± 47.70	977.80 ± 54.01	**<0.001**
TMD_{PEAK} (mg HA/cm^3)	1033.72 ± 47.81	1012.71 ± 62.08	**0.007**
TMD_{WIDTH} (mg HA/cm^3)	95.68 ± 17.17	124.85 ± 38.97	**0.003**
TMD_{LOW} (%)	5.57 ± 4.95	14.06 ± 9.50	**<0.001**
TMD_{HIGH} (%)	3.09 ± 5.14	3.43 ± 5.55	0.15
µCT BHC 1200			
TMD_{MEAN} (mg HA/cm^3)	895.69 ± 28.67	885.43 ± 35.55	**0.006**
TMD_{PEAK} (mg HA/cm^3)	899.11 ± 32.57	895.12 ± 39.98	0.43
TMD_{WIDTH} (mg HA/cm^3)	102.05 ± 12.88	107.00 ± 24.70	0.44
TMD_{LOW} (%)	5.54 ± 4.76	12.66 ± 11.59	**0.005**
TMD_{HIGH} (%)	4.62 ± 4.59	5.34 ± 5.22	**0.03**
µCT BHC 200			
TMD_{MEAN} (mg HA/cm^3)	845.22 ± 30.93	834.44 ± 32.01	**0.004**
TMD_{PEAK} (mg HA/cm^3)	849.97 ± 34.58	844.93 ± 35.88	0.55
TMD_{WIDTH} (mg HA/cm^3)	100.73 ± 12.79	115.17 ± 31.53	0.07
TMD_{LOW} (%)	3.81 ± 2.88	8.90 ± 6.56	**0.002**
TMD_{HIGH} (%)	8.47 ± 12.09	8.55 ± 10.16	0.91

Table 3.3 TMD distribution parameters of trabecular plates and rods from PT, FN and GT in the experimental set. (p value of paired Student's t tests for plate- and rod-related parameters)

	Plate	*Rod*	
Variable	*Mean±SD*	*Mean±SD*	*p*
Pooled (n=63)			
TMD_{MEAN} (mg HA/cm^3)	891.66 ± 33.49[a]	871.54 ± 33.47[a]	**<0.001**
TMD_{PEAK} (mg HA/cm^3)	896.32 ± 36.30[a]	884.08 ± 43.56	**0.005**
TMD_{WIDTH} (mg HA/cm^3)	136.00 ± 32.32[c]	148.02 ± 41.97	**0.002**
TMD_{LOW} (%)	4.94 ± 4.86[d]	11.90 ± 8.15	**<0.001**
TMD_{HIGH} (%)	3.13 ± 6.44	2.98 ± 5.10	0.49
PT (n=22)			
TMD_{MEAN} (mg HA/cm^3)	883.77 ± 25.97	867.19 ± 27.76	**<0.001**
TMD_{PEAK} (mg HA/cm^3)	887.86 ± 25.67	882.20 ± 29.17	0.14
TMD_{WIDTH} (mg HA/cm^3)	126.98 ± 15.17	132.00 ± 24.64	0.32
TMD_{LOW} (%)	4.76 ± 4.63	10.93 ± 7.44	**<0.001**
TMD_{HIGH} (%)	1.28 ± 1.03	1.34 ± 1.47	0.75
GT (n=21)			
TMD_{MEAN} (mg HA/cm^3)	875.98 ± 29.26	857.39 ± 27.41	**<0.001**
TMD_{PEAK} (mg HA/cm^3)	878.15 ± 31.02	869.85 ± 37.52	0.38
TMD_{WIDTH} (mg HA/cm^3)	156.91 ± 41.94	158.79 ± 53.28	0.74
TMD_{LOW} (%)	8.40 ± 5.04	16.01 ± 9.07	**<0.001**
TMD_{HIGH} (%)	2.78 ± 3.31	2.49 ± 2.54	0.24
FN (n=20)			
TMD_{MEAN} (mg HA/cm^3)	916.81 ± 31.69	891.17 ± 36.92	**<0.001**
TMD_{PEAK} (mg HA/cm^3)	924.70 ± 35.54	901.08 ± 56.91	**0.007**

TMD_{WIDTH} (mg HA/cm^3)	123.95 ± 23.94	154.36 ± 40.25	**<0.001**
TMD_{LOW} (%)	1.51 ± 1.00	8.64 ± 6.19	**<0.001**
TMD_{HIGH} (%)	5.53 ± 10.61	5.31 ± 8.15	0.72

ANOVA suggested: a, FN different from PT and GT; b, PT different from FN and GT; c, GT different from FN and PT; d, any two sites different from each other

Table 3.4. Predictions of Young's modulus and yield strength by homogenous, specimen-specific, and heterogeneous PR μFE models.

Variable	*Homogeneous model*	*Specimen-specific model*	Heterogeneous model
Pooled (n=63)			
Young's modulus (Mpa)	1386.63 ± 1478.41[a]	1350.11 ± 1499.89[b]	1300.22 ± 1470.52[a, b]
Yield strength (Mpa)	7.80 ± 8.75[a]	7.61 ± 8.87 [b]	8.13 ± 9.34[a, b]
PT (n=22)			
Young's modulus (Mpa)	681.40 ± 366.40[a]	624.79 ± 334.75[b]	596.04 ± 318.47[a, b]
Yield strength (Mpa)	3.54 ± 1.91	3.25 ± 1.75[b]	3.59 ± 1.96[b]
GT (n=21)			
Young's modulus (Mpa)	495.66 ± 355.40[a]	463.79 ± 335.61[b]	424.65 ± 298.27[a, b]
Yield strength (Mpa)	2.58 ± 1.82	2.41 ± 1.72	2.53 ± 1.74
FN (n=20)			
Young's modulus (Mpa)	3199.37 ± 1459.54[a]	3181.11 ± 1514.54[b]	3094.62 ± 1495.06[a, b]
Yield strength (Mpa)	18.58 ± 8.71[a]	18.48 ± 9.01[b]	19.63 ± 9.34[a, b]

a, $p<0.05$ in Student pair t-test between heterogeneous model and homogeneous model; b, $p<0.05$ in Student pair t-test between heterogeneous model and specimen-specific model.

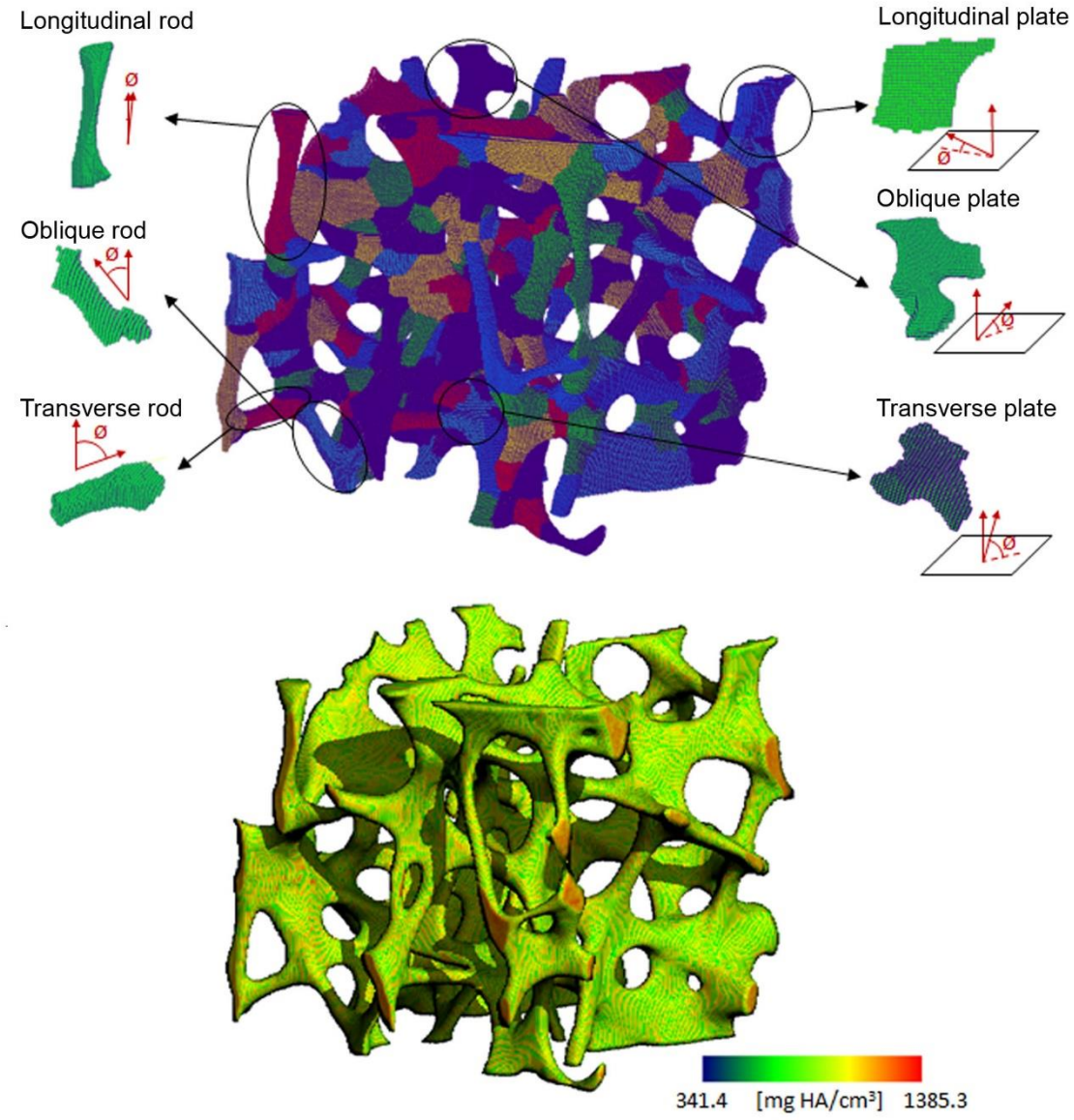

Figure 3.1. Illustration of ITM analysis: (top) decomposition of trabecular microstructure into individual trabecular plates and rods along various orientations; (bottom) grayscale image of trabecular bone to be mapped to the segmented trabecular microstructure to quantify the TMD of individual plates and rods.

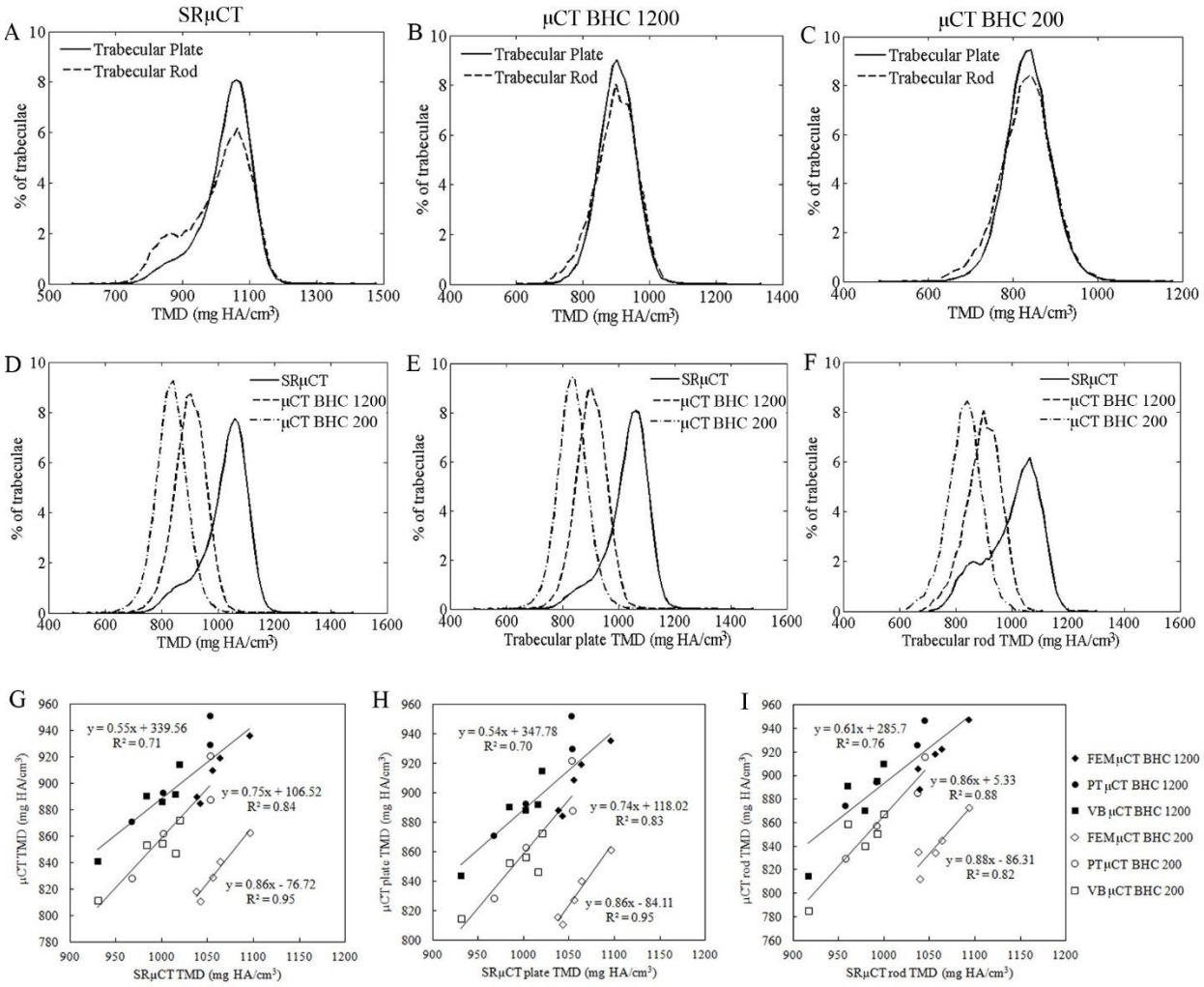

Figure 3.2. (A~C) Measurements of trabecular plate and rod TMD distributions for the validation set by SRμCT, μCT with 1200, and 200 mg HA/cm^3 beam hardening corrections; (D~F) comparisons of TMD, pTMD, and rTMD assessments by SRμCT and μCT with 1200 and 200 mg HA/cm^3 beam hardening corrections; and (G~I) regressions of μCT and SRμCT TMD assessments of all trabeculae, trabecular plates, and rods.

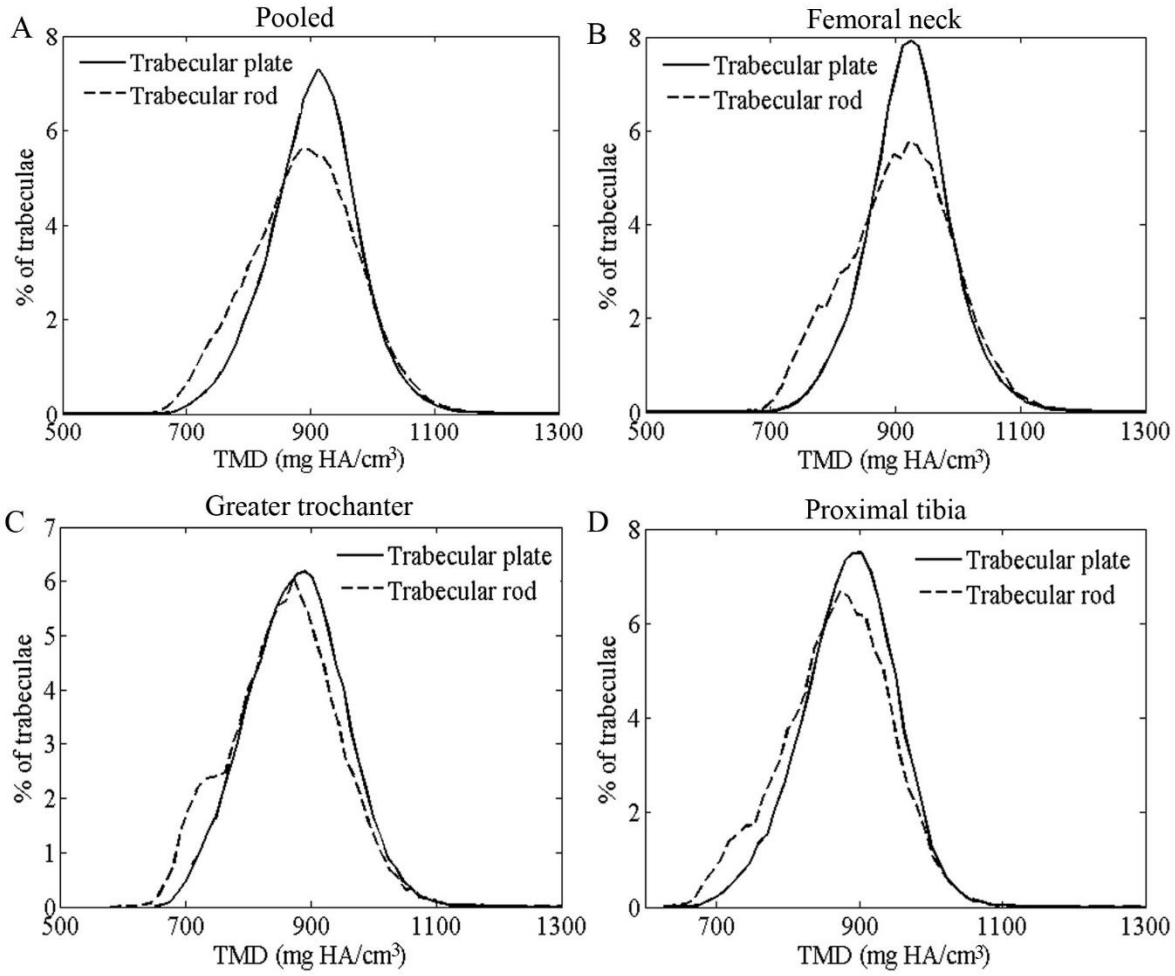

Figure 3.3. Measurements of trabecular plate and rod TMD distributions for the experimental data set pooled from (A) three anatomic locations; (B) femoral neck; (C) greater trochanter; (D) proximal tibia.

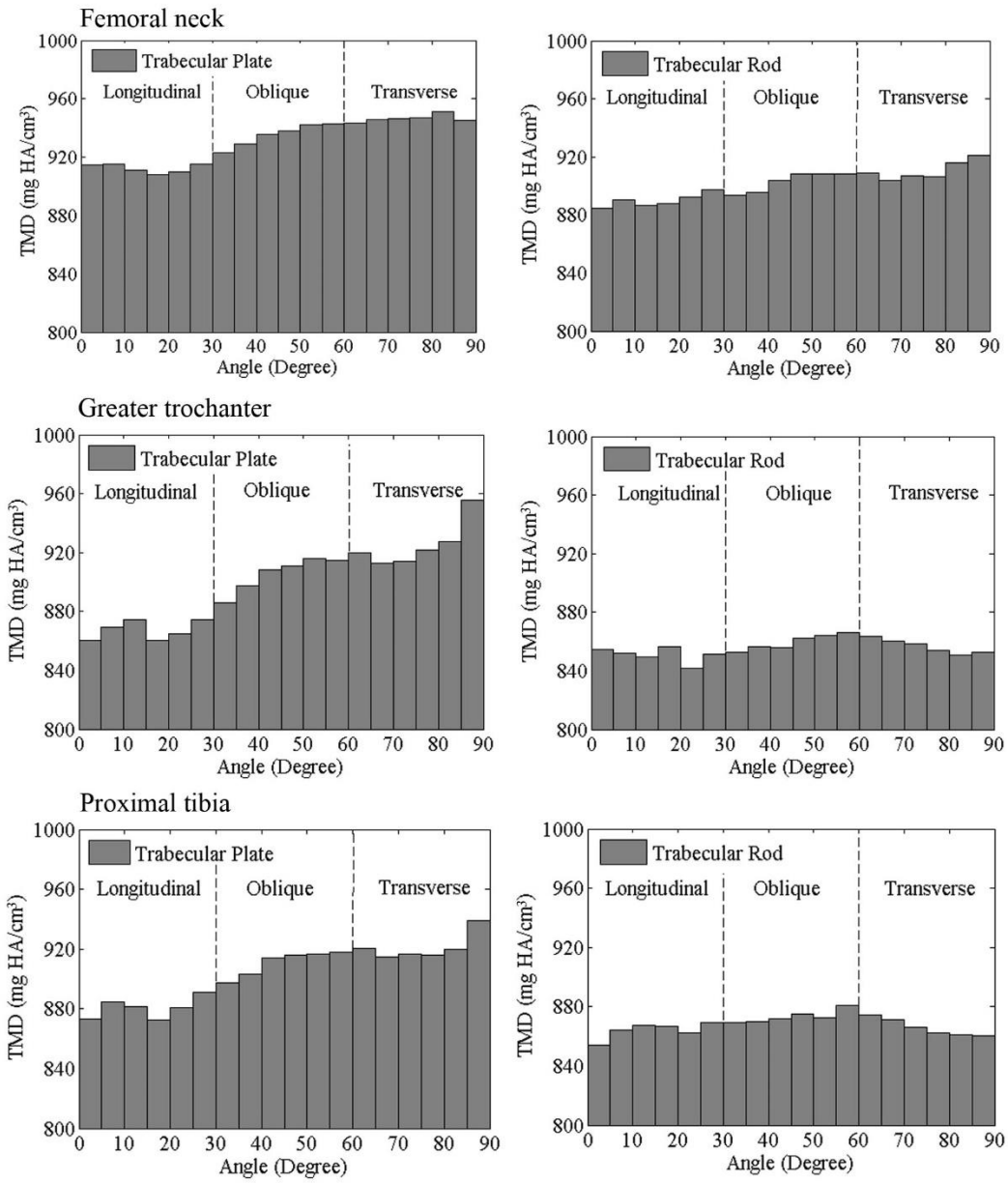

Figure 3.4. Distributions of individual trabecula TMD along trabecular orientation from the longitudinal to transverse direction for trabecular plates (left column) and rods (right column) and for femoral neck (top), greater trochanter (middle), and proximal tibia (bottom).

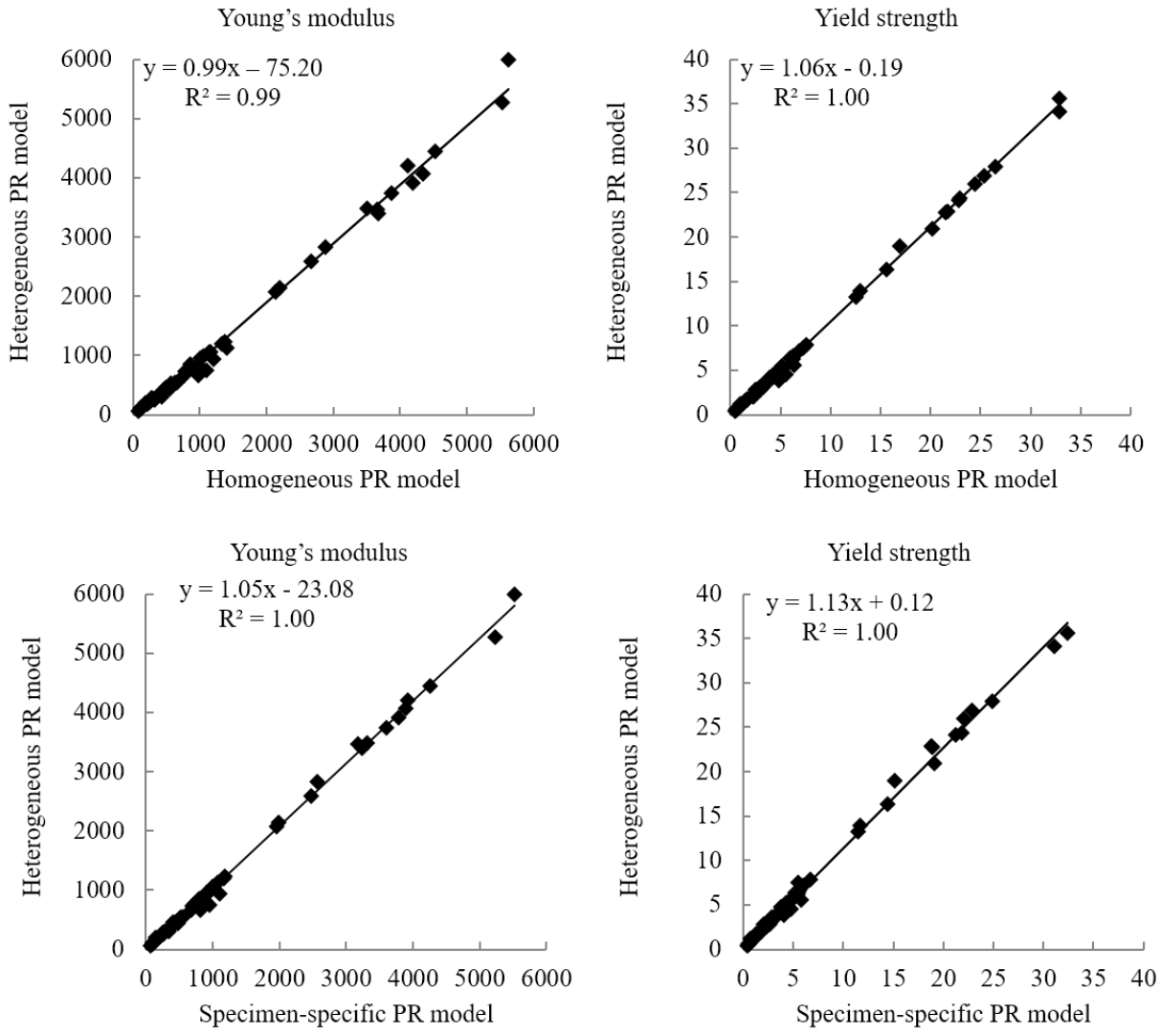

Figure 3.5. Linear regressions between heterogeneous PR models and (A and B) homogeneous PR models or (C and D) specimen-specific PR models for the prediction of Young's modulus and yield strength.

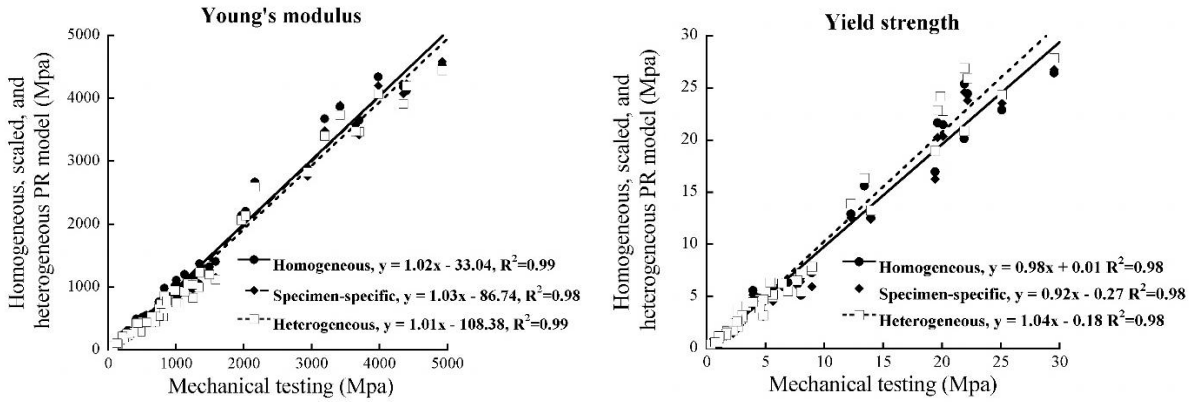

Figure 3.6. Linear regressions of (A) Young's modulus and (B) yield strength between predictions by homogeneous, specimen-specific, and heterogeneous models and measurements by mechanical testing.

Chapter 4. Assessment of whole bone strength based on clinical HR-pQCT plate-rod finite element model

4.1. Introduction

HR-pQCT, as a clinical tool, provides quantitative microstructural and mechanical measures of distal radii and tibiae that have greatly improved our understanding of the pathogenesis of osteoporosis and the mechanisms by which osteoporosis treatments reduce fractures. Studies that assessed the stiffness of distal radii and tibiae using HR-pQCT μFE analysis suggested that decreased whole bone stiffness at these two peripheral anatomic locations were associated with not only wrist and ankle fractures, but also fractures at central skeletons such as the spine and hip fractures (Stein, Liu et al. 2010, Stein, Liu et al. 2011, Stein, Liu et al. 2012). Recently, Zhou et al. conducted a comprehensive validation study of the microstructural and mechanical measures from HR-pQCT scans of distal radii and tibiae. It was showed that the stiffness and yield strength of the distal radii and tibiae segment predicted by HR-pQCT μFE analysis strongly correlated with those estimated by μCT μFE analysis and with direct measurements from mechanical testing experiments. In addition, strong correlations were found between the bone segment within the HR-pQCT region of interest and the whole distal radii and tibiae beyond the scan range. Also, the mechanical properties of distal radii and tibiae segment were correlated with the stiffness of vertebral bodies from the same subjects. These data suggested that the mechanical strength of distal radii and tibiae assessed by HR-pQCT μFE analysis was an important indicator for the subject's bone quality at both the peripheral and central skeletons which are highly susceptible to osteoporotic fractures in the aging population.

The PR μFE models based on μCT have shown excellent accuracy in estimating the mechanical properties of trabecular bone as compared with voxel μFE models and mechanical testing (Wang et al 2015), suggesting great potential in applying the PR modeling technique to clinical HR-pQCT. However, there are significant technical challenges in achieving fine meshing for the trabecular plates and rods based on HR-pQCT images which have a lower resolution and reduced signal-noise ratio compared with μCT images. The thin trabeculae, especially trabecular rods, are usually insufficiently resolved in HR-pQCT images. Thus the trabecular microstructure reconstructed by HR-pQCT requires more refined meshing of the shell and beam elements. The PR modeling algorithm needs to be adapted such that it can be appropriately applied on HR-pQCT images. The high efficiency of μFE analysis using PR models will allow significant reduction in the computational cost of performing linear or nonlinear μFE analysis as compared with the current HR-pQCT μFE simulations using voxel models. Recently, Christen et al. has reported that nonlinear μFE simulations provides important additional information on the risk of forearm fractures other than linear μFE or assessments of bone density or microstructure. It has been the first and so far only clinical study in which nonlinear μFE analyses were performed based on HR-pQCT images, since such simulations require tremendous computational resources. By using the PR modeling approach, nonlinear μFE simulation will be much more feasible for applications in clinical research to help improve the assessment of fracture risks.

Both the trabecular and cortical bone contribute significantly to the whole bone strength of distal radii and tibiae. The PR modeling strategy in Chapter 2 accurately characterize the microstructure and material properties of the trabecular compartment. In order to predict whole bone strength, it is important to create a whole bone model that accounts for contributions from the cortex. Structural features such as cortical porosity and cortical thickness are important

determinants of cortical strength (Currey 1988, Schaffler and Burr 1988, McCalden, McGeough et al. 1993, Wachter, Augat et al. 2001). Cortical porosity occurs as a result of intracortical remodeling that cavitates the cortex (Zebaze, Ghasem-Zadeh et al. 2010). Findings from *in vitro* histology and μCT studies indicate that cortical porosity increases with age (Stein, Feik et al. 1999, Bousson, Meunier et al. 2001, Cooper, Thomas et al. 2007, Busse, Hahn et al. 2010), and this age-related increase in void intracortical volume was shown to account for 76% of the loss in cortical bone strength at the clinically relevant proximal femur (McCalden, McGeough et al. 1993). Further, cortical porosity at the femoral neck was found to be higher in individuals who suffered a hip fracture compared with age-matched non-fractured controls (Barth, Williams et al. 1992, Squillante and Williams 1993, Bell, Loveridge et al. 1999). In addition to porosity, cortical thickness plays an important role in governing bone strength (Augat and Schorlemmer 2006). Biomechanical studies suggested cortical thickness to be a significant predictor of fracture load at the distal radius (Augat, Reeb et al. 1996). Moreover, thinning of the cortex occurs with aging (Mayhew, Thomas et al. 2005, Khosla, Riggs et al. 2006), and has been shown to result in bone fragility and increased fracture risk (Sornay-Rendu, Cabrera-Bravo et al. 2009, Nishiyama, Macdonald et al. 2010, Stein, Kepley et al. 2014). To fulfill the objective of creating a highly efficient whole bone μFE model, a coarsened cortex model that preserves cortical microstructure, in particular cortical porosity and cortical thickness, needs to be connected with the trabecular bone PR model.

4.2. Materials and Methods

4.2.1. Specimen Preparation

Thirty sets of radius and tibia bones from the same donors (72 ± 11 years old, 15 male/15 female) were obtained from Life Legacy Foundation (Tucson, AZ). The specimens were screened

using contact x-ray to ensure no metabolic bone disease or fracture exists. The region of interest in clinical HR-pQCT was selected based on the x-ray scan of each specimen, which is a 9.02 mm thick bone section along the axial direction of the distal radius and tibia. The bone segment were cut using a band saw with the radius and tibia specimens immobilized by a customized clamping jig that ensures precise cutting and alignment between the two end surfaces of the segment. The cutting surfaces were then polished using sandpaper. The specimens were kept hydrated throughout the preparation process and otherwise wrapped with wet gauze and stored in airtight plastic bags in a -20 C freezer.

4.2.2. HR-pQCT and µCT Imaging

The radius and tibia specimens were immersed in saline solution and scanned using HR-pQCT (Scanco Medical AG, Bruttisellen, Switzerland) according to the clinical protocol (60 KVp, 1 mA, 100 ms integration time). The reconstructed HR-pQCT images had an isotropic voxel size of 82 µm. Then, the specimens were scanned again by µCT (µCT 80, Scanco Medical AG) using the ex vivo settings (70 KVp, 114 µA, 700 ms integration time). The reconstructed µCT images had an isotropic voxel size of 37 µm.

4.2.3. HR-pQCT and µCT Nonlinear µFE Analyses

µFE models of distal radius and tibia segments were generated from the HR-pQCT and µCT images by converting each voxel to an 8-node brick element. Nonlinear µFE analyses were carried out by a Finite Element Analysis Program (FEAP, Berkeley, USA) implemented into the super computation system (Stampede, Austin, TX, USA). It was assumed that bone tissue had a rate-independent elasto-plastic material model with tissue elastic modulus of 15 GPa and Poisson's ratio of 0.3. The tissue-level tension and compression yield strains were 0.33% and 0.81%. The post-yield modulus was reduced to 50% of the original modulus. During nonlinear µFE simulation,

the models were loaded to a displacement equal to 1.2 % apparent strain along the axial direction. Stiffness was calculated in the linear region of the load-strain curve and yield load was calculated using a 0.2% offset method.

4.2.4. Trabecular Bone PR μFE Model

The trabecular and cortical compartments of distal radius and tibia were automatically separated in the HR-pQCT images. ITS was performed on the trabecular microstructure, and the PR μFE model was constructed from the segmented plate and rod structure for each specimen (Figure 4.1). Through the PR modeling procedure, individual trabecular plates and rods were meshed into shell and beam elements, respectively. Briefly, the HR-pQCT image of the trabecular microstructure was converted to a surface and curve skeleton with every voxel uniquely classified as inner plate, plate edge, inner rod, rod end and junction points through digital topological analysis (DTA) (Saha and Chaudhuri 1996, Saha, Chaudhuri et al. 1997). ITS further decomposes the surface-curve skeleton into individual trabecular plates and rods. The connection nodes in the surface-curve skeleton formed the framework of the PR model, consisting of plate-plate junction, rod-rod junction, plate-rod junction, rod end and junction between plate edges. In addition, shape-refining nodes were identified from the key turning points on the plate edges and rod curves, providing fine meshing of the trabecular plates and rods. Each trabecular rod was meshed into a beam element with two nodes connecting this rod to its neighboring trabeculae. A curvy rod was further divided into several beams by the key turning points on the rod curve, such that rod curvature could be preserved in the PR model Each trabecular plate was meshed into multiple triangular shell elements through Delaunay Triangulation using the node set of plate-plate junction, plate-rod junction, plate edge junction and turning points on the plate edges (Delaunay 1934). The thickness of individual trabeculae were assigned to the corresponding shell and beam elements,

such that the original volume of each trabecular plates and rods was preserved in the PR model. The PR models of the trabecular compartments at distal radius and tibiae were subjected to μFE analysis, implemented in ABAQUS 6.10 (Dassault Sytemes USA, Waltham, MA) software. Trabecular bone tissue was assumed to have an elastic modulus of 15 GPa and Poisson's ratio equal to 0.3, the same as the voxel μFE models. Trabecular bone tissue was assumed to yield at 0.81% strain with a post-yield modulus equal to 5% of the elastic modulus. A compression test along the axial direction of the radius and tibia specimens was simulated up to 1% apparent strain. Stiffness and yield force were determined from the load-strain curve.

4.2.5. Whole Bone PR μFE Model

For each radius and tibia specimen, a PR μFE model was generated for the whole bone segment including both trabecular and cortical bone (Figure 4.1). After the trabecular network was meshed with shell and beam elements, the trabecular bone PR model was reconnected with the cortical shell. First, the HR-pQCT image of the cortical shell was coarsened from 82 μm to 164 μm voxel size and converted to a voxel model with an 8-node brick element representing a bone voxel. Second, the interconnecting region between the trabecular and cortical compartments was identified by subtracting the thinned trabecular mask from the original trabecular mask. Within the interconnecting region, the nodes of shell and beam elements in the trabecular bone PR model were connected respectively to the closest nodes of the brick elements in the cortical model. These nodes were connected by merging the nodes of the brick elements to the nodes of the shell and beam elements, as illustrated in Figure 4.2. As a result, the brick element was slightly modified, but the overall structure on the intracortical surface was preserved as much as possible. The combined whole bone PR μFE model was then implemented in ABAQUS 6.10 (Dassault Sytemes USA, Waltham, MA) software. Trabecular and cortical bone tissue were assumed to have identical

elastic modulus of 15 GPa and Poisson's ratio equal to 0.3, the same as the voxel μFE models. The bone tissue was assumed to yield at 0.81% strain with a post-yield modulus equal to 5% of the elastic modulus. A compression test along the axial direction of the radius and tibia specimens was simulated up to 1% apparent strain. Whole bone stiffness and yield force were determined from the load-strain curve.

4.2.6. Mechanical Testing

After HR-pQCT and μCT imaging, uniaxial compression mechanical tests were performed to directly measure the mechanical properties of the radius and tibia segments. Using the material testing system (MTS 810, MTS, Eden Prairie, MN), the specimens were loaded to 0.5 mm displacement following three cycles of preconditioning with the loading speed of 5 mm/min. An extensometer (MTS 634.11F-24) was attached at the compression platens and used to measure the direct displacement between two end surfaces of the specimens. Load force was measure using a 100 kN load cell (MTS 661.20E-03). Stiffness was measured in the linear region of the load-displacement curve, and whole bone yield force was determined using the 0.2% offset technique based on the force-strain curve, for comparison with the nonlinear μFE predictions. Ultimate load was measured as the maximum load applied to the specimen during mechanical testing.

4.2.7. Statistical Analyses

Statistical analyses were performed using NCSS software (NCSS 2007, NCSS Statistical Software, Kaysville, Utah). Descriptive data were presented in the form of mean ± standard deviation (SD). Elastic modulus and yield strength predicted by PR models were correlated with those derived from voxel models and measured directly from mechanical testing experiments. Paired T-test was applied to examine the difference among PR model predictions, voxel model predictions and experimental measurements. Two-sided p values <0.05 were considered to

indicate statistical significance. Bland-Altman plots were shown to present the agreement of the PR model relative to mechanical testing experiment and voxel model. The relative difference between two methods (difference/average) was plotted versus their average.

4.3. Results

4.3.1. HR-pQCT Trabecular Bone PR Model

The stiffness and yield load of the trabecular bone compartment at distal radius and distal tibia were estimated by voxel model and PR model nonlinear FE analysis, respectively. Strong correlations were found between the predictions by PR model and those by voxel model, with slope equal to 0.98 and 0.99, R^2 equal to 0.99 for the stiffness and yield load (Figure 4.3).

4.3.2. Whole Bone PR Model

The whole bone PR model based on HR-pQCT was compared with three references: voxel model based on the same HR-pQCT image, voxel model based on corresponding μCT image of the same specimen, and mechanical testing of the specimen. Whole bone stiffness and yield load results from these four methods were summarized in Table 4.1 for radius and tibia. There was no significant difference between the predictions from HR-pQCT PR model and corresponding HR-pQCT voxel model for stiffness or yield load. Correlations between the two models were strong for both stiffness and yield load predictions with R^2 equal to 0.93 and 0.94, respectively (Figure 4.4). Moreover, the HR-pQCT PR model correlated with μCT voxel model and mechanical testing results as strongly (R^2 = 0.88~0.95) as HR-pQCT voxel models. The slopes of the linear regression curves indicated the PR model tended to underestimate yield load of the radius and tibia segment compared to the μCT voxel model and the mechanical testing experiment. The HR-pQCT voxel models of the radius and tibia segments had on average 1.6 and 3.7 million elements, respectively, whereas the PR models generated from the same images reduced model size to 0.1 and 0.2 million

elements (Table 4.2 and 4.3). Furthermore, the CPU time for nonlinear FE analysis using PR models were reduced to 1.6 and 5.9 hours from 36.7 and 78.6 hours for radius and tibia respectively using voxel models.

4.4. Discussion

In this chapter, the PR μFE modeling method was extended in two dimensions, first from high-resolution ex vivo μCT images to lower resolution clinical *in vivo* HR-pQCT images, and second from trabecular bone sub-volume specimens to whole bone segments including the cortex at distal radius and distal tibia. The newly developed HR-pQCT PR models were compared with HR-pQCT voxel models, μCT voxel models, and mechanical testing for predicting whole bone stiffness and yield load at distal radius and tibia. Overall, the PR model was indistinguishable from corresponding voxel model based on the same HR-pQCT image, and strongly correlated with the gold-standard μCT voxel model and mechanical testing results. Besides, the PR model achieved major reduction in model size and computation time compared to voxel model μFE analysis.

Previously, the accuracy of μCT-based PR model has been demonstrated in Chapter 2. The advantage of the PR modeling approach was evidenced by the predictions of trabecular bone Young's modulus and yield strength indistinguishable from traditional voxel models and mechanical testing, and moreover the dramatically improved computational efficiency of PR model nonlinear μFE simulations. Technical gap between μCT and HR-pQCT PR modeling results from the lower resolution and lower signal-noise ratio of HR-pQCT, which requires more delicate meshing of microstructural details. After refining the PR modeling technique, the HR-pQCT-based PR model μFE simulations were strongly correlated with the voxel model μFE simulations for predicting stiffness and yield load of the trabecular bone compartments at distal radius and tibia. The results demonstrated the comparability of PR models with voxel models based on HR-pQCT

images, and meanwhile provided the foundation for extending this highly efficient PR modeling technique to whole bone modeling that incorporates both trabecular and cortical bone.

By connecting the simplified PR model of the trabecular bone with coarsened voxel model of the cortical bone, whole bone PR μFE model was able to preserve trabecular and cortical microstructure and the connection in between the two compartments. Nonlinear μFE analysis using the whole bone PR model showed no significant difference in the calculated whole bone stiffness and yield load from corresponding voxel models based on HR-pQCT at radius or tibia. Studies in the effort of validating HR-pQCT-based μFE analysis have found that predictions of whole bone mechanical properties were highly correlated with μCT FE analysis and mechanical testing measurements. Consistently, results in this study showed that HR-pQCT PR models were as strongly correlated with corresponding μCT voxel models and mechanical testing experiments in estimating the stiffness and yield load of whole bone segments at distal radius and tibia. More importantly, the whole bone PR models led to dramatic improvement in computational efficiency of nonlinear μFE simulations compared to standard voxel models. Instead of large-scale parallel computation, the highly efficient PR model μFE simulations were performed on desktop computers, with approximately 14-fold reduction in model size and 30-fold reduction in CPU time. The high efficiency of PR model permits broader application of whole bone nonlinear μFE simulations in clinical research for better understanding of bone's failure behavior in various bone diseases or monitoring the effects of treatments on the whole bone yield strength which is closely related to bone's resistance to fracture.

In summary, this chapter of my thesis work represents a translational step in the development of plate-rod microstructure model from basic science to clinical research in bone biomechanics. The HR-pQCT PR μFE model provided accurate assessment of whole bone

stiffness and yield load at distal radius and tibia comparable to standard HR-pQCT voxel μFE model. Besides, conversion from voxel model to PR model achieved significant improvement in computational efficiency. The new whole bone PR μFE model added greater potential to HR-pQCT-based bone strength assessment for applications in evaluating risk of fragility fractures and studying mechanisms of fractures in various bone metabolic diseases.

Table 4.1. Comparison of stiffness and yield load predicted by HR-pQCT PR model, HR-pQCT voxel model, μCT voxel model, and measured by mechanical testing. Data is shown as Mean ± SD.

	HR-pQCT PR model	HR-pQCT voxel model	μCT voxel model	Mechanical testing
Radius				
Stiffness (N/mm)	66,555 ± 26,940	64,468 ± 24,925	54,408 ± 22,968*	53,146 ± 23,251*
Yield load (N)	3,715 ± 1,594	3,508 ± 1,431	2,601 ± 1,171*	4,165 ± 1,688*
Trabecular stiffness	17,218 ± 11,024	19,001 ± 12,770	--	--
Trabecular yield load	970 ± 625	1036 ±716	--	--
Tibia				
Stiffness	158,509 ± 50,227	155,767 ± 53,774	122,988 ± 47,139*	136,763 ± 57,688
Yield load	9,050 ± 2,944	8,900 ± 3,200	7,248 ± 2,822*	10,236 ± 4,273*
Trabecular stiffness	71,689 ± 38,719	74,707 ± 37,940	--	--
Trabecular yield load	4,065 ± 2,170	4,047 ± 2,159	--	--

* $p<0.05$ in Student paired t-test between HR-pQCT PR model and this reference method.

Table 4.2. ITS evaluation of the original trabecular microstructure and assessment of the recreated microstructure in the PR model. Data is shown as Mean ± SD.

	Radius	Tibia
BV/TV	0.21 ± 0.04	0.22 ± 0.05
pBV/TV	0.11 ± 0.04	0.14 ± 0.05
rBV/TV	0.10 ± 0.02	0.09 ± 0.02
Number of plates	4,482 ± 2,428	13,152 ± 5,941
Number of rods	9,586 ± 3,910	21,961 ± 8,639
BV/TV	0.21 ± 0.04	0.22 ± 0.05
pBV/TV	0.11 ± 0.04	0.14 ± 0.05
rBV/TV	0.10 ± 0.02	0.09 ± 0.02
Number of shell elements	14,416 ± 8,122	44,722 ± 21,769
Number of beam elements	12,151 ± 4,980	27,959 ± 10,926

Table 4.3. Comparison of model size, FEA computation time between HR-pQCT PR model and voxel model. Data is shown as Mean ± SD.

	Radius		Tibia	
Variables	Voxel model	PR model	Voxel model	PR model
# Trabecular element	882,878 ± 380,907	26,567 ± 12,523	2,328,900 ± 845,229	72,681 ± 28,625
# Cortical element	766,033 ± 266,179	95,754 ± 33,272	1,325,563 ± 545,448	165,695 ± 68,181
# Whole bone element	1,648,911 ± 555,954	122,321 ± 40,505	3,654,463± 1,122,342	238,376 ± 81,029
CPU Time for nonlinear FEA (Hours)	36.74 ± 12.71	1.64 ± 1.20	78.60 ± 24.90	5.87 ± 5.80

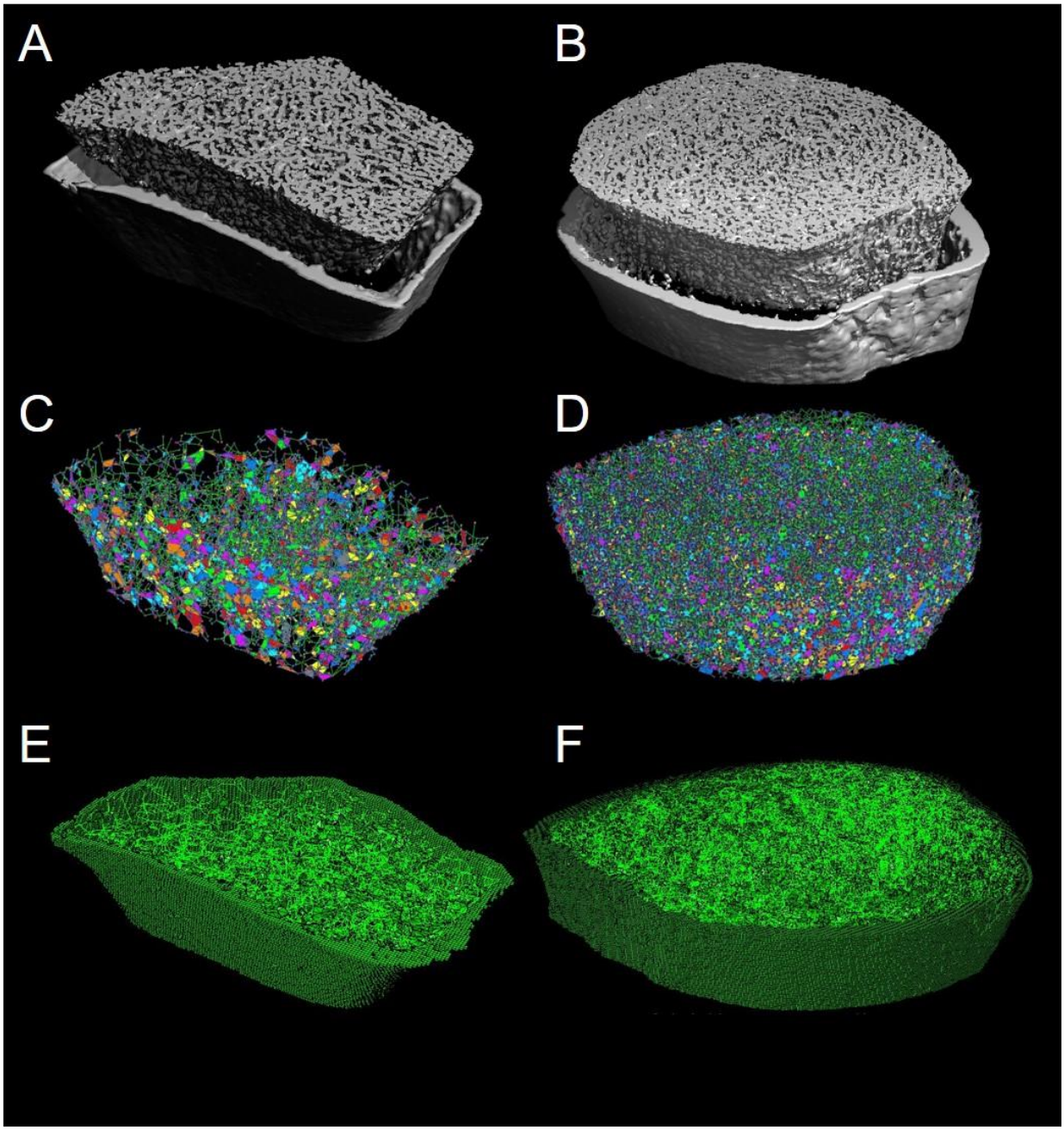

Figure 4.1. HR-pQCT images of (A) distal radius and (B) distal tibia segments with trabecular and cortical compartments separated. Trabecular bone PR μFE model at (C) radius and (D) tibia. Whole bone PR μFE model at (E) radius and (F) tibia.

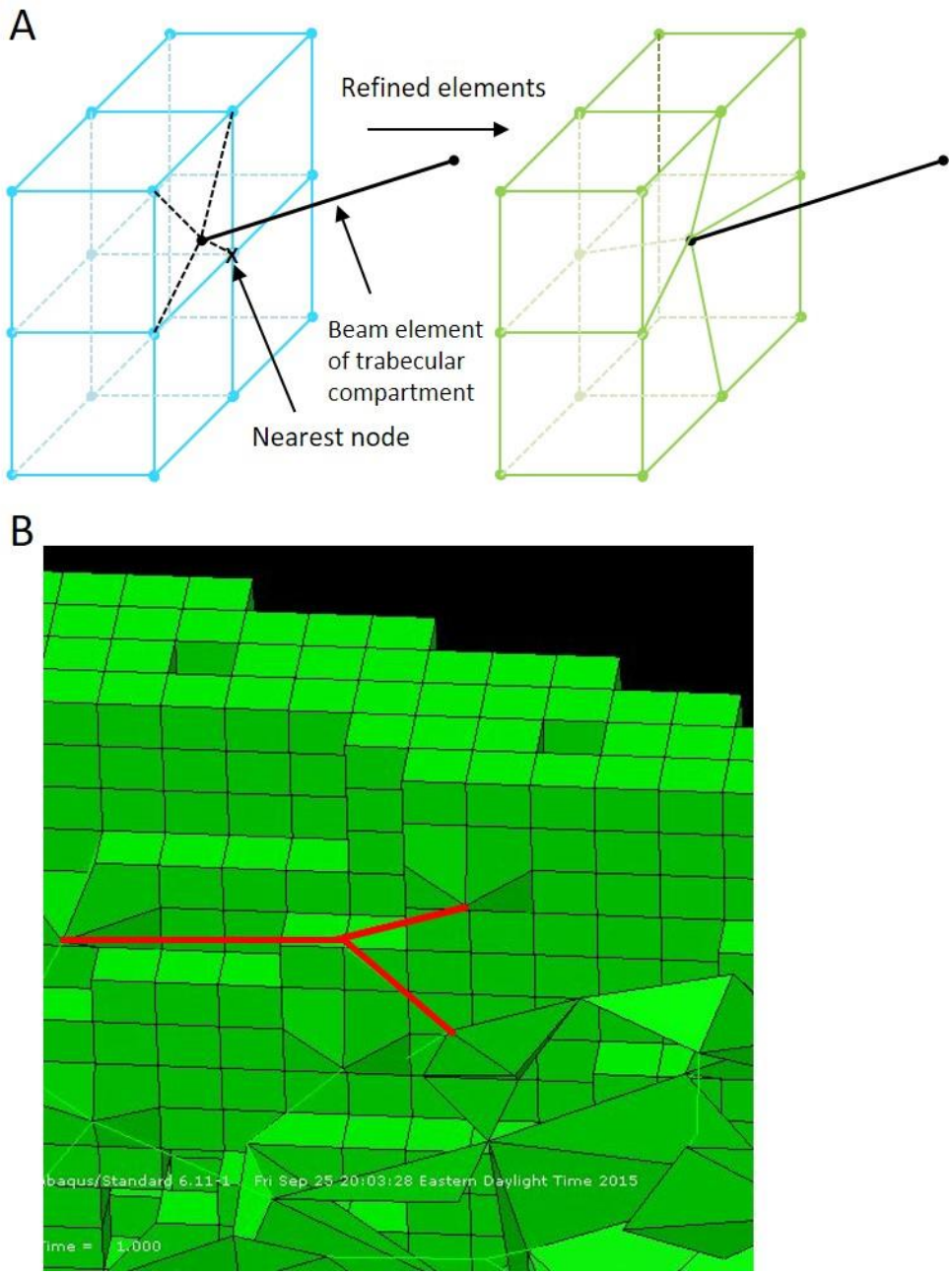

Figure 4.2 Illustration of node connection between the trabecular and cortical bone model in (A) a sketch and (B) an actual HR-pQCT image. Each trabecular node on the interface was connected with the nearest cortical node by merging the cortical node into the trabecular node and altering the cortical elements accordingly.

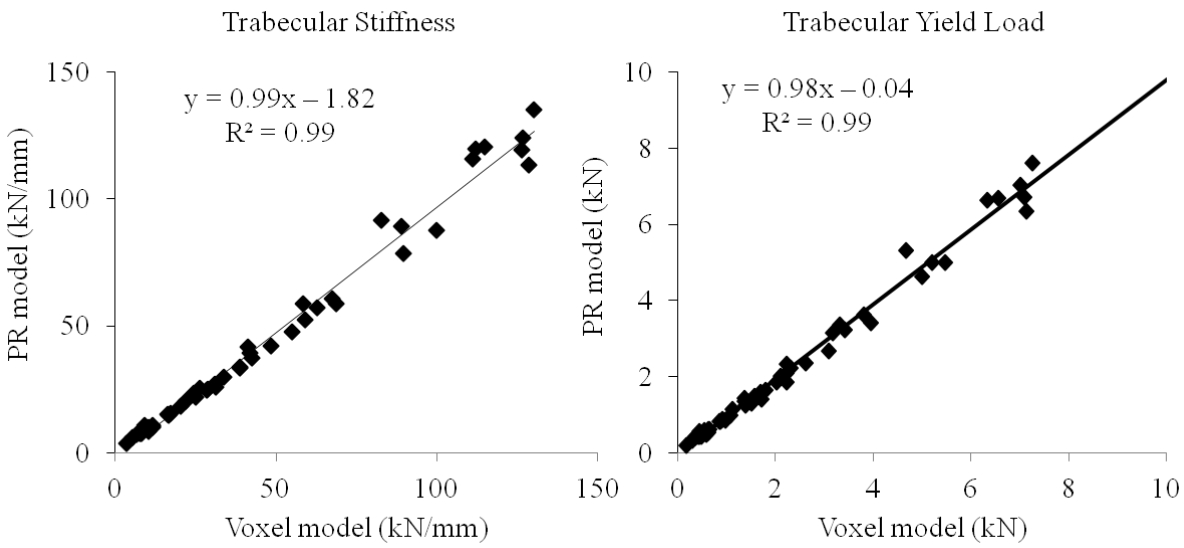

Figure 4.3. Linear regressions between HR-pQCT PR model and voxel model of the trabecular bone at distal radius and tibia for predicting trabecular bone stiffness and yield load.

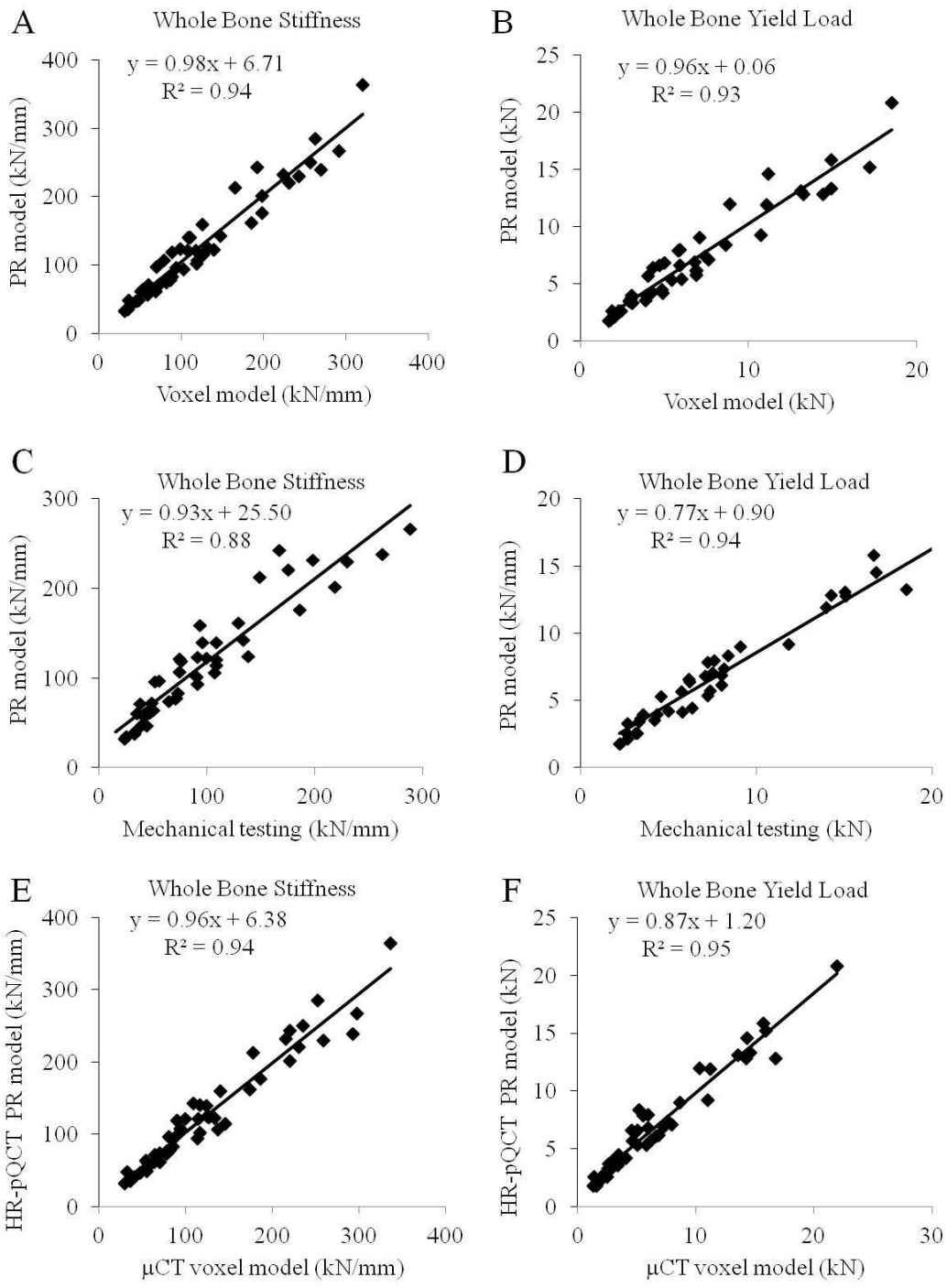

Figure 4.4. Linear regressions between HR-pQCT whole bone PR model and (A and B) HR-pQCT voxel model, (C and D) mechanical testing, and (E and F) µCT voxel model at distal radius and tibia for predicting whole bone stiffness and yield load.

Chapter 5. Deterioration of trabecular plate-rod microstructure and reduced bone strength at distal radius and tibia in postmenopausal women with vertebral fractures

5.1. Introduction

Osteoporosis is a major disease of aging, characterized by low bone mass and microstructural deterioration of trabecular and cortical bone that lead to increased bone fragility and susceptibility to fractures.(NIH 2001) Vertebral fractures are the most common osteoporotic fractures, occurring in nearly 25% of postmenopausal women,(Melton, Lane et al. 1993, Johnell and Kanis 2006) and are associated with substantial increase in the risk of both future vertebral and non-vertebral fractures.(Klotzbuecher, Ross et al. 2000, Lindsay, Silverman et al. 2001, Roux, Fechtenbaum et al. 2007) Assessment of microstructure and mechanical properties of bone at the distal radius and tibia using high resolution peripheral quantitative computed tomography (HR-pQCT) has increased the understanding of the structural abnormalities underlying vertebral fractures.(Melton, Riggs et al. 2007)

Vertebral fractures are the direct result of deterioration of vertebral microstructure with collapse of weakened vertebral bodies. Recent findings suggest that patients with vertebral fractures also have extensive deterioration of trabecular and cortical microstructure at peripheral skeletal sites. (Sornay-Rendu, Boutroy et al. 2007, Stein, Liu et al. 2010, Liu, Stein et al. 2012, Stein, Liu et al. 2012) At the distal radius and tibia, postmenopausal women with vertebral fractures have been shown to have fewer and more widely spaced trabeculae, and thinner cortices compared with women without fractures. HR-pQCT is a noninvasive, three-dimensional (3D) high-resolution imaging technique that measures volumetric bone mineral density (BMD)

of distal radius and tibia, and can visualize fine details of trabecular and cortical microstructure at 82μm voxel size.(Boutroy, Bouxsein et al. 2005, MacNeil and Boyd 2007, Liu, Zhang et al. 2010) Several HR-pQCT studies have demonstrated differences in microstructure and stiffness between subjects with osteoporotic fractures and non-fractured controls. (Melton, Riggs et al. 2007, Boutroy, Van Rietbergen et al. 2008, Vico, Zouch et al. 2008, Melton, Christen et al. 2010, Vilayphiou, Boutroy et al. 2010) Moreover, techniques based on HR-pQCT images have been developed that provide greater insights into skeletal microstructure and mechanical properties. Automatic segmentation algorithms have been developed to distinguish the cortical and trabecular compartments of distal radius and tibia.(Buie, Campbell et al. 2007) A newly developed cortical structure evaluation method measures porosity and thickness of the cortex, important determinants of whole bone strength.(Burghardt, Kazakia et al. 2010, Nishiyama, Macdonald et al. 2010) Individual trabecula segmentation (ITS)-based morphological analysis directly measures individual trabeculae, and characterizes trabecular type (plate and rod), orientation, and connectivity of trabecular plate and rod network.(Saha and Chaudhuri 1996, Saha, Chaudhuri et al. 1997, Liu, Sajda et al. 2006, Liu, Sajda et al. 2008) Because trabecular plates and rods of various orientations have different roles in determining mechanical properties of trabecular bone, ITS assessment of trabecular microstructure adds a unique perspective to bone fragility.(Liu, Bevill et al. 2009, Liu, Zhang et al. 2009, Liu, Walker et al. 2011, Wang, Zhou et al. 2013, Wang, Kazakia et al. 2015, Wang, Zhou et al. 2015) Studies using ITS have shown postmenopausal women with a history of fragility fractures have significantly lower trabecular plate volume, number and connectivity, regardless of aBMD by DXA, suggesting that trabecular plate microstructural abnormalities may increase the risk for osteoporotic fractures,

over and above that associated with low BMD by DXA.(Liu, Stein et al. 2012, Wang, Zhou et al. 2013, Stein, Kepley et al. 2014) However, no studies have focused exclusively on vertebral fracture patients.

HR-pQCT-based micro finite element analysis (μFEA) computationally predicts the mechanical competence of bone at distal radius and tibia. Previous HR-pQCT studies showed that fragility fracture was associated with reduced bone stiffness at radius and tibia, and the bone stiffness was effective in discriminating fracture subjects from non-fractured peers.(Boutroy, Van Rietbergen et al. 2008, Macneil and Boyd 2008, Liu, Zhang et al. 2010) However, bone strength, which is more directly related to bone's resistance to fracture, has rarely been reported in clinical bone research, because the computational cost of calculating bone strength through nonlinear μFE simulation is prohibitively high. The whole bone PR μFE model developed in my thesis research is able to address the need for efficient assessment of bone strength in clinical research.

The goal of this study was to characterize the alterations of trabecular and cortical microstructure, and bone strength at the distal radius and distal tibia in postmenopausal women with vertebral fractures. Besides, this study aimed to test the effectiveness of whole bone PR model nonlinear μFE simulation to discriminate between postmenopausal women with and without vertebral fractures. I hypothesized that postmenopausal women with vertebral fractures have fewer trabecular plates, less trabecular connectivity, more porous and thinner cortices, and lower bone strength at distal tibia and distal radius compared with non-fractured controls.

5.2. Materials and Methods

5.2.1. Subjects

In this study, I included 45 vertebral fracture subjects and 45 control subjects who matched with the fracture subjects according to age and race, from a subset of subjects previously described by Stein and colleagues.(Stein, Liu et al. 2010, Liu, Stein et al. 2012, Stein, Liu et al. 2012) 20 vertebral fracture cases in this cohort were reported in Liu et al and Stein et al. (Liu, Stein et al. 2012, Stein, Liu et al. 2012) Postmenopausal women, over age 60 years or more than 10 years postmenopause, were recruited at Columbia University Medical Center (CUMC; New York, NY, USA) or Helen Hayes Hospital (HHH; West Haverstraw, NY, USA) by advertisement, self-referral, or physician referral. Subjects were eligible for inclusion as vertebral fracture cases if they had a history of a low-trauma vertebral fracture that occurred after menopause or were found to have vertebral fractures by spine X-ray. Low trauma was defined as equivalent to a fall from a standing height or less. Vertebral fractures were identified by spine X-rays according to the semiquantitative method of Genant et al.(Genant, Wu et al. 1993) Vertebrae were graded as normal, or with mild, moderate, or severe deformities, defined as reductions in anterior, middle, or posterior height of 20- 25%, 25-40%, and >40%, respectively. Control subjects had no history of low-trauma fractures at any site and no vertebral deformity on lateral radiograph, as dictated by pre-specified exclusion criteria. There were no BMD requirements for inclusion. Potential cases and controls were excluded if they had endocrinopathies (*e.g.*, untreated hyperthyroidism, Cushing's syndrome, prolactinoma), celiac or other gastrointestinal diseases, abnormal mineral metabolism (*e.g.*, clinical osteomalacia, primary hyperparathyroidism), malignancy except for skin cancer, and drug exposures that could

affect bone metabolism (*e.g.*, glucocorticoids, anticonvulsants, anticoagulants, methotrexate, aromatase inhibitors, thiazolidinediones). Women using hormone replacement therapy or raloxifene were permitted to participate. Women who had ever used teriparatide, or who had taken bisphosphonates for more than 1 year were excluded. All subjects provided written informed consent and the Institutional Review Board of Columbia University Medical Center approved this study. At the study visit, past medical history, reproductive history, and medication use were assessed. A physical exam was performed including height and weight.

5.2.2. Areal BMD

Areal BMD (aBMD) was measured by DXA (QDR-4500; Hologic Inc., Walton, MA, at CUMC; Lunar Prodigy, GE, Madison, WI, at HHH) of lumbar spine L1-L4 (LS), total hip (TH), femoral neck (FN), 1/3 radius (1/3R), and ultradistal radius (UDR). T-scores compared subjects and controls with young-normal populations of the same race and sex, as provided by the manufacturer.

5.2.3. HR-pQCT of the distal radius and tibia

HR-pQCT (Xtreme CT, Scanco Medical AG, Brüttisellen, Switzerland) of the non-dominant distal radius and distal tibia (or non-fractured arm or leg in subjects with prior wrist or ankle fracture) was measured at CUMC as previously described.(Boutroy, Bouxsein et al. 2005, Boutroy, Van Rietbergen et al. 2008, Stein, Liu et al. 2010) The HR-pQCT measurement included 110 slices, corresponding to a 9.02-mm section along the axial direction, with a nominal isotropic voxel size of 82 µm. *After each scan, a reconstructed slide was examined immediately by the operator and grades the image quality from 1 to 5 (1= no motion artifact and 5=high wisping and major discontinuities. The subjects with severe movement artifact (>4) on*

the first scan were rescanned. Analysis was performed according to the standard patient evaluation protocol, (Laib, Hauselmann et al. 1998) and measurements were provided for total volumetric BMD (vBMD), trabecular bone volumetric BMD (Tb.BMD), cortical bone volumetric BMD (Ct.BMD), cortical thickness (Ct.Th), trabecular bone volume fraction (BV/TV), trabecular number (Tb.N), trabecular thickness (Tb.Th), and trabecular separation (Tb.Sp).

5.2.4. Cortical bone measurements

The cortical and trabecular regions were separated using a validated auto-segmentation custom method implemented in Image Processing language (IPL V5.07, Scanco Medical AG).(Buie, Campbell et al. 2007) Cortical microstructural parameters were evaluated as follows.(Burghardt, Kazakia et al. 2010, Nishiyama, Macdonald et al. 2010) Cortical porosity (Ct.Po, %) was calculated as the percentage of void space in the cortex. The number of pores was counted using component labeling, and the mean pore volume was calculated as the total volume of porosity divided by the pore number. The mean pore diameter (Ct.Po.Dm, mm) was calculated from the mean pore volume. Cortical thickness (Ct.Th, mm) was measured directly by removing the intracortical pores from the binary cortex image and using a distance transform. In addition, total bone area (Tot.Ar, mm^2), cortical bone area (Ct.Ar, mm^2), and trabecular bone area (Tb.Ar, mm^2) were calculated as the mean cross sectional area of total, cortical, and trabecular regions, respectively.

5.2.5. ITS-based morphological analyses

A complete volumetric decomposition technique was applied to segment the trabecular network into individual trabecular plates and rods.(Liu, Sajda et al. 2008) Briefly, digital topological analysis (DTA)-based skeletonization was applied first to transform a trabecular bone image into a representation composed of surfaces and curves skeleton while preserving the topology (*i.e.*, connectivity, tunnels, and cavities), as well as plate and rod morphology of trabecular microstructure.(Saha and Chaudhuri 1994, Saha, Chaudhuri et al. 1997) Then, digital topological classification was applied in which each skeletal voxel was uniquely classified as either a plate or a rod type.(Saha and Chaudhuri 1996) Using an iterative reconstruction method, each voxel of the original image was classified as belonging to either an individual plate or rod.(Liu, Sajda et al. 2006) Based on the 3D evaluations of each individual trabecular plate or rod, plate and rod bone volume and number were evaluated by plate and rod bone volume fraction (pBV/TV and rBV/TV), as well as plate and rod number densities (pTb.N and rTb.N, 1/mm). Plate-to-rod ratio (P-R ratio), a parameter of plate versus rod characteristics of trabecular bone, was defined as plate bone volume divided by rod bone volume. The average size of plates and rods was quantified by plate and rod thickness (pTb.Th and rTb.Th, mm), plate surface area (pTb.S, mm^2), and rod length (rTb.ℓ, mm). Intactness of trabecular plate and rod network was characterized by plate–plate, plate–rod, and rod–rod junction density (P-P, P-R, and R-R Junc.D, $1/mm^3$), calculated as the total junctions between trabecular plates and rods normalized by the bulk volume. Orientation of trabecular bone network was characterized by axial bone volume fraction (aBV/TV). A trabecular plate was considered axially aligned if the angle between the normal vector of the plate and the axial direction was between 60° and 90°, and a rod was

considered axially aligned if the angle between its normal vector and the axial direction was between 0° and 30°. aBV/TV was defined as the volume of axially aligned trabeculae divided by the bulk volume.(Liu, Sajda et al. 2008)

5.2.6. HR-pQCT-based PR model nonlinear μFE analysis

Segmented HR-pQCT whole bone image and trabecular bone image of the distal radius and tibia were converted to whole bone and trabecular bone PR μFE models.(Boutroy, Van Rietbergen et al. 2008, Liu, Zhang et al. 2010) Bone tissue was modeled as an isotropic, linear elastic material with a Young's modulus of 15 GPa and a Poisson's ratio of 0.3.(Zysset, Guo et al. 1998, Boutroy, Van Rietbergen et al. 2008, Vilayphiou, Boutroy et al. 2010) For each PR model of the whole bone or trabecular bone segment, a uniaxial compression test was performed to calculate the reaction force under a displacement equal to 1% of bone segment height along the axial direction. Abaqus was used to solve the models. Whole bone stiffness, whole bone yield load, trabecular bone stiffness, and trabecular bone yield load were derived from the nonlinear μFE simulations.

5.2.7. Statistical methods

Analyses were conducted with NCSS software (NCSS Statistical Software, Kaysville, UT, USA). Descriptive data are presented as mean ± standard error of the mean (SEM). Differences between vertebral fracture and control subjects were assessed by Student's t test . Two-sided p-values <0.05 were considered to indicate statistical significance. Analysis of covariance (ANCOVA) was used to evaluate differences in HR-pQCT, ITS, cortical, and μFEA parameters at the radius or tibia after adjusting for aBMD T-score at the ultradistal radius or total

hip, respectively and adjusting for vBMD at distal radius and tibia, respectively. ANOVA was also used to compare fracture versus non-fracture differences between the radius and tibia. Logistic regression analysis was performed to estimate the relative risk of fracture associated with DXA, ITS, cortical, and FE parameters by using odds ratios (OR). Also, receiver operating characteristic (ROC) curve analysis was performed to determine the ability of the DXA, ITS, cortical, and FE parameters to discriminate the fracture subjects from controls.

5.3. Results

5.3.1. Subject characteristics

Forty-five women with a history of postmenopausal vertebral fracture and 45 women with no fracture history were enrolled in this study. Subjects included 83% Caucasian, 8% African-American, and 9% from other backgrounds. Women with and without fractures did not differ on the basis of age, race or ethnicity, body mass index, or time since menopause (Table 5.1). Family history of osteoporosis was similar between groups. Alcohol and tobacco use, medication and supplement use, including use of calcium supplements, hormone replacement therapy, raloxifene, and thyroxine, did not differ between the fracture and control women. Use of vitamin D and bisphosphonates tended to be greater among women with vertebral fractures than in the control group, but the differences were not significant ($p=0.06$ and $p=0.13$, respectively)

5.3.2. Areal BMD

Mean *T*-score was in the osteopenic range, but above the WHO osteoporosis threshold (*T*-score $\leq$ -2.5), in vast majority of the subjects in both groups (Table 5.2). The prevalence of osteoporosis at any site was 49% among vertebral fracture subjects and 40% among controls. The prevalence of osteopenia at any site was 49% among vertebral fracture subjects and 44%

among controls. Mean *T*-score tended to be lower at the LS in vertebral fracture subjects compared with controls, (p=0.07). At the FN, TH, and UDR, the mean *T*-score was 0.5~0.75 SD lower in women with vertebral fractures (p<0.02).

5.3.3. HR-pQCT

At both radius and tibia, women with vertebral fractures had significantly lower vBMD in the trabecular and cortical compartments compared with control subjects. Cortex was 17% and 21% thinner in the fracture subjects at radius and tibia, respectively. Fracture subjects had lower trabecular volume, fewer, thinner, and more widely spaced trabeculae compared with the control group. The differences in most of these parameters remained significant after adjustment for aBMD measurements (Table 5.3 and 5.4).

5.3.4. Trabecular plate and rod microstructure

Significant differences in trabecular plate and rod microstructure were detected between groups using ITS morphological analyses. At the distal radius, plate bone volume fraction and number (pBV/TV and pTb.N) were 21% and 9% lower in the vertebral fracture subjects, and rod bone volume fraction and number (rBV/TV and rTb.N) were 11% and 5% lower. The plate-rod ratio was 10% lower in the fracture subjects, though not significantly different from the control group (p=0.20). Junction density between plates and rods (P-P, P-R, and R-R Junc. D) were 25%, 24%, and 14% lower in fracture subjects, indicating loss of trabecular connectivity compared with the controls. In contrast, the size of individual trabecular plates and rods did not differ significantly. Plate and rod thickness (pTb.Th and rTb.Th) were similar between groups. Plate surface area and rod length (pTb.S and rTb.ℓ) were 3% and 4% larger in fracture subjects

(p=0.04 and <0.001, respectively). Axial bone volume fraction (aBV/TV), which reflects trabecular alignment along the axial direction, was 18% lower in fracture subjects than controls (Table 5.3, Figure 5.1). At the distal tibia, differences between the two groups were mainly observed in trabecular plate measurements: pBV/TV, pTb.N, P-R ratio, P-P Junc.D, P-R Junc.D, and aBV/TV were 20%, 7%, 18%, 19%, 15%, and 17% lower in vertebral fracture subjects. In contrast, rBV/TV, rTb.N, and R-R Junc.D did not differ between groups. Similar to findings at the radius, pTb.Th and rTb.Th did not differ between fracture and non-fracture subjects. After adjusting for aBMD, plate-related ITS measurements (pBV/TV, pTb.N, P-P Junc.D, P-R Junc.D, and aBV/TV) remained significantly lower in women with vertebral fractures at both distal radius and tibia (Table 5.4). Furthermore, pTb.N, rTb.ℓ, and P-R Junc.D at the radius remained significantly different between the fracture and control groups after adjusting for vBMD. Representative HR-pQCT scans analyzed by ITS are shown in Figure 2 for a vertebral fracture subject and a control subject, who were both 71 years old and had similar DXA T-scores.

5.3.5. Cortical microstructure

Women with vertebral fractures also had significant abnormalities in cortical microstructure. Fracture subjects had larger total bone area (6% at radius, 8% at tibia), larger trabecular bone area (12% at radius, 10% at tibia), and smaller cortical bone area (8% at radius, 11% at tibia) than women without fractures. Cortical thickness was 12% and 14% lower in fracture subjects at radius and tibia, respectively. Cortical porosity tended to be greater in fracture subjects (p=0.11, 0.07 at radius and tibia). Pore diameter did not differ between two groups. After adjusting for aBMD, only the total bone area and cortical thickness at the tibia remained significantly different between groups.

5.3.6. Nonlinear μFE analysis

Whole bone and trabecular bone stiffness were lower in women with vertebral fractures at both sites. At the radius, whole bone and trabecular bone stiffness were 16% and 19% lower, and the whole bone and trabecular bone yield load were 17% and 19% lower in fracture subjects. At the tibia, whole bone and trabecular bone stiffness were 17% and 16% lower, and the whole bone and trabecular bone yield load were 19% and 16% lower in fracture subjects. After adjustment for aBMD, whole bone stiffness and yield load at the radius and tibia remained significantly lower, in fracture subjects, while trabecular bone stiffness and failure load no longer differed.

5.3.7. Logistic regression analyses

ORs assessed by logistic regression analyses and AUC assessed by ROC analyses suggested that HR-pQCT, ITS, and μFEA parameters were associated with vertebral fracture (Table 5.3 and 5.4). Whole bone yield load at distal tibia had the highest ORs of 4.46 (95% IC 1.84~6.83) among all the independent variables, such that each SD decrease in yield load was associated with an approximately 4.5-fold increase in the risk of vertebral fracture. At tibia, whole bone yield load had a higher AUC 0.78 than whole bone stiffness (AUC=0.75). At radius, whole bone yield load also had higher ORs and AUC value than whole bone stiffness. Among HR-pQCT parameters, vBMD, Tb.BMD, and trabecular BV/TV showed strong predictive value with AUC from 0.73 to 0.76, comparable to some of the ITS parameters, including pBV/TV, aBV/TV, pTb.N, P-P Junc.D, and P-R Junc.D with AUC of 0.69~0.75. Furthermore, ROC analyses were performed for three multiparametric models using aBMD measurements only, aBMD along with ITS variables, and aBMD, ITS, and FEA parameters all combined. The aBMD

model had an AUC of 0.71, whereas the model using both aBMD and ITS variables had an AUC of 0.81 at the radius and 0.77 at the tibia. Moreover, when combining aBMD, ITS, and FEA parameters, the integrated model had an AUC of 0.86 at the radius and tibia (Table 5.5).

5.4. Discussion

In this study, I used morphological and mechanical analytic tools to identify abnormalities in trabecular plate and rod morphology and cortical bone structure in postmenopausal women with vertebral fractures. Using ITS analysis, I found that women with vertebral fractures had lower plate volume, lower plate trabecular number, reduced connectivity between plates and between plates and rods, and a less axially aligned trabecular network. Besides, vertebral fracture subjects had thinner cortices and tended to have greater cortical porosity. Nonlinear μFE analysis using the newly developed PR model showed that women with vertebral fracture had reduced bone stiffness and yield load, which remained significantly different after adjusting for aBMD by DXA.

ITS, cortical, and μFE analyses of HR-pQCT images have been previously validated in comparison with gold standard micro CT images.(Burghardt, Buie et al. 2010, Liu, Zhang et al. 2010) Liu et al. reported that postmenopausal women with fragility fractures at the forearm, spine, ankle, and other sites had a prominent loss of trabecular plates, along with reduced stiffness at distal radius and tibia.(Liu, Stein et al. 2012) Our current study focused on women with vertebral fractures and increased the sample size, in order to provide further insights into the differences in trabecular and cortical microstructure, as well as bone stiffness between women with vertebral fractures and non-fracture controls. Our results demonstrated that women with

vertebral fractures had abnormalities of both trabecular and cortical microstructure at both radius and tibia. By ITS analyses, I found the vertebral fracture subjects had major depletion of trabecular plates, loss of axially aligned trabeculae, and a trend toward a more rod-like trabecular network particularly at the tibia. Furthermore, the loss of trabecular plate bone volume fraction was mainly attributable to a decrease in plate trabecular number, while plate thickness did not differ. Cortical thinning in vertebral fracture subjects was the most prominent change observed in cortical microstructure. Our observations in this study were consistent with findings from other studies of vertebral and nonvertebral fragility fractures.(Sornay-Rendu, Boutroy et al. 2007, Sornay-Rendu, Cabrera-Bravo et al. 2009, Stein, Liu et al. 2010) Specifically, loss of trabecular plates and thin cortex were found to be two major microstructural characteristics in osteopenic women with fragility fractures.(Stein, Kepley et al. 2014)

Abnormalities in trabecular plate microstructure were similar at the radius and tibia in the vertebral fracture subjects, but rod microstructure was altered only at the radius. This was consistent with several other studies that reported that tibia bone was relatively preserved compared to the radius, perhaps related to a protective effect of weight bearing.(Sornay-Rendu, Boutroy et al. 2007, Stein, Liu et al. 2010, Liu, Stein et al. 2012) When assessing different types of fractures, microstructural deterioration has often been more pronounced at the site that was more closely related anatomically to the fracture site. For example, changes in microstructure among women with wrist fractures were more pronounced at the radius, and tibial trabecular microstructural abnormalities were more severe in women with ankle or hip fractures.(Vico, Zouch et al. 2008, Stein, Liu et al. 2011) Recently, our lab measured trabecular microstructure and mechanical competence of the radius, tibia, and lumbar spine cadaver samples from the same

donors and investigated the correlation between these sites. Our preliminary data showed that HR-pQCT of the radius was more strongly associated with stiffness at the spine, (Liu, Cohen et al. 2010) which might help account for our finding that deterioration in trabecular microstructure was more pronounced at the radius in women with vertebral fractures.

Assessment of microstructure and mechanical competence increased our understanding of fragility fractures, and demonstrated that the HR-pQCT-based PR μFE model had the ability to discriminate fractured postmenopausal women from non-fractured controls, and thus may be useful in predicting fracture risk. Vilayphiou et al. found that μFE-derived mechanical properties of the distal radius and tibia based on HR-pQCT images were associated with all types of fractures.(Vilayphiou, Boutroy et al. 2010) In particular, vertebral fracture was associated with trabecular microstructure more strongly than nonvertebral fracture. Several ITS parameters (pBV/TV, pTb.N, aBV/TV, P-P Junc.D, and P-R Junc.D) and whole bone stiffness and yield load had high ORs and AUC greater than 0.70, suggesting that they might have high predictive value in discriminating vertebral fracture subjects from non-fracture controls. Furthermore, differences in these plate-related ITS parameters and PR model μFE parameters between fracture and control subjects were robust enough to remain significant after adjusting for aBMD *T*-score, which indicated that these microstructural and mechanical alterations in vertebral fracture subjects were independent of aBMD.

This study has several limitations. The cross-sectional study design cannot directly determine whether these methods can reliably predict incident vertebral fractures. Second, there are potential errors in evaluation of microstructure and μFE analysis due to the limited spatial

resolution and signal-to-noise ratio of HR-pQCT. While validation studies have shown that ITS measurements and FE estimates based on HR-pQCT images are strongly correlated with those based on micro CT, there are errors associated with magnitudes of the parameters, especially for trabecular rods.(Liu, Shane et al. 2011)

In conclusion, our study demonstrated marked differences in plate and rod trabecular microstructure, cortical thickness, and whole bone stiffness and yield load at the radius and tibia between postmenopausal women with vertebral fractures and non-fractured controls. ITS analyses revealed a pattern of abnormalities consistent with those reported in other fracture types. Specifically, preferential loss of trabecular plates, loss of axially aligned trabeculae, and loss of trabecular connectivity were the most prominent characteristics of women with vertebral fractures. Whole bone stiffness and yield load, which reflect overall mechanical strength of bone, were found to be markedly lower in women with vertebral fractures. Our results suggested that this pattern of abnormalities may contribute to bone fragility and increased susceptibility to vertebral fractures in postmenopausal women.

Table 5.1. Characteristics of the study population (Mean ± SEM)

	Vertebral fracture (n=45)	Control (n=45)	p
Age (years)	70 ± 1	70 ± 1	0.99
Race (%)			0.86
Caucasian	82	84	
African American	9	7	
Other	9	9	
Ethnicity (%)			0.79
Hispanic	20	18	
Non-Hispanic	80	82	
BMI (kg/m^2)	28 ± 1	27 ± 1	0.53
Years since menopause	22 ± 1	20 ± 1	0.46
Family history of osteoporosis by BMD (%)	40	33	0.78
Family history of fracture (%)	24	22	0.92
Tobacco use (%)			0.24
Never	47	33	
Former	38	47	
Current	7	2	
Alcohol use (beverages per day)	0.5 ± 0.1	0.8 ± 0.2	0.90
Calcium supplements, total daily dose (mg)	635 ± 100	593 ± 90	0.75
Vitamin D supplements, total daily dose (IU)	1233 ± 279	804 ± 228	0.06
Hormone replacement therapy (%)			
Past	38	40	0.46
Current	4	4	0.94
Bisphosphonates[a] (%)			
Past	13	4	0.13
Current	13	4	0.13
Raloxifene (%)	7	4	0.76
Thyroxine (%)	18	24	0.27

[a] Prior bisphosphonate use limited to <1 year

Table 5.2. DXA T-score in vertebral fracture subjects and controls

DXA *T*-score	Vertebral Fracture (Mean ± SEM)	Control (Mean ± SEM)	*p*-Value	OR (95% CI)	AUC
Lumbar spine	-1.81 ± 0.23	-1.26 ± 0.19	0.07	1.45 (0.97, 2.17)	0.60
Total hip	-1.55 ± 0.15	-0.98 ± 0.16	0.02	1.85 (1.12, 3.07)	0.66
Femoral neck	-2.05 ± 0.11	-1.53 ± 0.14	0.01	2.17 (1.24, 3.81)	0.66
1/3 radius	-1.65 ± 0.21	-1.39 ± 0.19	0.38	1.20 (0.80, 1.79)	0.54
Ultradistal radius	-1.75 ± 0.16	-1.00 ± 0.21	0.005	2.05 (1.21, 3.49)	0.67

Table 5.3. HR-pQCT, ITS, cortical, and mechanical parameters at distal radius in vertebral fracture subjects and controls

Variables	Vertebral Fracture (Mean ± SEM)	Control (Mean ± SEM)	*p*-Value	OR (95% CI)	AUC
HR-pQCT					
vBMD (mg HA/cm^3)	250 ± 8	304 ± 10	<0.001[b]	2.87 (1.58, 5.23)	0.73
Tb.BMD (mg HA/cm^3)	107 ± 5	140 ± 6	<0.001[c]	2.62 (1.54, 4.44)	0.74
Ct.BMD (mg HA/cm^3)	812 ± 12	852 ± 10	<0.001	1.68 (1.09, 2.59)	0.63
BV/TV	0.090 ± 0.005	0.116 ± 0.005	<0.001[b]	2.47 (1.48, 4.12)	0.73
Tb.N (1/mm)	1.587 ± 0.055	1.832 ± 0.049	0.001[a]	1.99 (1.27, 3.12)	0.69
Tb.Th (mm)	0.056 ± 0.002	0.063 ± 0.001	0.002[a]	1.94 (1.22, 3.08)	0.71
Tb.Sp (mm)	0.613 ± 0.029	0.502 ± 0.017	0.001[a]	1.83 (1.22, 2.77)	0.69
ITS					
pBV/TV	0.082 ± 0.005	0.103 ± 0.005	0.002[a]	2.00 (1.22, 3.29)	0.69
rBV/TV	0.137 ± 0.005	0.154 ± 0.004	0.007	1.79 (1.15, 2.79)	0.66
aBV/TV	0.089 ± 0.004	0.108 ± 0.004	0.002[a]	2.06 (1.27, 3.35)	0.70
P-R ratio	0.611 ± 0.040	0.684 ± 0.038	0.12	1.34 (0.85, 2.11)	0.62
pTb.N (1/mm)	1.224 ± 0.022	1.344 ± 0.021	<0.001[b,*]	2.36 (1.45, 3.84)	0.73
rTb.N (1/mm)	1.765 ± 0.023	1.862 ± 0.021	0.003	1.90 (1.21, 2.96)	0.69
pTb.Th (mm)	0.222 ± 0.002	0.220 ± 0.001	0.14	1.11 (0.78, 1.58)	0.56
rTb.Th (mm)	0.208 ± 0.001	0.209 ± 0.001	0.46	1.08 (0.72, 1.61)	0.55
P-P Junc.D (1/mm^3)	1.344 ± 0.074	1.786 ± 0.083	<0.001[b]	2.61 (1.51, 4.51)	0.74
P-R Junc.D (1/mm^3)	2.830 ± 0.139	3.705 ± 0.157	<0.001[b,*]	2.71 (1.57, 4.69)	0.74
R-R Junc.D (1/mm^3)	2.595 ± 0.111	3.021 ± 0.108	0.007	1.82 (1.15, 2.86)	0.67
Cortical					
Tt.Ar (mm^2)	244 ± 6	230 ± 5	0.05	1.49 (0.99, 2.26)	0.62
Tb.Ar (mm^2)	203 ± 6	182 ± 5	0.02	1.69 (1.11, 2.57)	0.65
Ct. Ar (mm^2)	47 ± 1	51 ± 1	0.02	1.73 (1.07, 2.80)	0.63
Ct.Th (mm)	0.783 ± 0.024	0.889 ± 0.026	0.003	2.03 (1.22, 3.38)	0.70
Ct.Po	0.055 ± 0.004	0.047 ± 0.003	0.11	1.38 (0.93, 2.05)	0.60
Ct.Po.Dm (mm)	0.154 ± 0.003	0.150 ± 0.003	0.16	1.29 (0.83, 2.00)	0.58
PR model nonlinear FEA					

Whole bone stiffness (N/mm)	60,971 ± 2,193	72,399 ± 2,418	<0.001[a]	2.39 (1.37, 4.18)	0.71
Whole bone yield load (N)	3,468 ±129	4,173 ± 151	<0.001[a]	2.48 (1.39, 4.43)	0.73
Trabecular bone stiffness (N/mm)	11,441 ± 1,099	14,156 ± 965	0.06	1.49 (0.98, 2.29)	0.66
Trabecular bone yield load (N)	629 ± 62	782 ± 52	0.06	1.48 (0.97, 2.26)	0.63

[a] $p<0.05$, [b] $p<0.01$, [c] $p<0.001$, group difference remains significant after adjusting for aBMD at ultradistal radius; [*] $p<0.05$, group difference remains significant after adjusting for vBMD at distal radius.

Table 5.4. HR-pQCT, ITS, cortical, and mechanical parameters at distal tibia in vertebral fracture subjects and controls

Variables	Vertebral Fracture (Mean ± SEM)	Control (Mean ± SEM)	*p*-Value	OR (95% CI)	AUC
HR-pQCT					
vBMD (mg HA/cm^3)	201 ± 7	251 ± 6	<0.001[c]	1.48 (1.13, 1.83)	0.76
Tb.BMD (mg HA/cm^3)	122 ± 5	153 ± 5	<0.001[c]	1.63 (1.23, 2.03)	0.74
Ct.BMD (mg HA/cm^3)	742 ± 11	792 ± 9	<0.001[a]	1.35 (1.09, 1.61)	0.68
BV/TV	0.102 ± 0.004	0.127 ± 0.004	<0.001[c]	1.77 (1.31, 2.34)	0.74
Tb.N (1/mm)	1.551 ± 0.046	1.723 ± 0.042	0.007	1.18 (1.02, 1.34)	0.69
Tb.Th (mm)	0.066 ± 0.002	0.074 ± 0.002	0.001[c]	1.28 (1.07, 1.49)	0.68
Tb.Sp (mm)	0.604 ± 0.021	0.523 ± 0.016	0.003	1.41 (1.05, 1.78)	0.69
ITS					
pBV/TV	0.118 ± 0.006	0.148 ± 0.006	<0.001[b]	1.37 (1.12, 1.62)	0.73
rBV/TV	0.122 ± 0.005	0.127 ± 0.004	0.19	0.99 (0.96, 1.02)	0.55
aBV/TV	0.116 ± 0.004	0.140 ± 0.004	<0.001[b]	1.45 (1.15, 1.74)	0.73
P-R ratio	1.041 ± 0.073	1.261 ± 0.084	0.02	1.05 (0.97, 1.13)	0.61
pTb.N(1/mm)	1.356 ± 0.018	1.463 ± 0.016	<0.001[c]	1.97 (1.26, 2.67)	0.74
rTb.N(1/mm)	1.702 ± 0.023	1.728 ± 0.021	0.41	0.99 (0.96, 1.03)	0.56
pTb.Th(mm)	0.231 ± 0.001	0.232 ± 0.001	0.56	0.99 (0.96, 1.01)	0.56
rTb.Th(mm)	0.212 ± 0.001	0.213 ± 0.001	0.33	1.00 (0.95, 1.04)	0.52
pTb.S (mm^2)	0.198 ± 0.002	0.200 ± 0.002	0.63	0.99 (0.96, 1.02)	0.52
rTb.l (mm)	0.635 ± 0.004	0.619 ± 0.003	<0.001[b]	1.41 (1.10, 1.71)	0.70
P-P Junc.D (1/mm^3)	1.742 ± 0.061	2.156 ± 0.065	<0.001[c]	1.74 (1.28, 2.20)	0.75
P-R Junc.D (1/mm^3)	3.193 ± 0.101	3.766 ± 0.112	<0.001[b]	1.36 (1.12, 1.59)	0.71
R-R Junc.D (1/mm^3)	2.238 ± 0.117	2.272 ± 0.097	0.82	0.98 (0.97, 0.99)	0.56
Cortical					
Tt.Ar (mm^2)	719 ± 19	668 ± 13	0.03[a]	1.13 (0.96, 1.29)	0.63
Tb.Ar (mm^2)	636 ± 19	577 ± 14	0.01	1.20 (0.98, 1.42)	0.65
Ct. Ar (mm^2)	87 ± 2	98 ± 3	0.006	1.18 (1.02, 1.34)	0.63
Ct.Th (mm)	0.912 ± 0.029	1.054 ± 0.032	0.001[a]	1.28 (1.07, 1.50)	0.67
Ct.Po	0.113 ± 0.005	0.101 ± 0.005	0.07	1.06 (0.97, 1.15)	0.60

Ct.Po.Dm (mm)	0.180 ± 0.003	0.180 ± 0.002	0.96	0.98 (0.98, 0.98)	0.52
PR model nonlinear FEA					
Whole bone stiffness (N/mm)	167,536 ± 5,101	201,369 ± 6,424	<0.001[b]	3.47 (1.63, 5.40)	0.75
Whole bone yield load (N)	9,816 ± 299	12,078 ± 418	<0.001[b]	4.46 (1.84, 6.83)	0.78
Trabecular bone stiffness (N/mm)	69,682 ± 4,149	82,522 ± 4,087	0.03	1.67 (1.03, 2.70)	0.64
Trabecular bone yield load (N)	3,760 ± 224	4,473 ± 220	0.03	1.70 (1.05, 2.75)	0.64

[a] $p<0.05$, [b] $p<0.01$, [c] $p<0.001$, group difference remains significant after adjustment for aBMD at total hip.

Table 5.5. Logistic regression of the multiparametric model using aBMD, ITS and FEA parameters

	AUC	
Independent variables	Radius	Tibia
aBMD	0.71	0.71
aBMD + ITS	0.81	0.77
aBMD + ITS + FEA	0.86	0.86

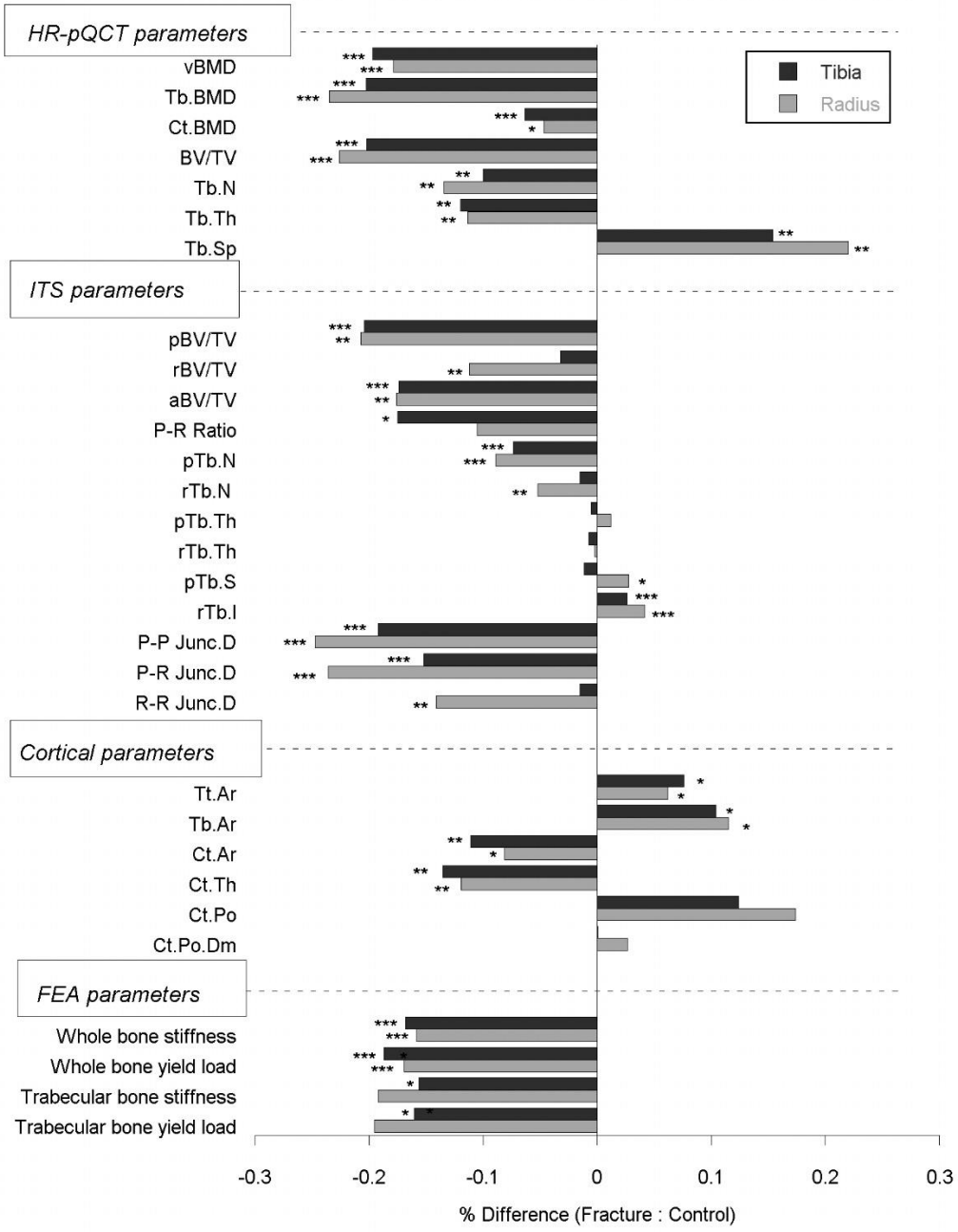

Figure 5.1. Percent difference in HR-pQCT, ITS, cortical, and FEA parameters between women with vertebral fractures and controls. pBV/TV, plate bone volume fraction; rBV/TV, rod bone volume fraction; aBV/TV, axial bone volume fraction; P-R ratio, plate-rod volume ratio; pTb.N,

trabecular plate number; rTb.N, trabecular rod number; pTb.Th, trabecular plate thickness; rTb.Th, trabecular rod thickness; pTb.S, trabecular plate surface area; rTb.l, trabecular rod length; P-P Junc. D, plate-plate junction density; P-R Junc.D, plate-rod junction density; R-R Junc.D, rod-rod junction density; Tt.Ar, total area; Tb.Ar, trabecular area; Ct.Ar, cortical area; Ct.Th, cortical thickness; Ct.Po, cortical porosity; Ct.Po.Dm, cortical pore diameter. (* $p<0.05$, ** $p<0.01$, *** $p<0.001$, fracture vs. control difference)

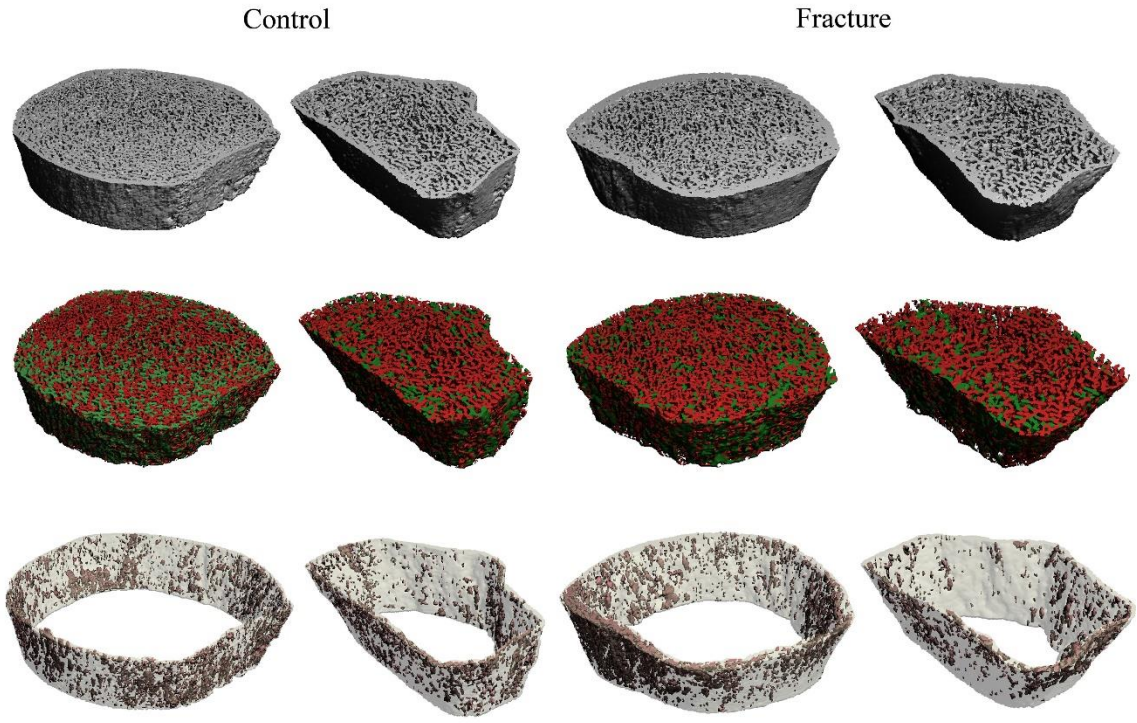

Figure 5.2. Representative HR-pQCT scans at the tibia and radius of a vertebral fracture subject and a control subject who were both 71 years old and had similar DXA T-scores: (top) HR-pQCT image, (middle) trabecular compartment analyzed by ITS with plates in green and rods in red, (bottom) cortical compartment with bone tissue in light grey and pores in pink.

Chapter 6. Summary

In this dissertation, development of three new bone quality analytical techniques were included: (1) plate-rod modeling of trabecular bone microstructure, (2) ITM assessment of heterogeneous mineral distribution in trabecular plates and rods, and (3) HR-pQCT-based whole bone plate-rod modeling at distal radius and tibia. These new techniques formulate a novel approach of fast and accurate assessment of bone strength that accounts for both the microstructure and material properties of human bone. Such highly efficient PR models enable the application of nonlinear μFE analysis on the whole bone level, which requires prohibitively large amount of computational resources using the currently available voxel μFE models. The development of PR models signifies great technical leap in computational biomechanics from three aspects: first to address the challenges in maintaining accurate representation of bone microstructure and minimizing model size and computation time for FE analysis; second to quantify the impact of heterogeneous material properties on apparent mechanical competence; and third to promote FE mechanical simulation to the whole bone level with full appreciation of the trabecular and cortical compartments. In addition, the PR models can generate quantitative mechanical characterization of each individual trabecular plates and rods, and provide a unique method to study the failure mode of individual trabeculae under various loading conditions. The PR model-based bone strength assessment has great promise for applications in both basic science and clinical biomechanics research.

6.1. Plate-rod microstructural modeling

The PR μFE models were created based on segmented trabecular plate and rod microstructure. Using a minimal number of shell and beam elements, the PR model preserved the

morphology, connectivity, and volume of the individual trabecular plates and rods. The prediction of elastic modulus and yield strength by the μCT-based PR models were strongly correlated with those determined by mechanical testing experiments and voxel μFE models. Not only did PR models show excellent accuracy comparable to voxel models, the conversion from voxel model to PR model achieved dramatic reduction in computational time for the nonlinear μFE analysis. The results suggested that trabecular plate and rod microstructure sufficiently determine the apparent mechanical properties of human trabecular bone. Further development of the PR modeling technique extended its application to clinical HR-pQCT images. It was demonstrated that HR-pQCT-based PR models of the trabecular compartment at distal radius and tibia provided estimation of stiffness and yield load as accurate as the voxel models constructed from the same images. By connecting the trabecular bone PR model with coarsened cortical bone model, whole bone PR model was created based on HR-pQCT image. The whole bone PR models were indistinguishable from the corresponding voxel models, and highly correlated with higher-resolution μCT-based voxel models and mechanical testing in predicting whole bone stiffness and yield load. By using PR model, nonlinear μFE simulation of the radius and tibia whole bone segments were implemented in a highly efficient manner.

6.2. Heterogeneous tissue mineralization in trabecular bone

The individual trabecula mineralization (ITM) analysis developed in this dissertation provided direct evidence for distinct tissue mineral density distributions in plate- and rod-like trabeculae of human trabecular bone. ITM analysis enabled evaluating the mineral density of individual trabeculae for particular research interests and investigating the interaction between tissue mineralization and trabecular microstructure. By categorizing trabeculae by trabecular type

and orientation, the study in Chapter 3 demonstrated higher mineral density in trabecular plates relative to rods, and higher mineral density in trabecular plates along the transverse direction relative to the longitudinal direction. Since both trabecular microstructure and tissue property are both important indicators for bone quality, the PR μFE model that accounted for mineral heterogeneity will be a valuable tool for assessing bone strength in the conditions where bone mineralization is altered by diseases or treatments. Though minor impact of the heterogeneous tissue property was observed on the apparent mechanical strength of the bone specimens without metabolic bone diseases, it might make a difference in bone diseases affecting bone mineralization.

6.3. Assessment of bone strength based on clinical HR-pQCT

HR-pQCT has advanced clinical evaluation of bone quality tremendously over the past decade. However, assessment of bone strength from HR-pQCT is still limited by the prohibitively high computational cost that results from the simple voxel-to-element approach of creating μFE models. In this dissertation, the newly developed whole bone PR model permits accurate and fast assessment of bone strength at distal radius and tibia. Bone yield strength predicted by the PR model nonlinear μFE analysis characterizes the initiation of permanent damage in the bone tissue, which provides insights into the failure behavior of bone inaccessible from currently used linear μFE analysis. Chapter 5 showcased the application of the PR models in clinical research on osteoporosis and fragility fractures. Postmenopausal women with vertebral fractures had deteriorated trabecular and cortical microstructure as compared with non-fractured peers. More importantly, the microstructure abnormalities led to mechanical deficiencies characterized by reduced whole bone stiffness and yield load as predicted by the PR model μFE nonlinear analysis. Whole bone yield load was able to effectively discriminate between the

vertebral fracture subjects and non-fractured controls. The results suggested great promise of the HR-pQCT PR model to contribute to the assessment of fracture risk. The efficient evaluation of bone strength facilitated by PR μFE models may also help better understand the underlining biomechanical influence on bone from other metabolic diseases, such as diabetes and chronic kidney disease.

Bibliography

Adams, M. F., et al (2004). "Ultrascalable implicit finite element analyses in solid mechanics with over a half a billion degrees of freedom." in ACM/IEEE Proceedings of SC2004: High Performance Networking and Computing.

Augat, P., H. Reeb and L. E. Claes (1996). "Prediction of fracture load at different skeletal sites by geometric properties of the cortical shell." J Bone Miner Res **11**(9): 1356-1363.

Augat, P. and S. Schorlemmer (2006). "The role of cortical bone and its microstructure in bone strength." Age Ageing **35 Suppl 2**: ii27-ii31.

Barth, R. W., J. L. Williams and F. S. Kaplan (1992). "Osteon morphometry in females with femoral neck fractures." Clin Orthop Relat Res(283): 178-186.

Bayraktar, H. H., E. F. Morgan, G. L. Niebur, G. E. Morris, E. K. Wong and T. M. Keaveny (2004). "Comparison of the elastic and yield properties of human femoral trabecular and cortical bone tissue." J Biomech **37**(1): 27-35.

Bell, K. L., N. Loveridge, J. Power, N. Garrahan, B. F. Meggitt and J. Reeve (1999). "Regional differences in cortical porosity in the fractured femoral neck." Bone **24**(1): 57-64.

Bevill, G., S. K. Eswaran, A. Gupta, P. Papadopoulos and T. M. Keaveny (2006). "Influence of bone volume fraction and architecture on computed large-deformation failure mechanisms in human trabecular bone." Bone **39**(6): 1218-1225.

Bourne, B. C. and M. C. van der Meulen (2004). "Finite element models predict cancellous apparent modulus when tissue modulus is scaled from specimen CT-attenuation." J Biomech **37**(5): 613-621.

Bousson, V., A. Meunier, C. Bergot, E. Vicaut, M. A. Rocha, M. H. Morais, A. M. Laval-Jeantet and J. D. Laredo (2001). "Distribution of intracortical porosity in human midfemoral cortex by age and gender." J Bone Miner Res **16**(7): 1308-1317.

Boutroy, S., M. L. Bouxsein, F. Munoz and P. D. Delmas (2005). "In vivo assessment of trabecular bone microarchitecture by high-resolution peripheral quantitative computed tomography." J Clin Endocrinol Metab **90**(12): 6508-6515.

Boutroy, S., B. Van Rietbergen, E. Sornay-Rendu, F. Munoz, M. L. Bouxsein and P. D. Delmas (2008). "Finite element analysis based on in vivo HR-pQCT images of the distal radius is associated with wrist fracture in postmenopausal women." J Bone Miner Res **23**(3): 392-399.

Buie, H. R., G. M. Campbell, R. J. Klinck, J. A. MacNeil and S. K. Boyd (2007). "Automatic segmentation of cortical and trabecular compartments based on a dual threshold technique for in vivo micro-CT bone analysis." Bone **41**(4): 505-515.

Burghardt, A. J., H. R. Buie, A. Laib, S. Majumdar and S. K. Boyd (2010). "Reproducibility of direct quantitative measures of cortical bone microarchitecture of the distal radius and tibia by HR-pQCT." Bone **47**(3): 519-528.

Burghardt, A. J., G. J. Kazakia, A. Laib and S. Majumdar (2008). "Quantitative assessment of bone tissue mineralization with polychromatic micro-computed tomography." Calcif Tissue Int **83**(2): 129-138.

Burghardt, A. J., G. J. Kazakia, S. Ramachandran, T. M. Link and S. Majumdar (2010). "Age- and gender-related differences in the geometric properties and biomechanical significance of intracortical porosity in the distal radius and tibia." J Bone Miner Res **25**(5): 983-993.

Busse, B., M. Hahn, T. Schinke, K. Puschel, G. N. Duda and M. Amling (2010). "Reorganization of the femoral cortex due to age-, sex-, and endoprosthetic-related effects emphasized by osteonal dimensions and remodeling." J Biomed Mater Res A **92**(4): 1440-1451.

Busse, B., M. Hahn, M. Soltau, J. Zustin, K. Puschel, G. N. Duda and M. Amling (2009). "Increased calcium content and inhomogeneity of mineralization render bone toughness in osteoporosis: mineralization, morphology and biomechanics of human single trabeculae." Bone **45**(6): 1034-1043.

Chen, H., X. Zhou, H. Fujita, M. Onozuka and K. Y. Kubo (2013). "Age-related changes in trabecular and cortical bone microstructure." Int J Endocrinol **2013**: 213234.

Chevalier, Y., D. Pahr, H. Allmer, M. Charlebois and P. Zysset (2007). "Validation of a voxel-based FE method for prediction of the uniaxial apparent modulus of human trabecular bone using macroscopic mechanical tests and nanoindentation." J Biomech **40**(15): 3333-3340.

Christen, D., L. J. Melton, 3rd, A. Zwahlen, S. Amin, S. Khosla and R. Muller (2013). "Improved fracture risk assessment based on nonlinear micro-finite element simulations from HRpQCT images at the distal radius." J Bone Miner Res **28**(12): 2601-2608.

Christen, D., A. Zwahlen and R. Muller (2014). "Reproducibility for linear and nonlinear micro-finite element simulations with density derived material properties of the human radius." J Mech Behav Biomed Mater **29**: 500-507.

Ciarelli, T. E., D. P. Fyhrie and A. M. Parfitt (2003). "Effects of vertebral bone fragility and bone formation rate on the mineralization levels of cancellous bone from white females." Bone **32**(3): 311-315.

Cohen, A., X. S. Liu, E. M. Stein, D. J. McMahon, H. F. Rogers, J. LeMaster, R. R. Recker, J. M. Lappe, X. E. Guo and E. Shane (2009). "Bone Microarchitecture and Stiffness in Premenopausal Women with Idiopathic Osteoporosis." J Clin Endocrinol Metab **94**(11): 4351-4360.

Cooper, D. M., C. D. Thomas, J. G. Clement, A. L. Turinsky, C. W. Sensen and B. Hallgrimsson (2007). "Age-dependent change in the 3D structure of cortical porosity at the human femoral midshaft." Bone **40**(4): 957-965.

Currey, J. D. (1988). "The effect of porosity and mineral content on the Young's modulus of elasticity of compact bone." J Biomech **21**(2): 131-139.

Dede, A. D., S. Tournis, I. Dontas and G. Trovas (2014). "Type 2 diabetes mellitus and fracture risk." Metabolism **63**(12): 1480-1490.

Delaunay, B. (1934). "Sur la sphere vide. A la memoire de Georges Voronoi." Izv. Akad. Nauk SSSR, Otdelenie Matematicheskih i Estestvennyh Nauk **7**: 793-800.

Delmas, P. D. (2000). "How does antiresorptive therapy decrease the risk of fracture in women with osteoporosis?" Bone **27**(1): 1-3.

Ding, M. and I. Hvid (2000). "Quantification of age-related changes in the structure model type and trabecular thickness of human tibial cancellous bone." Bone **26**(3): 291-295.

Eswaran, S. K., A. Gupta, M. F. Adams and T. M. Keaveny (2006). "Cortical and trabecular load sharing in the human vertebral body." J Bone Miner Res **21**(2): 307-314.

Fields, A. J., G. L. Lee, X. S. Liu, M. G. Jekir, X. E. Guo and T. M. Keaveny (2011). "Influence of vertical trabeculae on the compressive strength of the human vertebra." J Bone Miner Res **26**(2): 263-269.

Genant, H. K., C. Y. Wu, C. van Kuijk and M. C. Nevitt (1993). "Vertebral fracture assessment using a semiquantitative technique." J Bone Miner Res **8**(9): 1137-1148.

Gross, T., D. H. Pahr, F. Peyrin and P. K. Zysset (2012). "Mineral heterogeneity has a minor influence on the apparent elastic properties of human cancellous bone: a SRmuCT-based finite element study." Comput Methods Biomech Biomed Engin **15**(11): 1137-1144.

Guo, X. E. and C. H. Kim (2002). "Mechanical consequence of trabecular bone loss and its treatment: a three-dimensional model simulation." Bone **30**(2): 404-411.

Harada, Y., H. W. Wevers and T. D. Cooke (1988). "Distribution of bone strength in the proximal tibia." J Arthroplasty **3**(2): 167-175.

Harrison, N. M., P. F. McDonnell, D. C. O'Mahoney, O. D. Kennedy, F. J. O'Brien and P. E. McHugh (2008). "Heterogeneous linear elastic trabecular bone modelling using micro-CT attenuation data and experimentally measured heterogeneous tissue properties." J Biomech **41**(11): 2589-2596.

Hollister, S. J., J. M. Brennan and N. Kikuchi (1994). "A homogenization sampling procedure for calculating trabecular bone effective stiffness and tissue level stress." J Biomech **27**(4): 433-444.

Hvid, I. (1988). "Mechanical strength of trabecular bone at the knee." Dan Med Bull **35**(4): 345-365.

Jaasma, M. J., H. H. Bayraktar, G. L. Niebur and T. M. Keaveny (2002). "Biomechanical effects of intraspecimen variations in tissue modulus for trabecular bone." Journal of Biomechanics **35**(2): 237-246.

Jaasma, M. J., H. H. Bayraktar, G. L. Niebur and T. M. Keaveny (2002). "Biomechanical effects of intraspecimen variations in tissue modulus for trabecular bone." J Biomech **35**(2): 237-246.

Johnell, O. and J. A. Kanis (2006). "An estimate of the worldwide prevalence and disability associated with osteoporotic fractures." Osteoporos Int **17**(12): 1726-1733.

Kanis, J. A. (2002). "Diagnosis of osteoporosis and assessment of fracture risk." Lancet **359**(9321): 1929-1936.

Kazakia, G. J., A. J. Burghardt, S. Cheung and S. Majumdar (2008). "Assessment of bone tissue mineralization by conventional x-ray microcomputed tomography: comparison with synchrotron radiation microcomputed tomography and ash measurements." Med Phys **35**(7): 3170-3179.

Keaveny, T. M., X. E. Guo, E. F. Wachtel, T. A. McMahon and W. C. Hayes (1994). "Trabecular bone exhibits fully linear elastic behavior and yields at low strains." J Biomech **27**(9): 1127-1136.

Keaveny, T. M., M. R. McClung, H. K. Genant, J. R. Zanchetta, D. Kendler, J. P. Brown, S. Goemaere, C. Recknor, M. L. Brandi, R. Eastell, D. L. Kopperdahl, K. Engelke, T. Fuerst, H. S. Radcliffe and C. Libanati (2014). "Femoral and vertebral strength improvements in postmenopausal women with osteoporosis treated with denosumab." J Bone Miner Res **29**(1): 158-165.

Keaveny, T. M., E. F. Morgan, G. L. Niebur and O. C. Yeh (2001). "Biomechanics of trabecular bone." Annu Rev Biomed Eng **3**: 307-333.

Keaveny, T. M., E. F. Wachtel, X. E. Guo and W. C. Hayes (1994). "Mechanical behavior of damaged trabecular bone." J Biomech **27**(11): 1309-1318.

Khosla, S., B. L. Riggs, E. J. Atkinson, A. L. Oberg, L. J. McDaniel, M. Holets, J. M. Peterson and L. J. Melton, 3rd (2006). "Effects of sex and age on bone microstructure at the ultradistal radius: a population-based noninvasive in vivo assessment." J Bone Miner Res **21**(1): 124-131.

Klotzbuecher, C. M., P. D. Ross, P. B. Landsman, T. A. Abbott, 3rd and M. Berger (2000). "Patients with prior fractures have an increased risk of future fractures: a summary of the literature and statistical synthesis." J Bone Miner Res **15**(4): 721-739.

Laib, A., H. J. Hauselmann and P. Ruegsegger (1998). "In vivo high resolution 3D-QCT of the human forearm." Technol Health Care **6**(5-6): 329-337.

Lindsay, R., S. L. Silverman, C. Cooper, D. A. Hanley, I. Barton, S. B. Broy, A. Licata, L. Benhamou, P. Geusens, K. Flowers, H. Stracke and E. Seeman (2001). "Risk of new vertebral fracture in the year following a fracture." JAMA **285**(3): 320-323.

Liu, X. S., G. Bevill, T. M. Keaveny, P. Sajda and X. E. Guo (2009). "Micromechanical analyses of vertebral trabecular bone based on individual trabeculae segmentation of plates and rods." J Biomech **42**(3): 249-256.

Liu, X. S., A. Cohen, E. Shane, E. Stein, H. Rogers, S. L. Kokolus, P. T. Yin, D. J. McMahon, J. M. Lappe, R. R. Recker and X. E. Guo (2010). "Individual trabeculae segmentation (ITS)-based morphological analysis of high-resolution peripheral quantitative computed tomography images detects abnormal trabecular plate and rod microarchitecture in premenopausal women with idiopathic osteoporosis." J Bone Miner Res **25**(7): 1496-1505.

Liu, X. S., A. Cohen, E. Shane, P. T. Yin, E. M. Stein, H. Rogers, S. L. Kokolus, D. J. McMahon, J. M. Lappe, R. R. Recker, T. Lang and X. E. Guo (2010). "Bone density, geometry, microstructure, and stiffness: Relationships between peripheral and central skeletal sites assessed by DXA, HR-pQCT, and cQCT in premenopausal women." J Bone Miner Res **25**(10): 2229-2238.

Liu, X. S., P. Sajda, P. K. Saha, F. W. Wehrli, G. Bevill, T. M. Keaveny and X. E. Guo (2008). "Complete Volumetric Decomposition of Individual Trabecular Plates and Rods and Its

Morphological Correlations With Anisotropic Elastic Moduli in Human Trabecular Bone." Journal of Bone and Mineral Research **23**(2): 223-235.

Liu, X. S., P. Sajda, P. K. Saha, F. W. Wehrli and X. E. Guo (2006). "Quantification of the Roles of Trabecular Microarchitecture and Trabecular Type in Determining the Elastic Modulus of Human Trabecular Bone." Journal of Bone and Mineral Research **21**(10): 1608-1617.

Liu, X. S., E. Shane, D. J. McMahon and X. E. Guo (2011). "Individual trabecula segmentation (ITS)-based morphological analysis of microscale images of human tibial trabecular bone at limited spatial resolution." J Bone Miner Res **26**(9): 2184-2193.

Liu, X. S., E. M. Stein, B. Zhou, C. A. Zhang, T. L. Nickolas, A. Cohen, V. Thomas, D. J. McMahon, F. Cosman, J. Nieves, E. Shane and X. E. Guo (2012). "Individual trabecula segmentation (ITS)-based morphological analyses and microfinite element analysis of HR-pQCT images discriminate postmenopausal fragility fractures independent of DXA measurements." Journal of Bone and Mineral Research **27**(2): 263-272.

Liu, X. S., M. D. Walker, D. J. McMahon, J. Udesky, G. Liu, J. P. Bilezikian and X. E. Guo (2011). "Better skeletal microstructure confers greater mechanical advantages in Chinese-American women versus white women." J Bone Miner Res **26**(8): 1783-1792.

Liu, X. S., J. Wang, B. Zhou, E. Stein, X. Shi, M. Adams, E. Shane and X. E. Guo (2013). "Fast trabecular bone strength predictions of HR-pQCT and individual trabeculae segmentation-based plate and rod finite element model discriminate postmenopausal vertebral fractures." J Bone Miner Res **28**(7): 1666-1678.

Liu, X. S., X. H. Zhang and X. E. Guo (2009). "Contributions of trabecular rods of various orientations in determining the elastic properties of human vertebral trabecular bone." Bone **45**(2): 158-163.

Liu, X. S., X. H. Zhang, C. S. Rajapakse, M. J. Wald, J. Magland, K. K. Sekhon, M. F. Adam, P. Sajda, F. W. Wehrli and X. E. Guo (2010). "Accuracy of high-resolution in vivo micro magnetic resonance imaging for measurements of microstructural and mechanical properties of human distal tibial bone." J Bone Miner Res **25**(9): 2039-2050.

Liu, X. S., X. H. Zhang, K. K. Sekhon, M. F. Adams, D. J. McMahon, J. P. Bilezikian, E. Shane and X. E. Guo (2010). "High-resolution peripheral quantitative computed tomography can assess microstructural and mechanical properties of human distal tibial bone." J Bone Miner Res **25**(4): 746-756.

Loveridge, N., J. Power, J. Reeve and A. Boyde (2004). "Bone mineralization density and femoral neck fragility." Bone **35**(4): 929-941.

MacNeil, J. A. and S. K. Boyd (2007). "Accuracy of high-resolution peripheral quantitative computed tomography for measurement of bone quality." Med Eng Phys **29**(10): 1096-1105.

Macneil, J. A. and S. K. Boyd (2008). "Bone strength at the distal radius can be estimated from high-resolution peripheral quantitative computed tomography and the finite element method." Bone **42**(6): 1203-1213.

Mayhew, P. M., C. D. Thomas, J. G. Clement, N. Loveridge, T. J. Beck, W. Bonfield, C. J. Burgoyne and J. Reeve (2005). "Relation between age, femoral neck cortical stability, and hip fracture risk." Lancet **366**(9480): 129-135.

McCalden, R. W., J. A. McGeough, M. B. Barker and C. M. Court-Brown (1993). "Age-related changes in the tensile properties of cortical bone. The relative importance of changes in porosity, mineralization, and microstructure." J Bone Joint Surg Am **75**(8): 1193-1205.

Melton, L. J., 3rd, D. Christen, B. L. Riggs, S. J. Achenbach, R. Muller, G. H. van Lenthe, S. Amin, E. J. Atkinson and S. Khosla (2010). "Assessing forearm fracture risk in postmenopausal women." Osteoporos Int **21**(7): 1161-1169.

Melton, L. J., 3rd, A. W. Lane, C. Cooper, R. Eastell, W. M. O'Fallon and B. L. Riggs (1993). "Prevalence and incidence of vertebral deformities." Osteoporos Int **3**(3): 113-119.

Melton, L. J., 3rd, B. L. Riggs, T. M. Keaveny, S. J. Achenbach, P. F. Hoffmann, J. J. Camp, P. A. Rouleau, M. L. Bouxsein, S. Amin, E. J. Atkinson, R. A. Robb and S. Khosla (2007). "Structural determinants of vertebral fracture risk." J Bone Miner Res **22**(12): 1885-1892.

Melton, L. J., 3rd, B. L. Riggs, G. H. van Lenthe, S. J. Achenbach, R. Muller, M. L. Bouxsein, S. Amin, E. J. Atkinson and S. Khosla (2007). "Contribution of in vivo structural measurements and load/strength ratios to the determination of forearm fracture risk in postmenopausal women." J Bone Miner Res **22**(9): 1442-1448.

Morgan, E. F. and T. M. Keaveny (2001). "Dependence of yield strain of human trabecular bone on anatomic site." J Biomech **34**(5): 569-577.

Nawathe, S., H. Akhlaghpour, M. L. Bouxsein and T. M. Keaveny (2014). "Microstructural failure mechanisms in the human proximal femur for sideways fall loading." J Bone Miner Res **29**(2): 507-515.

Nawathe, S., B. P. Nguyen, N. Barzanian, H. Akhlaghpour, M. L. Bouxsein and T. M. Keaveny (2015). "Cortical and trabecular load sharing in the human femoral neck." J Biomech **48**(5): 816-822.

Nickolas, T. L., M. B. Leonard and E. Shane (2008). "Chronic kidney disease and bone fracture: a growing concern." Kidney Int **74**(6): 721-731.

Niebur, G. L., M. J. Feldstein, J. C. Yuen, T. J. Chen and T. M. Keaveny (2000). "High-resolution finite element models with tissue strength asymmetry accurately predict failure of trabecular bone." J Biomech **33**(12): 1575-1583.

Niebur, G. L., J. C. Yuen, A. J. Burghardt and T. M. Keaveny (2001). "Sensitivity of damage predictions to tissue level yield properties and apparent loading conditions." J Biomech **34**(5): 699-706.

Niebur, G. L., J. C. Yuen, A. C. Hsia and T. M. Keaveny (1999). "Convergence behavior of high-resolution finite element models of trabecular bone." J Biomech Eng **121**(6): 629-635.

NIH (2001). "NIH Consensus Development Panel on Osteoporosis Prevention, Diagnosis, and Therapy, March 7-29, 2000: highlights of the conference." South Med J **94**(6): 569-573.

Nishiyama, K. K., A. Cohen, P. Young, J. Wang, J. M. Lappe, X. E. Guo, D. W. Dempster, R. R. Recker and E. Shane (2014). "Teriparatide increases strength of the peripheral skeleton in premenopausal women with idiopathic osteoporosis: a pilot HR-pQCT study." J Clin Endocrinol Metab **99**(7): 2418-2425.

Nishiyama, K. K., H. M. Macdonald, H. R. Buie, D. A. Hanley and S. K. Boyd (2010). "Postmenopausal women with osteopenia have higher cortical porosity and thinner cortices at the

distal radius and tibia than women with normal aBMD: an in vivo HR-pQCT study." J Bone Miner Res **25**(4): 882-890.

Nishiyama, K. K., H. M. Macdonald, D. A. Hanley and S. K. Boyd (2013). "Women with previous fragility fractures can be classified based on bone microarchitecture and finite element analysis measured with HR-pQCT." Osteoporos Int **24**(5): 1733-1740.

Papadopoulos, P. and J. Lu (1998). "A general framework for the numerical solution of problems in finite elasto-plasticity." Computer Methods in Applied Mechanics and Engineering **159**(1-2): 1-18.

Papadopoulos, P. and J. Lu (2001). "On the formulation and numerical solution of problems in anisotropic finite plasticity." Computer Methods in Applied Mechanics and Engineering **190**(37-38): 4889-4910.

Pistoia, W., B. van Rietbergen, E. M. Lochmüller, C. A. Lill, F. Eckstein and P. Rüegsegger (2002). "Estimation of distal radius failure load with micro-finite element analysis models based on three-dimensional peripheral quantitative computed tomography images." Bone **30**(6): 842-848.

Rho, J. Y., P. Zioupos, J. D. Currey and G. M. Pharr (1999). "Variations in the individual thick lamellar properties within osteons by nanoindentation." Bone **25**(3): 295-300.

Roschger, P., H. S. Gupta, A. Berzlanovich, G. Ittner, D. W. Dempster, P. Fratzl, F. Cosman, M. Parisien, R. Lindsay, J. W. Nieves and K. Klaushofer (2003). "Constant mineralization density distribution in cancellous human bone." Bone **32**(3): 316-323.

Roschger, P., E. P. Paschalis, P. Fratzl and K. Klaushofer (2008). "Bone mineralization density distribution in health and disease." Bone **42**(3): 456-466.

Ross, R. D., L. H. Edwards, A. S. Acerbo, M. S. Ominsky, A. S. Virdi, K. Sena, L. M. Miller and D. R. Sumner (2014). "Bone matrix quality after sclerostin antibody treatment." J Bone Miner Res **29**(7): 1597-1607.

Roux, C., J. Fechtenbaum, S. Kolta, K. Briot and M. Girard (2007). "Mild prevalent and incident vertebral fractures are risk factors for new fractures." Osteoporos Int **18**(12): 1617-1624.

Roy, M. E., J. Y. Rho, T. Y. Tsui, N. D. Evans and G. M. Pharr (1999). "Mechanical and morphological variation of the human lumbar vertebral cortical and trabecular bone." J Biomed Mater Res **44**(2): 191-197.

Saha, P. K. and B. B. Chaudhuri (1994). "Detection of 3-d simple points for topology preserving transformations with application to thinning." Ieee Transactions on Pattern Analysis and Machine Intelligence **16**(10): 1028-1032.

Saha, P. K. and B. B. Chaudhuri (1996). "3D digital topology under binary transformation with applications." Computer Vision and Image Understanding **63**(3): 418-429.

Saha, P. K., B. B. Chaudhuri, B. Chanda and D. D. Majumder (1994). "Topology preservation in 3d digital space." Pattern Recognition **27**(2): 295-300.

Saha, P. K., B. B. Chaudhuri, D. Dutta and D. D. Majumder (1997). "A new shape preserving parallel thinning algorithm for 3D digital images." Pattern Recognition **30**(12): 1939-1955.

Schaffler, M. B. and D. B. Burr (1988). "Stiffness of compact bone: effects of porosity and density." J Biomech **21**(1): 13-16.

Schuit, S. C., M. van der Klift, A. E. Weel, C. E. de Laet, H. Burger, E. Seeman, A. Hofman, A. G. Uitterlinden, J. P. van Leeuwen and H. A. Pols (2004). "Fracture incidence and association with bone mineral density in elderly men and women: the Rotterdam Study." Bone **34**(1): 195-202.

Seitz, S., T. Koehne, C. Ries, A. De Novo Oliveira, F. Barvencik, B. Busse, C. Eulenburg, T. Schinke, K. Puschel, J. M. Rueger, M. Amling and P. Pogoda (2013). "Impaired bone mineralization accompanied by low vitamin D and secondary hyperparathyroidism in patients with femoral neck fracture." Osteoporos Int **24**(2): 641-649.

Shi, X., X. S. Liu, X. Wang, X. E. Guo and G. L. Niebur (2010). "Effects of trabecular type and orientation on microdamage susceptibility in trabecular bone." Bone **46**(5): 1260-1266.

Siris, E. S., P. D. Miller, E. Barrett-Connor, K. G. Faulkner, L. E. Wehren, T. A. Abbott, M. L. Berger, A. C. Santora and L. M. Sherwood (2001). "Identification and fracture outcomes of undiagnosed low bone mineral density in postmenopausal women: results from the National Osteoporosis Risk Assessment." JAMA **286**(22): 2815-2822.

Sornay-Rendu, E., S. Boutroy, F. Munoz and P. D. Delmas (2007). "Alterations of cortical and trabecular architecture are associated with fractures in postmenopausal women, partially independent of decreased BMD measured by DXA: the OFELY study." J Bone Miner Res **22**(3): 425-433.

Sornay-Rendu, E., J. L. Cabrera-Bravo, S. Boutroy, F. Munoz and P. D. Delmas (2009). "Severity of vertebral fractures is associated with alterations of cortical architecture in postmenopausal women." J Bone Miner Res **24**(4): 737-743.

Squillante, R. G. and J. L. Williams (1993). "Videodensitometry of osteons in females with femoral neck fractures." Calcif Tissue Int **52**(4): 273-277.

Stein, E. M., A. Kepley, M. Walker, T. L. Nickolas, K. Nishiyama, B. Zhou, X. S. Liu, D. J. McMahon, C. Zhang, S. Boutroy, F. Cosman, J. Nieves, X. E. Guo and E. Shane (2014). "Skeletal

structure in postmenopausal women with osteopenia and fractures is characterized by abnormal trabecular plates and cortical thinning." J Bone Miner Res **29**(5): 1101-1109.

Stein, E. M., X. S. Liu, T. L. Nickolas, A. Cohen, D. J. McMahon, B. Zhou, C. Zhang, M. Kamanda-Kosseh, F. Cosman, J. Nieves, X. E. Guo and E. Shane (2012). "Microarchitectural abnormalities are more severe in postmenopausal women with vertebral compared to nonvertebral fractures." J Clin Endocrinol Metab **97**(10): E1918-1926.

Stein, E. M., X. S. Liu, T. L. Nickolas, A. Cohen, V. Thomas, D. J. McMahon, C. Zhang, F. Cosman, J. Nieves, J. Greisberg, X. E. Guo and E. Shane (2011). "Abnormal microarchitecture and stiffness in postmenopausal women with ankle fractures." J Clin Endocrinol Metab **96**(7): 2041-2048.

Stein, E. M., X. S. Liu, T. L. Nickolas, A. Cohen, V. Thomas, D. J. McMahon, C. Zhang, P. T. Yin, F. Cosman, J. Nieves, X. E. Guo and E. Shane (2010). "Abnormal microarchitecture and reduced stiffness at the radius and tibia in postmenopausal women with fractures." J Bone Miner Res **25**(12): 2572-2581.

Stein, M. S., S. A. Feik, C. D. Thomas, J. G. Clement and J. D. Wark (1999). "An automated analysis of intracortical porosity in human femoral bone across age." J Bone Miner Res **14**(4): 624-632.

Stone, K. L., D. G. Seeley, L. Y. Lui, J. A. Cauley, K. Ensrud, W. S. Browner, M. C. Nevitt, S. R. Cummings and G. Osteoporotic Fractures Research (2003). "BMD at multiple sites and risk of fracture of multiple types: long-term results from the Study of Osteoporotic Fractures." J Bone Miner Res **18**(11): 1947-1954.

Vanderoost, J., S. V. Jaecques, G. Van der Perre, S. Boonen, J. D'Hooge, W. Lauriks and G. H. van Lenthe (2011). "Fast and accurate specimen-specific simulation of trabecular bone elastic modulus using novel beam-shell finite element models." J Biomech **44**(8): 1566-1572.

Vico, L., M. Zouch, A. Amirouche, D. Frere, N. Laroche, B. Koller, A. Laib, T. Thomas and C. Alexandre (2008). "High-resolution pQCT analysis at the distal radius and tibia discriminates patients with recent wrist and femoral neck fractures." J Bone Miner Res **23**(11): 1741-1750.

Vilayphiou, N., S. Boutroy, E. Sornay-Rendu, B. Van Rietbergen, F. Munoz, P. D. Delmas and R. Chapurlat (2010). "Finite element analysis performed on radius and tibia HR-pQCT images and fragility fractures at all sites in postmenopausal women." Bone **46**(4): 1030-1037.

Wachter, N. J., P. Augat, G. D. Krischak, M. R. Sarkar, M. Mentzel, L. Kinzl and L. Claes (2001). "Prediction of strength of cortical bone in vitro by microcomputed tomography." Clin Biomech (Bristol, Avon) **16**(3): 252-256.

Wang, H., X. S. Liu, B. Zhou, J. Wang, B. Ji, Y. Huang, K. C. Hwang and X. E. Guo (2013). "Accuracy of individual trabecula segmentation based plate and rod finite element models in idealized trabecular bone microstructure." J Biomech Eng **135**(4): 044502.

Wang, J., G. J. Kazakia, B. Zhou, X. T. Shi and X. E. Guo (2015). "Distinct Tissue Mineral Density in Plate and Rod-Like Trabeculae of Human Trabecular Bone." J Bone Miner Res.

Wang, J., B. Zhou, X. S. Liu, A. J. Fields, A. Sanyal, X. Shi, M. Adams, T. M. Keaveny and X. E. Guo (2015). "Trabecular plates and rods determine elastic modulus and yield strength of human trabecular bone." Bone **72**: 71-80.

Wang, J., B. Zhou, I. Parkinson, C. D. L. Thomas, J. G. Clement, N. Fazzalari and X. E. Guo (2013). "Trabecular Plate Loss and Deteriorating Elastic Modulus of Femoral Trabecular Bone in Intertrochanteric Hip Fractures." Bone Research **4**: 346-354.

Wehrli, F. W. (2007). "Structural and functional assessment of trabecular and cortical bone by micro magnetic resonance imaging." J Magn Reson Imaging **25**(2): 390-409.

Wolff, J. (1986). The Law of Bone Remodeling, Springer.

Zebaze, R. M. D., A. Ghasem-Zadeh, A. Bohte, S. Iuliano-Burns, M. Mirams, R. I. Price, E. J. Mackie and E. Seeman (2010). "Intracortical remodelling and porosity in the distal radius and post-mortem femurs of women: a cross-sectional study." Lancet **375**(9727): 1729-1736.

Zhou, B., X. S. Liu, J. Wang, X. L. Lu, A. J. Fields and X. E. Guo (2014). "Dependence of mechanical properties of trabecular bone on plate-rod microstructure determined by individual trabecula segmentation (ITS)." J Biomech **47**(3): 702-708.

Zhou, B., J. Wang, E. M. Stein, Z. Zhang, K. K. Nishiyama, C. A. Zhang, T. L. Nickolas, E. Shane and X. E. Guo (2014). "Bone density, microarchitecture and stiffness in Caucasian and Caribbean Hispanic postmenopausal American women." Bone Research **2**.

Zhou, B., J. Wang, Y. E. Yu, Z. Zhang, S. Nawathe, K. K. Nishiyama, F. R. Rosete, T. M. Keaveny, E. Shane and X. E. Guo (2016). "High-resolution peripheral quantitative computed tomography (HR-pQCT) can assess microstructural and biomechanical properties of both human distal radius and tibia: Ex vivo computational and experimental validations." Bone **86**: 58-67.

Zysset, P. K., X. E. Guo, C. E. Hoffler, K. E. Moore and S. A. Goldstein (1998). "Mechanical properties of human trabecular bone lamellae quantified by nanoindentation." Technol Health Care **6**(5-6): 429-432.